System Identification Modeling of Micro Air Vehicles from Visual Motion Tracking Data

A THESIS
SUBMITTED TO THE FACULTY OF THE GRADUATE SCHOOL
OF THE UNIVERSITY OF MINNESOTA
BY

Robyn Michèle Woollands

IN PARTIAL FULFILLMENT OF THE REQUIREMENTS
FOR THE DEGREE OF
Master of Science

Dec, 2010

Acknowledgements

Over the past two years many people have played a key role in helping me to succeed and accomplish my academic and research goals. First I need to thank my adviser, Professor Bernie Mettler, for all her advice and guidance during the course of this project. The encouragement, nurturing and genuine interest in her students' well-being is evident in our weekly meetings. In addition to her support from an academic perspective, I would like to thank her for all the challenging tennis matches we played this summer that have also resulted in the improvement of my tennis!

My sincere thanks also needs to be extended to the following people, who have all helped me immensely at various stages over the last two years: Professor Demoz Gebre-Egziabher, Professor Yohannes Ketema, Professor William Garrard, Professor Perry Leo and Professor Tryphon Georgiou. Their advice, guidance, teaching and endless willingness to help were invaluable to me.

The work presented in this thesis extends work previously undertaken by other graduate students at the University of Minnesota. Thus I need to thank Navid Dadkhah and Pradeep Reddy for their help and suggestions relating to the Kalman filter (Chapter 3) and the maximum likelihood estimation algorithm (Chapter 6) respectively.

Throughout the duration of my studies at the University of Minnesota I was financially supported on a teaching assistantship from the Department of Aerospace Engineering and Mechanics, and a research assistantship from the Department of Mechanical Engineering.

Thanks to my friends and fellow graduate students, Adhika Lie, Raghu Devulapalli, Ryan Howe-Veenstra, Arda Özdemir, Kamrun Turkoglu, Andrei Dorobantu, Paul Norman, Wei Guo and Narina Jung for our many study sessions, assignment collaboration and your friendship over the past two years.

To my "US family" with whom I have lived since arriving here - Michelle Chen, Shweta Singh and Michal Rogalski - this freezing Minnesotan adventure wouldn't have been the same without you!

A special thank you to Chris and Kathleen Macosko for their unending kindness, guidance, prayers and friendship.

To Joseph and Linda Butterfield, thanks for your hospitality, kindness, support and encouragement. Trips to your home in Rochester have been a highlight and a source of inspiration!

To my parents Robert and Michèle, and my best friend (sister) Andrea, thanks for ALL the phone calls, skype calls, emails, gmail chats and surprise packages. Your unceasing support, guidance and love over the years have brought me to where I am today.

Finally thanks to Joe, my sweetheart, for making this challenging endeavor worth while!

Abstract

This thesis describes a new technique, known as direct trajectory sampling, for extracting aerodynamic coefficients directly from Micro Air Vehicle trajectory data. The experiment is conducted in the Interactive Guidance and Control Laboratory (Aerospace Engineering & Mechanics, University of Minnesota) using the vision tracking system and an aircraft fitted with reflective markers on its wings, fuselage, nose and tail. The technique was developed to study the aerodynamics of small-scale aircraft as the traditional methods using wind tunnels and computational fluid dynamics have produced limited results for this rapidly growing field of research.

The indoor environment takes advantage of the stationary atmospheric conditions and as the glider is launched into flight the full trajectory is captured by the tracking system while the aircraft position and attitude vary naturally throughtout the flight. The experimental data is filtered with a Kalman filter to eliminate any data drop-outs and to generate velocities and accelerations. Aerodynamic forces, moments and angles are extracted from the filtered flight data and are used in the calculation of the aerodynamic coefficients.

Stability derivatives are determined from the aerodynamic coefficients using a linear regression approach, and these are then refined with a flight simulation model and the technique of maximum likelihood estimation. Once the stability derivatives have been refined, resulting in an identified system, the aircraft simulation model is validated using the weighted mean of each stability derivative. Pleasing results are obtained in several cases but further refinement of the model is required before confident claims regarding the validation can be made.

Nomenclature

Chapter 2 variables

x_N	=	longitudinal position
y_E	=	lateral position
z_D	=	vertical position
ϕ	=	roll Euler angle
θ	=	pitch Euler angle
ψ	=	yaw Euler angle

Chapter 3 variables

x	=	state vector
$v(t)$	=	process noise
q	=	variance
T	=	sampling time
Q_k	=	covariance of discrete-time process noise
P	=	covariance matrix
r	=	measurement residual
S	=	residual covariance
K	=	optimal gain
R	=	variance of measurement noise
$\hat{x^+}$	=	state covariance matrix
P^+	=	error covriance matrix
v_N	=	longitudinal velocity
v_E	=	lateral velocity
v_D	=	vertical velocity
p	=	roll velocity
q	=	pitch velocity
r	=	yaw velocity
a_N	=	longitudinal acceleration
a_E	=	lateral acceleration
a_D	=	vertical acceleration
a_p	=	roll acceleration
a_q	=	pitch acceleration
a_r	=	yaw acceleration

Chapter 4 variables

R	=	rotation matrix
v_b	=	velocity in the body frame
u	=	longitudinal velocity in the body frame
v	=	lateral velocity in the body frame
w	=	vertical velocity in the body frame
α	=	angle of attack
β	=	angle of side-slip
θ	=	pitch angle
ϕ	=	roll angle
$\mathbf{v}$	=	velocity
m	=	mass
F_{ext}	=	external forces
F_{aero}	=	aerodynamic forces
$F_{gravity}$	=	gravitational force
$\mathbf{I}$	=	mass moment of inertia
w	=	angular velocity
M_{ext}	=	external moments
M_{aero}	=	aerodynamic moments
$\mathbf{I_B}$	=	inertia in the body frame
w_B	=	angular velocity in the body frame
X_{aero}	=	aerodynamic force vector
F_x	=	axial aerodynamic force (A)
F_y	=	side aerodynamic force (Y)
F_z	=	normal aerodynamic force (N)
$\mathbf{V}$	=	airspeed
D	=	drag force
L	=	lift force
ρ	=	air density
C_D	=	coefficient of drag
C_Y	=	side force coefficient
C_L	=	coefficient of lift
C_l	=	roll moment coefficient
C_m	=	pitch moment coefficient
C_n	=	yaw moment coefficient
A_{AC}	=	total wing surface area
b	=	wingspan
c	=	chord length

Chapter 5 variables

C_{D0}	=	drag coefficient at zero angle of attack
$C_{D\alpha}$	=	drag coefficient at α angle of attack
$C_{D\delta_E}$	=	drag coefficient due to elevator input
δ_E	=	elevator input
C_{Y0}	=	side-force coefficient at zero angle of attack
$C_{Y\beta}$	=	side-force coefficient at β side-slip angle
$C_{Y\delta_R}$	=	side-force coefficient due to rudder input
δ_R	=	rudder input
$C_{Y\delta_A}$	=	side-force coefficient due to aileron input
δ_A	=	aileron input
C_{L0}	=	lift coefficient at zero angle of attack
$C_{L\alpha}$	=	lift coefficient at α angle of attack
$C_{L\delta_E}$	=	lift coefficient due to elevator input
C_{l0}	=	roll moment coefficient at zero angle of attack
$C_{l\beta}$	=	roll moment coefficient at β side-slip angle
$C_{l\delta_R}$	=	roll moment coefficient due to rudder input
$C_{l\delta_A}$	=	roll moment coefficient due to aileron input
C_{lp}	=	roll moment coefficient at p roll rate
C_{lr}	=	roll moment coefficient at r yaw rate
C_{m0}	=	pitch moment coefficient at zero angle of attack
$C_{m\alpha}$	=	pitch moment coefficient at α angle of attack
$C_{m\delta_E}$	=	pitch moment coefficient due to elevator input
$C_{m\delta_A}$	=	pitch moment coefficient due to aileron input
C_{mq}	=	pitch moment coefficient at q pitch rate
C_{n0}	=	yaw moment coefficient at zero angle of attack
$C_{n\beta}$	=	yaw moment coefficient at β side-slip angle
$C_{n\delta_R}$	=	yaw moment coefficient due to rudder input
$C_{n\delta_A}$	=	yaw moment coefficient due to aileron input
C_{np}	=	yaw moment coefficient at p roll rate
C_{nr}	=	yaw moment coefficient at r yaw rate

Chapter 6 variables

π	=	mean of the Gaussian distribution
σ^2	=	variance of the Gaussian distribution
y_k	=	random sample or experimental trajectory
$\hat{y}_k$	=	simulated trajectory
J	=	cost function
$\hat{x}$	=	estimate of measurement
R	=	covariance matrix
$\hat{\mathbf{p}}$	=	unknown parameter e.g. stability derivative
N	=	total number of increments
$\nabla_{\hat{\mathbf{p}}}$	=	Jacobian vector
$\nabla^2_{\hat{\mathbf{p}}}$	=	Hessian matrix
x_N	=	longitudinal position
y_E	=	lateral position
z_D	=	vertical position
ϕ	=	roll Euler angle
θ	=	pitch Euler angle
ψ	=	yaw Euler angle
$\mathbf{V}$	=	airspeed
α	=	angle of attack
β	=	angle of side-slip
v_N	=	longitudinal velocity
v_E	=	lateral velocity
v_D	=	vertical velocity
p	=	roll velocity
q	=	pitch velocity
r	=	yaw velocity
t	=	time
C_{D0}	=	drag coefficient at zero angle of attack
$C_{D\alpha}$	=	drag coefficient at α angle of attack
C_{Y0}	=	side-force coefficient at zero angle of attack
$C_{Y\beta}$	=	side-force coefficient at β side-slip angle
C_{L0}	=	lift coefficient at zero angle of attack
$C_{L\alpha}$	=	lift coefficient at α angle of attack
C_{l0}	=	roll moment coefficient at zero angle of attack
$C_{l\beta}$	=	roll moment coefficient at β side-slip angle
C_{lp}	=	roll moment coefficient at p roll rate
C_{lr}	=	roll moment coefficient at r yaw rate

C_{m0} = pitch moment coefficient at zero angle of attack
$C_{m\alpha}$ = pitch moment coefficient at α angle of attack
C_{mq} = pitch moment coefficient at q pitch rate
C_{n0} = yaw moment coefficient at zero angle of attack
$C_{n\beta}$ = yaw moment coefficient at β side-slip angle
C_{np} = yaw moment coefficient at p roll rate
C_{nr} = yaw moment coefficient at r yaw rate
C_D = coefficient of drag
C_Y = side force coefficient
C_L = coefficient of lift
D = drag force
Y = side force
L = lift force
C_l = roll moment coefficient
C_m = pitch moment coefficient
C_n = yaw moment coefficient
M_x = longitudinal aerodynamic moment
M_y = lateral aerodynamic moment
M_z = vertical aerodynamic moment
u = longitudinal velocity in the body frame
v = lateral velocity in the body frame
w = vertical velocity in the body frame
$\dot{u}$ = longitudinal acceleration in the body frame
$\dot{v}$ = lateral acceleration in the body frame
$\dot{w}$ = vertical acceleration in the body frame
dt = time increment
g = gravitational acceleration
m = mass
$\dot{p}$ = roll acceleration
$\dot{q}$ = pitch acceleration
$\dot{r}$ = yaw acceleration
I_x = longitudinal moment of inertia
I_y = lateral moment of inertia
I_z = vertical moment of inertia

Contents

List of Figures

List of Tables

"There shall be wings! If the accomplishment be not for me, 'tis for some other." **- Leonardo da Vinci** (1452 - 1519).

Chapter 1

Introduction

1.1 Micro Air Vehicles

Micro aerial vehicles (MAVs) are a class of small unmanned aerial vehicles (UAVs) that generally satisfy the following physical requirements. Their wingspan, mass and maximum velocity should all be less than 15 cm, 200 g and 10 ms^{-1} respectively (McMichael and Francis 1997). MAVs can be further classified into three main subsections: fixed-wing aircraft, rotary-wing aircraft and flapping-wing aircraft, with each design being unique to its intended purpose. To stay airborne, fixed-wing aircraft operate at higher forward velocities that allow them to travel longer distances, however this limits their performance in confined spaces like buildings. Rotary-wing aircraft possess greater agility in addition to their hovering capabilities, but their range is relatively short. To date, flapping wing designs are yet to achieve the same technological level as the afore mentioned designs, but research in this area is being actively pursued as these aircraft could eventually prove to be superior to both fixed-wing and rotary-wing designs due to their enhanced maneuverability (Chabalko et al. 2009).

The unique operational capabilities demonstrated by MAVs means that advancement in their design is the focus of many organizations, from commercial and research organizations through to the government and military. The uses for MAVs are numerous, and in many cases they out perform their UAV predecessors with regard to specific tactical tasks. Atmospheric monitoring is one application for MAVs, and in this capacity they may be flown in swarms to detect harmful biological agents or simply for weather forecasting. Another application is flying MAVs in the confines of a city as a surveillance system to improve security. Using MAVs for civilian search and rescue aids or for military operations and reconnaissance are other important/desired ways of employing this technology.

All the above mentioned applications take advantage of the unique MAV characteristics such as portability, ease of deployment, high mobility, unobtruse/stealth (i.e. low visibility and sound), and ability to carry a small payload of sensors, cameras and GPS for navig-

ation. However, along with the numerous advantages afforded by MAVs there are several accompanying disadvantages. Since MAVs perform at low airspeeds their flight is characterized by low Renolds numbers ($< 1 \times 10^{-5}$) where laminar separation and separation bubbles dominate (Campbell and Maciejowski 2009). As a result they are extremely sensitive to atmospheric conditions such as turbulence and wind, thus making them a challenge to pilot. In addition, their relatively flexible nature make MAVs difficult to control in-flight and also adds to the complexity of aerodynamic modeling.

1.2 History of Micro Aerial Vehicle studies

The first powered flight was conducted by the Wright brothers at Kitty Hawk, North Carolina in 1903, and over 100 years later engineers are continually being presented with challenges regarding the physical nature of flight. The 20th century may be remembered for its advancements in manned atmospheric and space flight but the 21st century will surely be classified as the era for development of autonomous and unmanned flight. Designs and research relating to UAVs emerged during the last two decades of the 20th century to satisfy demands made by the military and various civilian organizations (Pines and Bohorquez 2006). The study and development of UAVs is now a global challenge due to the great benefits, such as surveillance and atmospheric monitoring, that this technology can offer (Gallington et al. 1996; NASA 2009). The birth of a new class of UAV know as an MAV is a result of the technological advancements in the past decade with regard to fuel cells, miniature internal combustion engines and computer hardware components (Chabalko et al. 2009). These vehicles are restricted by certain size, mass and speed specifications (see Section 1.1).

Similar to the way the Wright brothers pioneered the age of flight and the development of "large-scale" aerodynamics in the early 1900s, a century later engineers and scientists are experiencing parallels with regard to the exploration and development of "small-scale" MAV aerodynamics. As mentioned in Section 1.1, the low operational speeds associated with these vehicles results in their aerodynamic nature being classified by low Renolds numbers. To date this aerodynamic regime has been sparsely studied, with the majority of the advances owing to "trial and error" or down-scaled concepts borrowed from existing UAV designs.

For the last two decades much work has been undertaken to advance MAV capabilities (Mueller 1985), but few validated flight dynamic models are available for simulation and control studies. At this point the only guide available for designing such vehicles is to imitate what is displayed by the animal world. Biological fliers clearly demonstrate that current MAV designs fall well short when they are matched to the aerodynamic performance (stability, maneuverability and efficiency) of insects, birds and bats. This comes as no surprise due to the fact that aircraft design tools at this level are yet to be conceived.

The physical processes that govern the outstanding flight capabilities portrayed by the

fliers in nature remain unfathomable. Conventional aerodynamic theory (Nachtigall 1974; Dalton 1975; Ellington 1984, 1991; Ellington and Pedley 1995) is unable to explain the way in which an insect can transition from a backwards take-off, through a sideways flight, to an upside down landing! One of the greatest challenges is figuring out how small birds and insects can generate forces ranging from 2 to 12 times their own mass. Again, steady-state aerodynamic theory fails to interpret this enigmatic phenomenon. Recent investigations by experimental biologists indicate that a pitching/plunging wing motion permits a rapid recovery from wake vorticities, thus leading to improved efficiency for the insect (Dickinson 1996). For birds it seems that large-scale morphing of their wing geometries adds to their aerodynamic efficiency (Rayner 1988).

Past research has shown the design, building and testing of a variety of MAVs which encompass all three wing designs - fixed, rotary and flapping. Many of these projects have focused on technical issues (Nicoud and Zufferey 2002; Pines and Bohorquez 2006) but the science and design methodologies for these small-scale aircraft are still in their infancy.

At the present, particular interest in the advancement of MAV technology for operation in urban (unknown 1998; Nordwall 1997; Davis et al. 1996) and military (Hundley and Gritton 1994) environments has result in several studies by different groups. Some designs include the Black Widow (Aerovironment), Hoverfly (Aerovironment), LUMAV (Auburn Univ.), MicroStar (Lockheed-Martin), Microbat (CalTech) and MICOR (university of maryland). The literature relating to these designs (Grasmeyer and Keenon 2001; Pornsin-Sirirak et al. 2000; Michelson et al. 1997; Michelson 1998; Kornbluh 2002; Morris 1997; Cox et al. 2002; Samuel et al. 2000) reveals that the majority of current fixed wing and rotary MAV aircraft utilize battery power as an energy source, propellers or rotors as a thrust producing mechanism and conventional airfoil shapes for acquiring lift. All accept the flapping-wing Microbat, cooperatively developed by Caltech and Aerovironment, make use of conventional steady-state aerodynamic principles for creating thrust and lift.

Once at its peak, the flapping-wing design will no doubt out perform fixed and rotary wing designs - but arriving at that point means overcoming numerous challenges. A recent aerodynamic study by Chabalko et al. (2009) on flapping wing design in hover mode has resulted in another improvement in modeling and analysis techniques. They modeled the aerodynamics using a vortex particle method that includes conservation of circulation. Chabalko et al. (2009) are of the opinion that this method is capable of capturing intricate flow features while reducing the heavy computation burdens associated with complex computational fluid dynamic modeling.

To date, no validation based on flight test data has been performed (Mueller 2001). A hand full of isolated wind tunnel experiments have been carried out on small-scale wing elements (Burk 1975; Shields and Mohseni 2010), with the focus on extracting steady aerodynamic characteristics for different airfoil shapes and airspeeds. Computational fluid dynamics approaches, which are used extensively for large scale aircraft, are of limited use because their

results have not been thoroughly validated at the small-scale (Shyy et al. 2008). To date, no experiments focusing on actual aircraft flight dynamic behavior at centimeter scale have been reported. Pelletier and Mueller (2000) describe their experiments with a 2 g glider, but no actual flight data is mentioned and all the results are based on wind tunnel data.

The uniqueness of the MAV, with regard to size, flight regime and modes of operation, present numerous technical challenges that need to be overcome in order to make full use of their revolutionary capabilities. MAV research is a multidisciplinary field combining aerodynamics, MAV aerodynamics (unsteady flows), structural dynamics, aeroelasticity, control (non-linear and adaptive) and guidance and navigation. As a result significant advancements can only be made by the integration of new techniques and discoveries from all these branches of science and engineering. Thus it is imperative that in depth studies geared towards the above mentioned specialties are continually pursued in order to solve some of the current mysteries relating to MAVs.

1.3 Thesis motivation and structure

The motivation for this thesis originated from an idea by Prof. Bernie Mettler, to use her Interactive Guidance and Control Laboratory that affords vision based motion tracking capabilities, to collect flight trajectories for small fixed-wing aircraft with the purpose of advancing the current aerodynamic knowledge relating to MAVs. In general, the laboratory is used for experiments involving human/pilot interaction with regard to the guidance of rotor aircraft, but it is also an ideal environment for studying fixed-wing MAV properties.

The idea became the motivation for this thesis after a thorough literature review revealed that no other studies on the system identification of MAVs had been done using this method of direct trajectory sampling. This alternate method is unique in that it allows trajectory data from a full experimental flight to be captured as the aircraft position and attitude vary naturally throughout the flight. The aim of this study is to extract and refine aerodynamic coefficients and stability derivatives from the flight data in order to create a validated aerodynamic simulation model.

The structure of this thesis is summarized and color-coded in the MAV flow diagram (Figure 1.1). Throughout this thesis the various color blocks are referred to in order to clearly communicate the relevant position in the sequence of steps involved from data collection through to the system validation.

Chapter 2 of this thesis provides details relating to the experimental facility, the equipment and the aircraft selected for flight tests. The data collection method and basic data reduction/preparation are also included in this chapter. Chapter 3 (green block) describes the Kalman filtering process and the procedure for generating velocities and accelerations from the experimental data. The extraction of aerodynamic forces, moments, angles and

coefficients is explained in Chapter 4 (pink block).

The bulk of the analysis for this thesis is presented in Chapters 5 and 6 (blue and yellow blocks). Here the procedure for generating linear stability derivatives from the aerodynamic coefficients is discussed and carried out. Further investigation and explanation relating to flight regions of non-linearity is also presented in Chapter 5. The penultimate chapter of this thesis (Chapter 6) provides details on the system identification procedure and the maximum likelihood estimation algorithm that is used for refining the stability derivatives. A system validation with the refined stability derivatives is also performed. Finally, in Chapter 7, the main thesis ideas and results are stated and from them ultimate conclusions are draw.

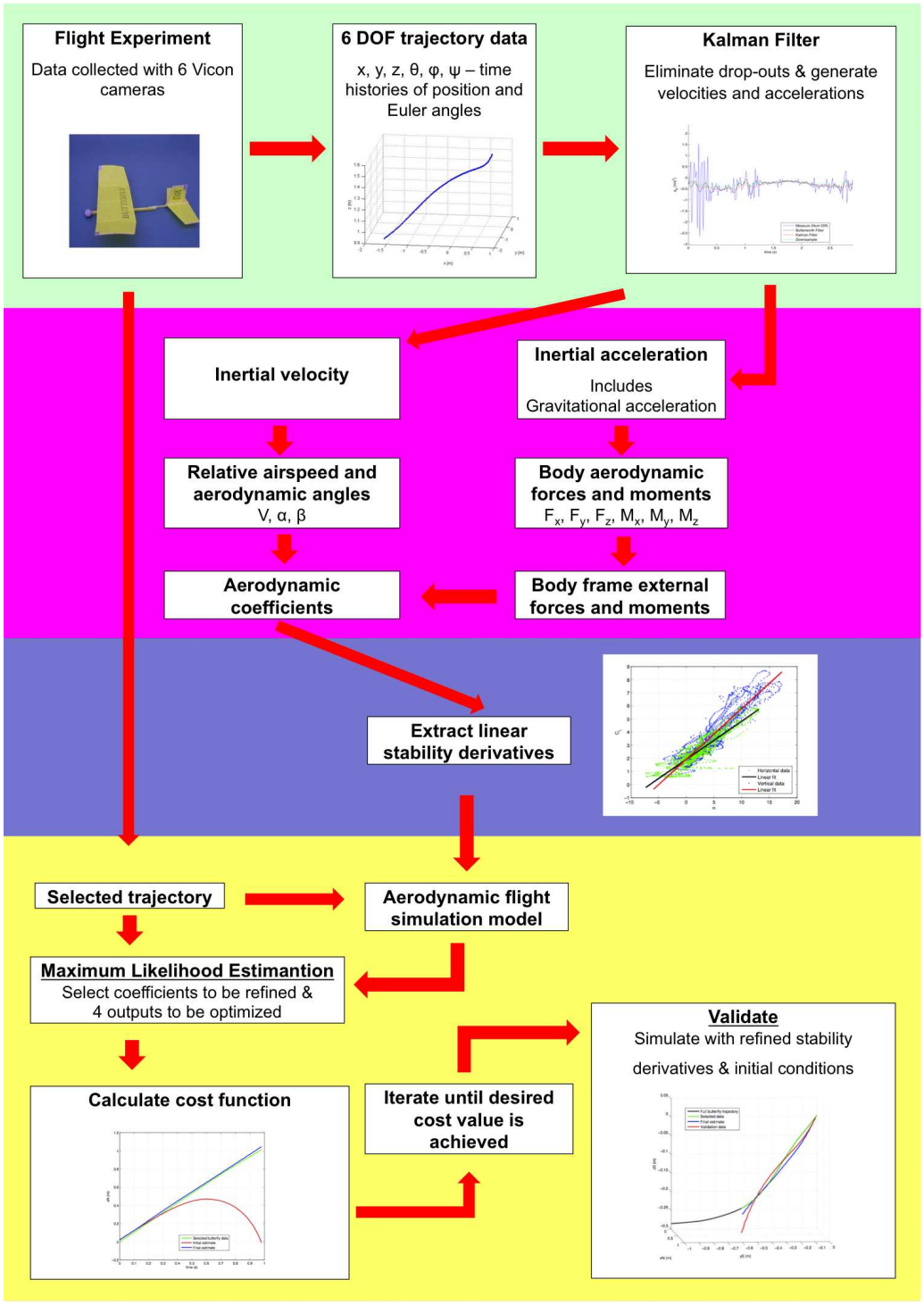

Figure 1.1: A pictorial representation of the structure for this thesis. The algorithms used in Chapter 4 (pink) were previously published by Mettler (2010).

Chapter 2

Experimental facility and data collection

This chapter describes the aircraft used for generating flight trajectory data and the laboratory equipment employed for measuring it. The Vicon tracking system, consisting of several components including six high resolution cameras, is a complicated and advanced collection of equipment that is capable of measuring data at high frequencies. A full description of this system and the favored data collection method is presented.

2.1 Butterfly aircraft

The MAV experiment was conducted with the Butterfly aircraft (Figure 2.1) developed by Plantraco (2008). The Butterfly is a simple remote controlled aircraft possessing an 18 cm polyhedral wing with a 6.6 cm chord length and an under-cambered profile. In it's usual configuration the plane embodies an electrically driven propeller and an actuated rudder. In addition, the plane is equipped with an on board receiver that processes the remote controlled commands and also makes small adjustments to the speed controller thus allowing the propeller speed to be varied.

For the data collected and analyzed in this thesis the receiver, motor and actuator were removed in order for the plane to be used as a glider in the laboratory. The physical nature and size of the laboratory environment prevents the testing of propeller driven fixed wing aircraft. In addition, chosing to fly the plane as a glider instead of as a propeller driven aircraft greatly reduces the complexity of the aerodynamics (Kundak and Mettler 2007) - a desired condition for this initial phase of the experiment. Without these three components the overall mass of the glider is 2.8 g. The silver markers (strips/sphere) visible on the tail fin, wing tips and nose in Figure 2.1 are retro-reflective markers that were added to the airframe to permit motion tracking with the Vicon camera system described in Section 2.2.

Figure 2.2 shows the Butterfly aircraft rendered in a computer assisted design (CAD) software program. This model and aircraft specifications were used for determing the moments of inertia that are required later in the analysis to calculate the aerodynamic moments from the aircraft position and attitude trajectory data (see Chapter 4).

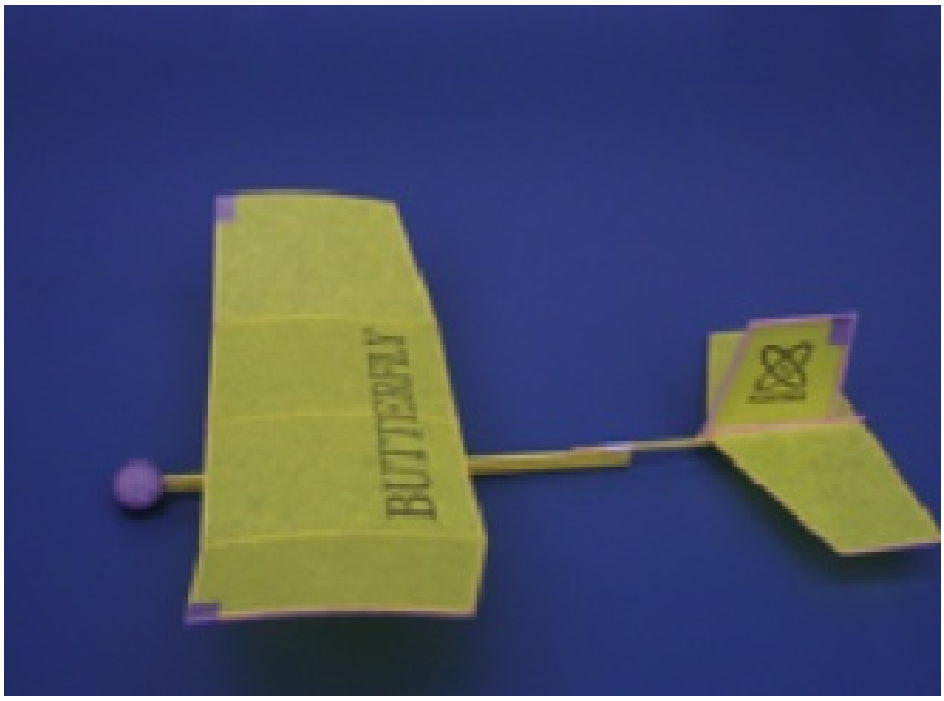

Figure 2.1: The Butterfly aircraft, with an 18 cm wingspan and a mass of 2.3 g, was used for collecting the data analyzed in this thesis. The reflective markers (5×5 mm) used for traking the inflight motion are clearly visible on the tail fin and wing tips, and a 14 mm reflective sphere is fitted to the nose (taken from Mettler (2010)).

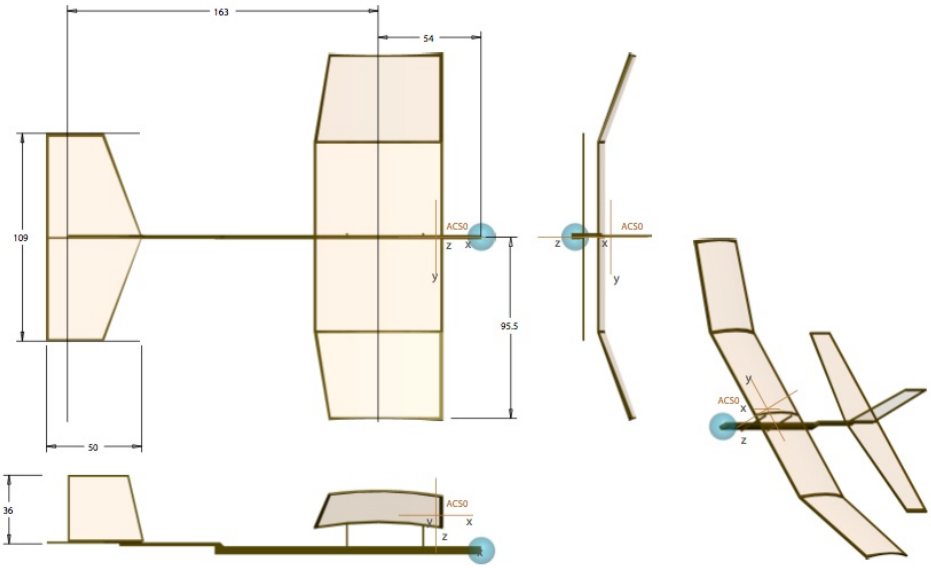

Figure 2.2: A CAD model of the Butterfly airframe which was created in order to determine the moments of inertia required for calculating the aerodynamic moments and coefficients (taken from Mettler (2010)).

2.2 Experimental facility and Motion tracking system

The experimental facility consists of an indoor space of about $7 \times 7 \times 2.5$ meters equiped with a complex motion tracking system. The main components of the motion tracking system are six MX-40 high resolution 10-bit grey scale Vicon cameras (Vicon 2006), a router and a computer running ViconIQ software. Each camera has dimensions of 2352×1728 pixels and is fixed to the wall. Inside the laboratory the effective tracking volume produced by the six camreas is about $5 \times 5 \times 2$ meters. The red ring on the camera shown in Figure 2.3 is composed of an array of light emitting diodes (LEDs). The purpose of these LEDs is to enhance the reflection off the markers fixed to the aircraft so that it can be more easily tracked during a flight.

Before collecting a series of trajectories the approximate geometry of the marker configuration must be put into the tracking software system. Using these geometric positions the ViconIQ software makes a calibration and creates an accurate model of the marker configuration in the computer. This model configuration produces a rigid-body system for the aircraft that is used to provide an estimate of the aircraft's six degree of freedom motion during the real time motion tracking of the flight. Figure 2.4 shows a wireframe model of the aircraft's maker configuration produced by the ViconIQ software.

A local network is set up in the laboratory to link the information from the six Vicon cameras through the router to the computer running the ViconIQ software. Some image pre-processing is done on-board the cameras prior to it being routed to the computer. This involves a computation, for each of the six cameras respectively, of the marker coordinates from the reflections detected in each image frame. Following this the pre-processed data is transferred to the computer where it is then processed to calculate the 3-dimensional position of the markers in the laboratory space. Figure 2.5 displays the computer representation of the Vicon workspace for tracking these flights.

As part of the motion tracking system the camera configuration is automatically calibrated in order to determine the orientations and locations of each camera with respect to the spatial reference system origin. Published values for the tracking accuracy of the cameras are 0.1 deg in rotation and 40 µm in translation, and the system also has the ability to collect full image resolution data at frequencies up to 166 image frames per second. Further details on the Vicon tracking system may be obtained by referring to Vicon (2006).

Figure 2.3: The 4 mega pixel MX-40 Vicon camera operates at frequencies up to 166Hz (frames per second). Near infrared LED light (red ring in image) was used to enhance the tracking performance of the six cameras installed in the lab (taken from Mettler (2010)).

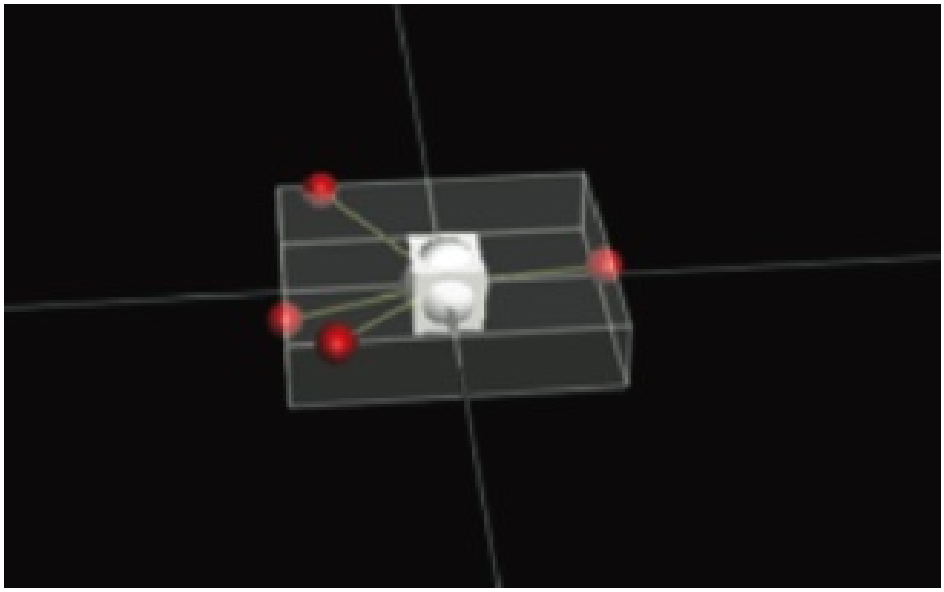

Figure 2.4: The wireframe model of the marker configuration (from aircraft in Figure 2.1) is created by the computer during the initial set-up and calibration prior to each launch (taken from Mettler (2010)).

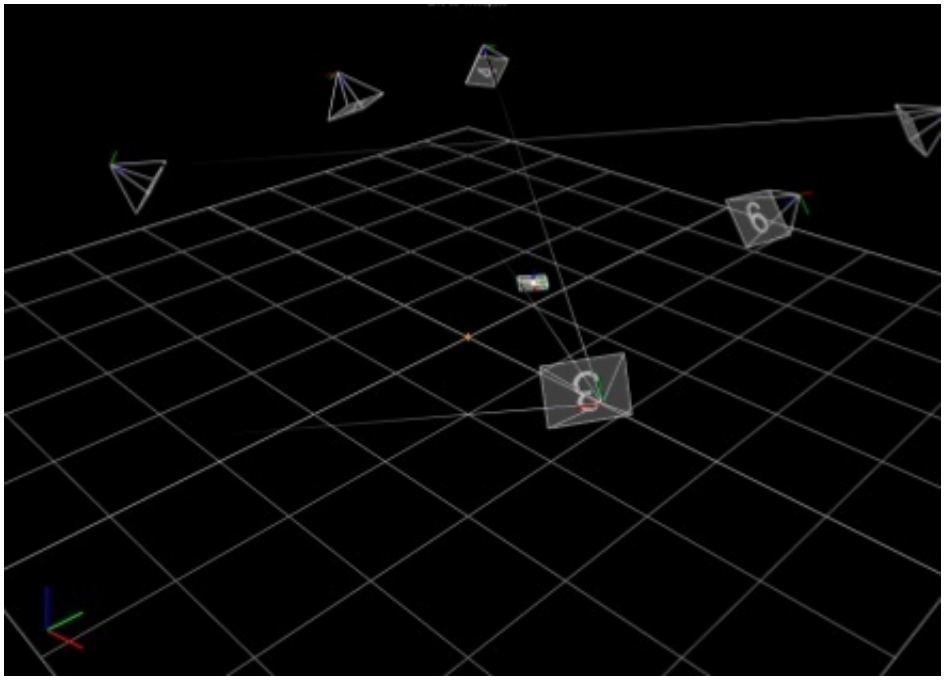

Figure 2.5: The workspace created by the six Vicon cameras. The aircraft to be tracked is the small "boxed" object close to the center of the tracking field (taken from Mettler (2010)).

2.3 Flight data collection

Once the tracking system has been switched on and the computer has generated the "wire-frame" model of the aircraft, a series of flight data may be collected. As previously mentioned the plane is flown like a glider in the laboratory which has enabled a wide variety of flight conditions to be explored. The plane is hand-launched with the appropriate initial speed, and angles to achieve the desired flight conditions. To date, the types of trajectories achievable using this procedure cover a range from rectilinear helical glides to non-equilibrium maneuvers (transitions in and out of stalls - Mettler (2010)). Depending on the initial flight conditions and the way in which the glider is trimmed, flights may begin at a non-equilibrium state (out of balance - demonstrated by turbulent flow) and transition to an equilibrium state (in balance - laminar flow) and vice versa.

The raw trajectory, as provided by the Vicon tracking system, is described in terms of the time histories of the three position coordinates (x_{N}, y_{E}, z_{D}) in the reference body frame, and the three Euler angles (φ - roll, ϑ - pitch, ψ - yaw). Figure 2.6 shows an ensemble of trajectories collected during two separate experimental sessions. The green data (lateral-directional motion) and the blue data (vertical-longitudinal motion) were acquired at different times and have been shifted in order for the initial launch location to coincide. Figure 2.7 displays a sequence of images taken during a stall, and Figure 2.8 shows the stall data plotted along with the body axis position reference frame superimposed at 0.1 s intervals respectively.

Once these position and angular measurements have been (automatically) extracted from the Vicon images they are mathematically filtered (see Chapter 3) prior to being used in the aerodynamic equations (Crassisis and Junkins 2004) to determine the aerodynamic coefficients (see Chapter 4) which are required for the remainder of the analysis.

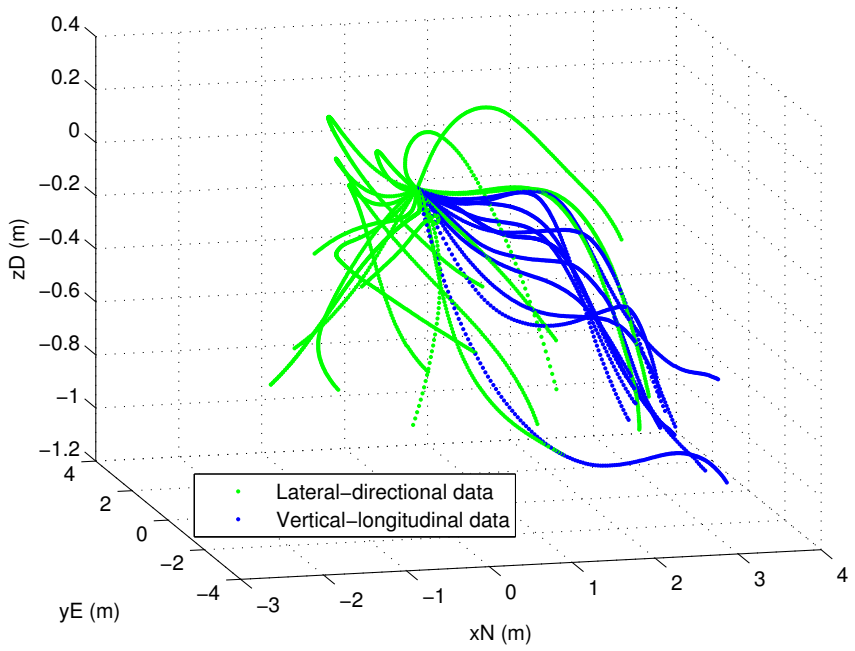

Figure 2.6: A sample of flight trajectories obtained with the butterfly aircraft and the Vicon motion tracking system. The green trajectories correspond to flights with a dominant lateral-directional motion (turns) whereas the blue trajectories correspond to flights dominating in the vertical-longitudinal direction.

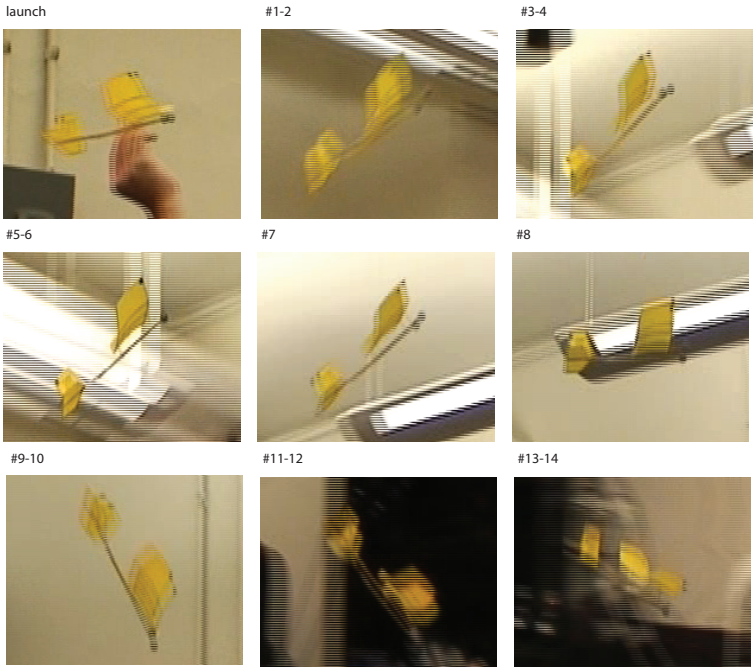

Figure 2.7: A sequence of images for the stall trajectory shown in Figure 2.8. The image numbers correspond to the numbers shown on the trajectory in Figure 2.8 and were extracted by hand based on the position and attitude data time histories (taken from Mettler (2010)).

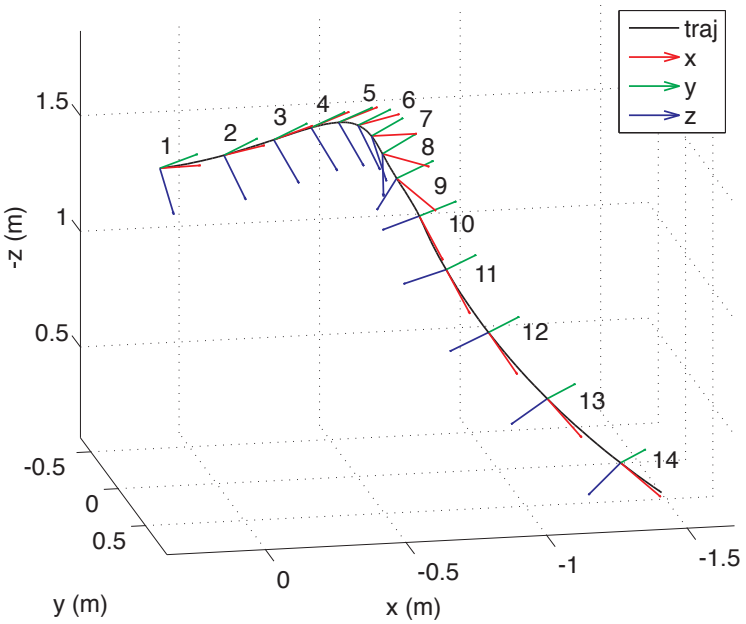

Figure 2.8: Body reference axis superimposed on the stall trajectory at time intervals of 0.1 s (taken from Mettler (2010)).

2.4 Summary of the experimental facility

The material covered in this chapter sets the stage for the remaining chapters in this thesis. A description of the aircraft, laboratory equipment and data collection method required for generating the flight data are presented. A minor automated data reduction is undertaken by the Vicon cameras discussed in this chapter but the majority of the data preparation and filtering is performed in the following chapter.

Chapter 3

Data filtering

This chapter presents a detailed explanation of the chosen data filtering method, the Kalman filter, and the procedure for generating the linear and angular velocities and accelerations from the position and attitude data acquired in Chapter 2. All the steps shown in the green section of the MAV experiment flow diagram in Chapter 1 are covered in this chapter.

3.1 Kalman filter description

The Kalman filter, named after Rudolf E. Kalman, is a mathematical algorithm that utilizes observed noisy measurements with the aim of producing values that are more representative of the true values for these measurements (Kalman and Bucy 1961). Put simply, the Kalman filter makes an estimate of the true value by predicting a value, it guesses the respective uncertainty of the predicted value, and then calculates the weighted mean of the measured and predicted values.

To elaborate, the Kalman filter requires a kinematic/dynamic model of the system, measurements from sensors, and some knowledge of the control inputs, in order to produce an estimated measure of the system's time dependent characteristics. Fusing the information from all three sources (dynamic model, sensor measurements and control inputs) together in one mathematical algorithm results in better estimates than using only the information from one source.

It is assumed that calculations and measurements obtained from models are always estimates - to some extent. Uncertainty is introduced into a modeled system by means of noisy data, approximations in the equations used to characterize systemic variations, and external effects that are neglected. As mentioned previously, the Kalman filter employs a weighted mean computation to predict the state of a system at a given instant in time. The weight of each predicted value is calculated from the covariance which is a measure of the estimated uncertainty of the predicted state of the system (Stengle 1994). The weighted mean results in a new state estimate for the system that falls between the measured and predicted state,

and has a more reliable associated uncertainty than either of the predicted and measured uncertainties alone. The procedure described above is repeated at every time increment with the most recent estimate and associated covariance forming the basis of the prediction for the proceeding iteration. Thus the Kalman filter may be described as a recursive filter since only the last prediction is required for a new system state to be calculated, not all the previous state estimates.

In reality, the calculations are performed with covariance and state estimate matrices so that multiple dimensions can be included in each step of the process. This means that the relationship between the various state variables (i.e. position, velocity and acceleration) may be represented linearly in any of the covariances or intra-computation models.

The Kalman filter is usually portrayed as two separate phases: a predict phase (a priori state estimate) and an update phase (a posteriori state estimate). While the algorithm is in operation the phases alternate between predict and update. The predict phase continues to advance the state until the next available observation, upon which it updates the state of the system, including in the computation the observed data at that point (Lewis 1986). If for some reason an observation is missing, the update step may be omitted allowing multiple prediction steps to occur in succession. Similarly, if several unique observations are present at one particular time instant, multiple update steps may occur prior to switching back to the predict phase.

3.2 Kalman filter algorithm

All the data analyzed for this thesis were filtered using a Kalman filter algorithm coded in matlab. The kinematic models chosen to describe the physical behavior of the system are the Wiener process velocity and acceleration models (Bar-Shalom et al. 2001; Crassisis and Junkins 2004). The following models in continuous-time depict the aircraft's linear (Equation 3.1) and angular rates (Equation 3.2) respectively:

$$\frac{d}{dt}\begin{bmatrix} x \\ \dot{x} \\ \ddot{x} \end{bmatrix} = \begin{bmatrix} 0 & 1 & 0 \\ 0 & 0 & 1 \\ 0 & 0 & 0 \end{bmatrix}\begin{bmatrix} x \\ \dot{x} \\ \ddot{x} \end{bmatrix} + \begin{bmatrix} 0 \\ 0 \\ 1 \end{bmatrix} v(t) \tag{3.1}$$

and

$$\frac{d}{dt}\begin{bmatrix} \theta \\ \dot{\theta} \\ \ddot{\theta} \end{bmatrix} = \begin{bmatrix} 0 & 1 & 0 \\ 0 & 0 & 1 \\ 0 & 0 & 0 \end{bmatrix}\begin{bmatrix} \theta \\ \dot{\theta} \\ \ddot{\theta} \end{bmatrix} + \begin{bmatrix} 0 \\ 0 \\ 1 \end{bmatrix} v(t), \tag{3.2}$$

where $v(t)$ is the process noise with a variance q.

The discrete-time process models for the linear (Equation 3.3) and angular (Equation 3.4) rates are given by:

$$\begin{bmatrix} x_{k+1} \\ \dot{x}_{k+1} \\ \ddot{x}_{k+1} \end{bmatrix} = \overbrace{\begin{bmatrix} 1 & T & \frac{T^2}{2} \\ 0 & 1 & T \\ 0 & 0 & 1 \end{bmatrix}}^{\Phi} \begin{bmatrix} x_k \\ \dot{x}_k \\ \ddot{x}_k \end{bmatrix} + \overbrace{\begin{bmatrix} 0 \\ 0 \\ 1 \end{bmatrix}}^{G} v_k, \tag{3.3}$$

and

$$\begin{bmatrix} \theta_{k+1} \\ \dot{\theta}_{k+1} \\ \ddot{\theta}_{k+1} \end{bmatrix} = \overbrace{\begin{bmatrix} 1 & T & \frac{T^2}{2} \\ 0 & 1 & T \\ 0 & 0 & 1 \end{bmatrix}}^{\Phi} \begin{bmatrix} \theta_k \\ \dot{\theta}_k \\ \ddot{\theta}_k \end{bmatrix} + \overbrace{\begin{bmatrix} 0 \\ 0 \\ 1 \end{bmatrix}}^{G} v_k, \tag{3.4}$$

where T is the sampling time.

The discrete-time measurement models for the linear and angular cases are shown in Equation 3.5 and Equation 3.6:

$$z_k = \overbrace{\begin{bmatrix} 1 & 1 & 1 \end{bmatrix}}^{H} \begin{bmatrix} x_{k+1} \\ \dot{x}_{k+1} \\ \ddot{x}_{k+1} \end{bmatrix} + \eta_k \tag{3.5}$$

and

$$z_k = \overbrace{\begin{bmatrix} 1 & 1 & 1 \end{bmatrix}}^{H} \begin{bmatrix} \theta_{k+1} \\ \dot{\theta}_{k+1} \\ \ddot{\theta}_{k+1} \end{bmatrix} + \eta_k. \tag{3.6}$$

Following this the covariance of the discrete-time process noise Q_k can be obtained by taking the integral (Equation 3.7) over a sampling period,

$$Q_k = \int_0^T \Phi(\tau) G q G^T \Phi(\tau) d\tau \tag{3.7}$$

$$Q_k = q \begin{bmatrix} \frac{1}{20}T^5 & \frac{1}{8}T^4 & \frac{1}{6}T^3 \\ \frac{1}{8}T^4 & \frac{1}{3}T^3 & \frac{1}{2}T^2 \\ \frac{1}{6}T^3 & \frac{1}{2}T^2 & T \end{bmatrix}. \tag{3.8}$$

The Kalman filter time propagation (predict phase) for the state vector x and the covariance matrix P are defined as follows;

- predicted (a priori) state estimate:

$$x_{k+1}^{-} = \Phi_k x_k^{+} \tag{3.9}$$

- predicted (a priori) estimate covariance:

$$P_{k+1}^{-} = \Phi_k P_k^{+} \Phi_k^T + Q_k. \tag{3.10}$$

The measurement update continues with a computation of the Kalman gain;

- measurement residual:

$$r = z_k - H x_{k+1}^{-} \tag{3.11}$$

- residual covariance:

$$S = (H P^{-} H^T + R) \tag{3.12}$$

- Optimal Kalman gain:

$$K = P^{-} H^T S^{-1} \tag{3.13}$$

where the variance of the measurement noise is given by R. Finally, an update of the state and error covariance matrix is made as follows:

$$\hat{x}^{+} = \hat{x}^{-} + Kr \tag{3.14}$$

and

$$P^{+} = (I - KH) P^{-} (I - KH)^T + KRK^T. \tag{3.15}$$

3.2.1 Tuning the filter

In the algorithm presented in Equations 3.1 through 3.15 there are two free parameters: R - the measurement variance noise, and q - the process noise variance. The measurement noise variance may be obtained from the sensor specifications (see Mettler (2010)), which leaves the process noise variance as the only parameter that may be varied to tune the filter output. According to Equations 3.7 and 3.8 the changes in velocity and acceleration over the sampling period are of the order $\sqrt{qT}$, which may be used as a guide for the initial selection of q. In addition, the $3-\sigma$ covariance bound of the residuals is monitored to ensure filter consistency (Figures 3.7 and 3.8), and if an inconsistency is detected q is modified

accordingly to obtain satisfactory results. The autocorrelation (Figures 3.9 and 3.10) of the residuals are also checked to ensure that they are approximately white noise.

3.3 Kalman filter outputs

The raw Vicon position and orientation data for the butterfly aircraft is used in the Kalman filter algorithm to produce reliable velocity and acceleration measurements for each data point along the flight trajectory. For the original analysis Mettler (2010) a Butterworth 8th order filter with a sampling frequency of 30 Hz was used to filter the data. Following this filtering process, the data was numerically differentiated to obtain velocities and accelerations. This method of numerical differentiation greatly amplifies errors near drop-out zones in the data, which is the main reason for implementing a Kalman filter as part of this thesis.

The Kalman filter requires a starting point or an initial estimate to allow it to propagate forward and generate the next point. For the positions and orientations the first raw data point was used as an initial guess and the algorithm proceeded from there. For the velocities and accelerations an average of the first data point obtained by means of numerical differentiation, down sampled numerical differentiation and the Butterworth filter was used as a starting point. This method proved successful and is illustrated in Figures 3.1 through 3.10 using the butterflyJan10_01 flight trajectory.

Figures 3.1 and 3.2 show excellent agreement between the measured data (blue), and the data after applying with the Butterworth (black) and Kalman (red) filters respectively. Figures 3.3 and 3.4 show the linear and angular velocities obtained by numerical differentiation (blue), the Butterworth filter (black), the Kalman filter (red) and by down sampled numerical differentiation (green). Similarly, the linear and angular acceleration data is displayed in Figures 3.5 and 3.6. It is clear that implementation of the Kalman filter greatly reduces the amount of noise that is evident in the velocity and acceleration plots compared with the other three filtering procedures. However, in order to mathematically qualify this statement a series of residual and autocorrelation plots were created for the respective velocities and accelerations. A selection is shown in Figures 3.7 through 3.10. These figures display residuals that fall well within the $3-\sigma$ bound and autocorrelation profiles that reveal a prominent peak, thus providing weight to the statements above. As mention previously, these plots were also used as a guide for tuning the Kalman filter until satisfactory results were achieved.

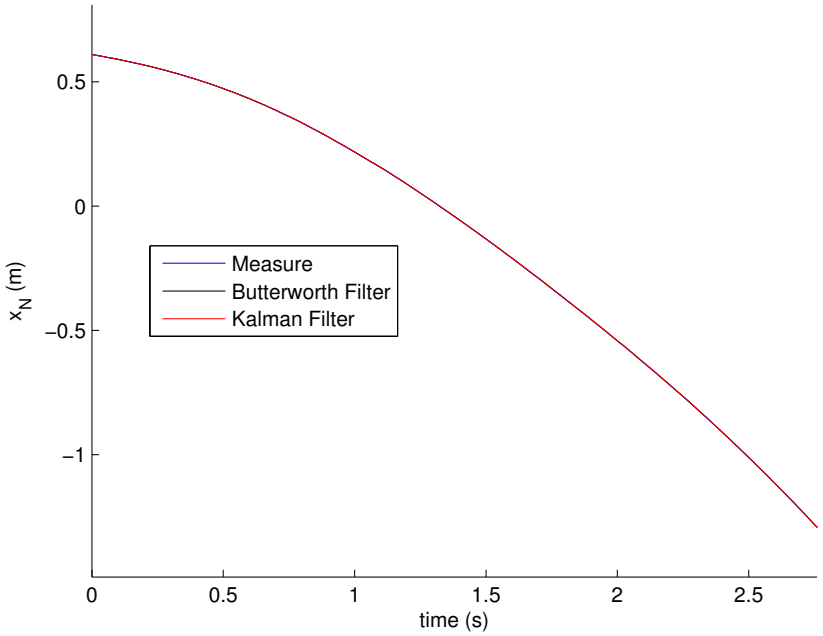

Figure 3.1: Time history of the linear position (x_N) along a butterfly flight trajectory.

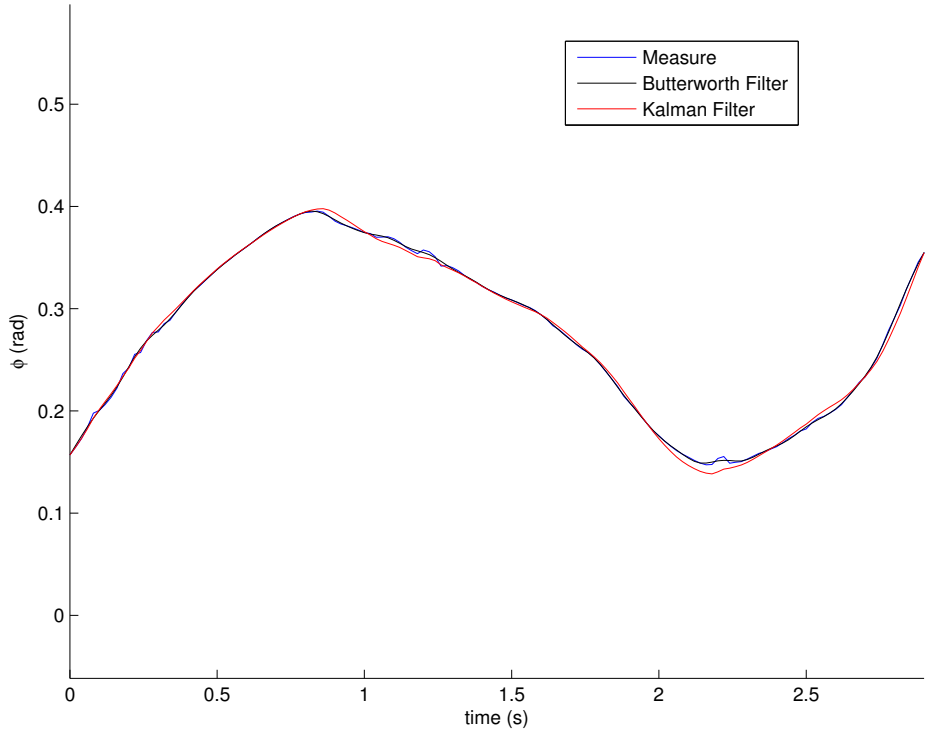

Figure 3.2: Time history of the roll angle (ϕ) along a butterfly flight trajectory.

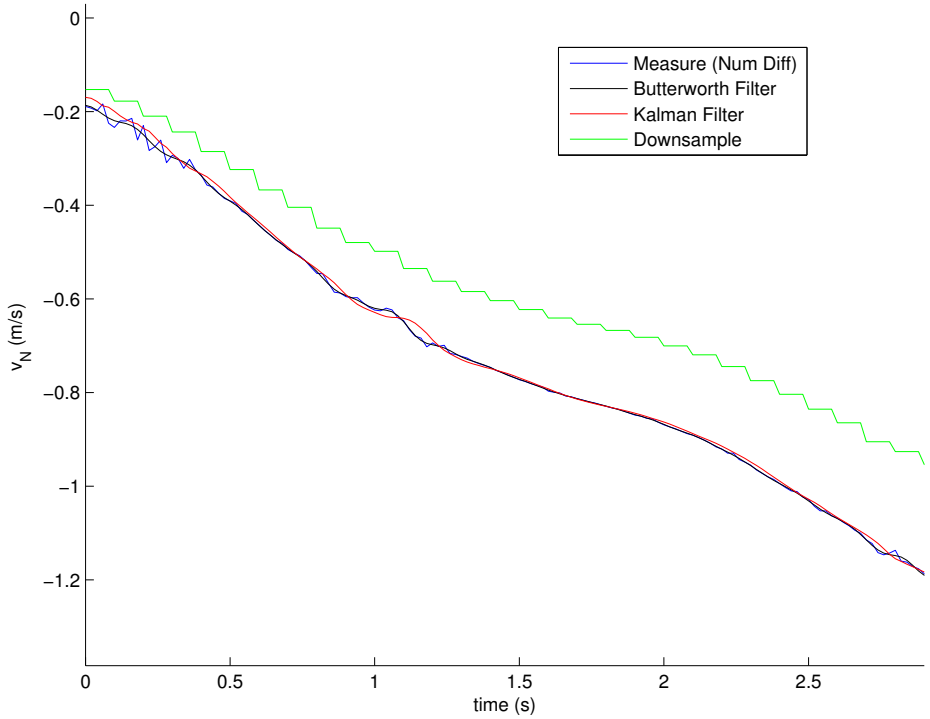

Figure 3.3: Time history of the linear velocity (v_N) along a butterfly flight trajectory.

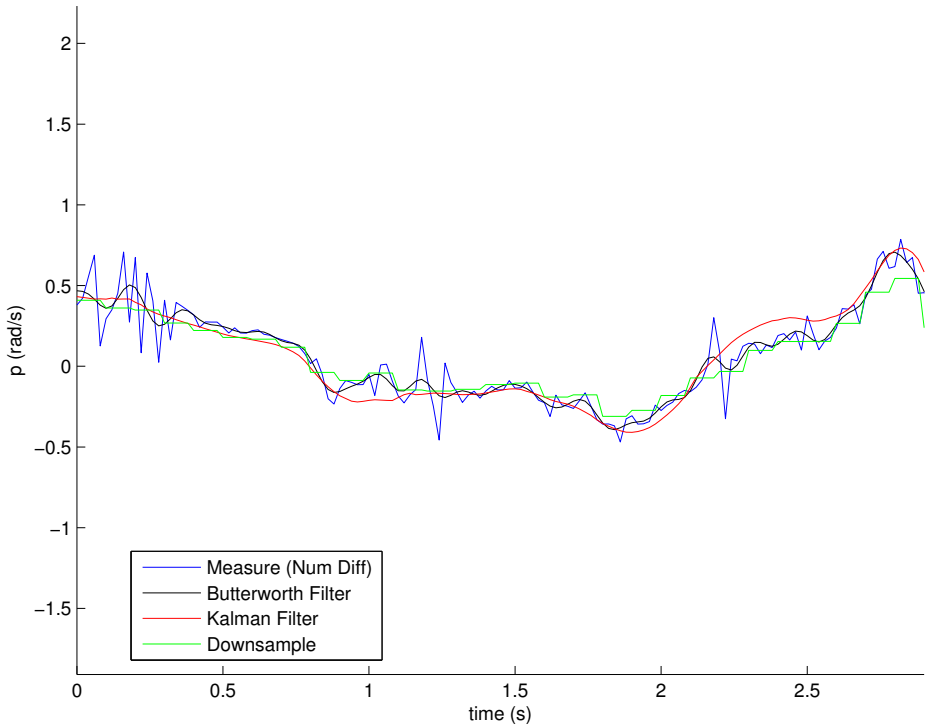

Figure 3.4: Time history of the roll velocity (p) along a butterfly flight trajectory.

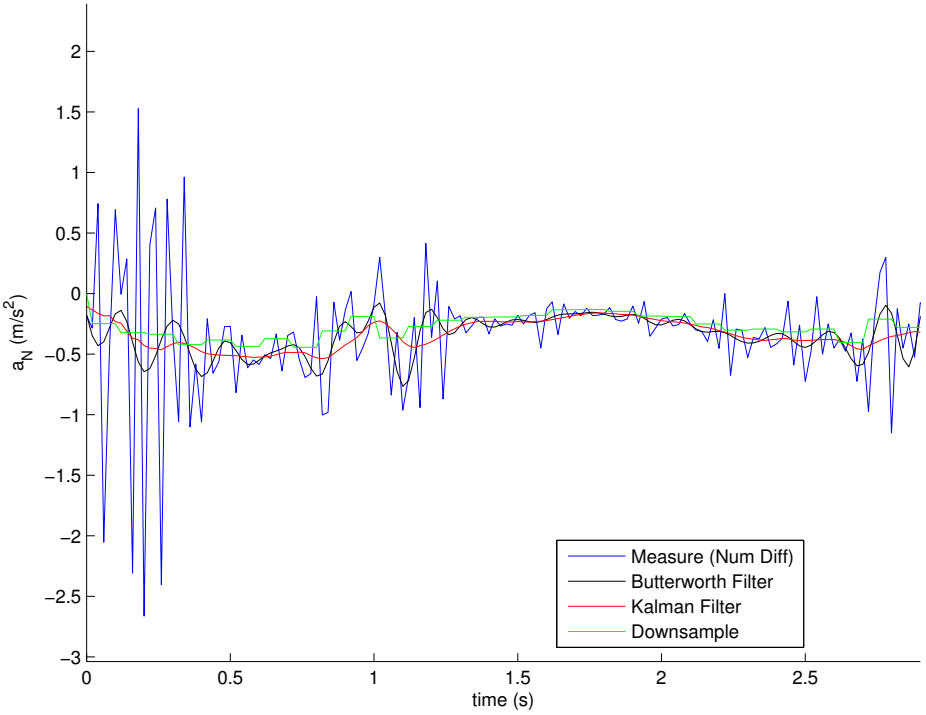

Figure 3.5: Time history of the linear acceleration (a_N) along a butterfly flight trajectory.

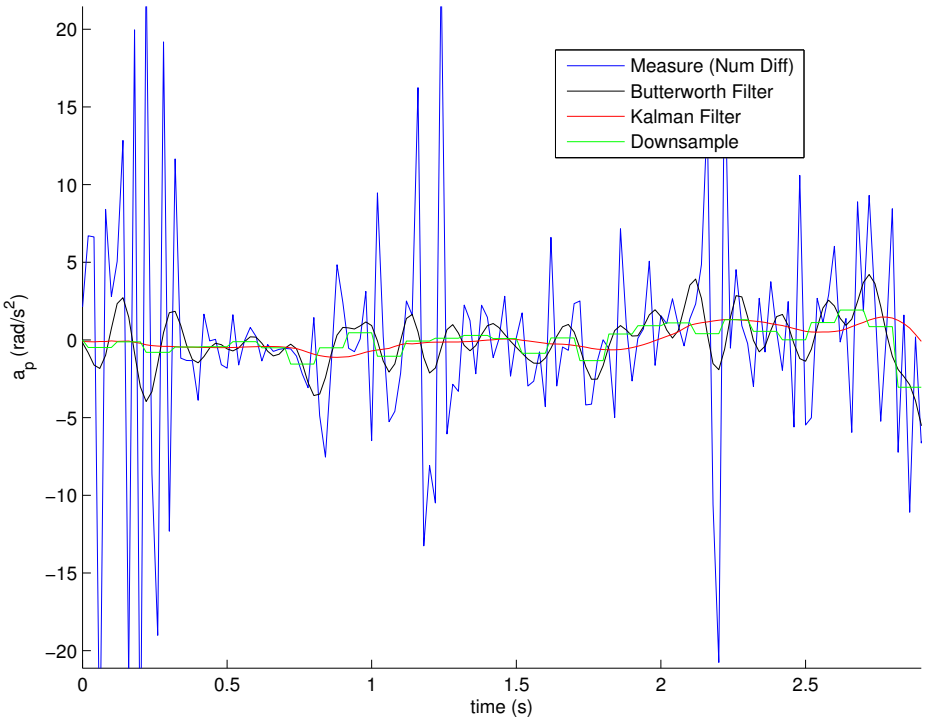

Figure 3.6: Time history of the roll acceleration (a_p) along a butterfly flight trajectory.

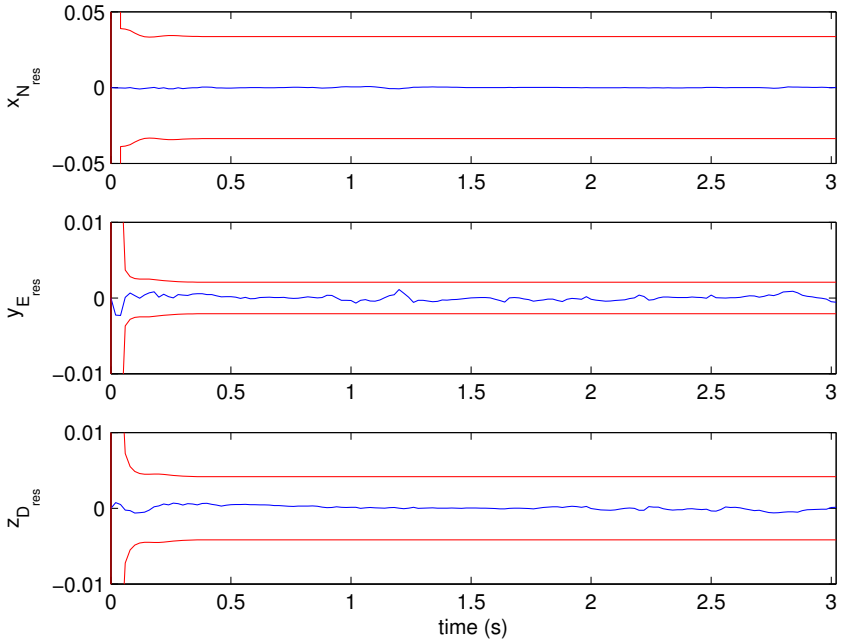

Figure 3.7: Position residuals for x_N (top panel), y_E (middle panel) and z_D (bottom panel). The red lines represent the 3σ limit.

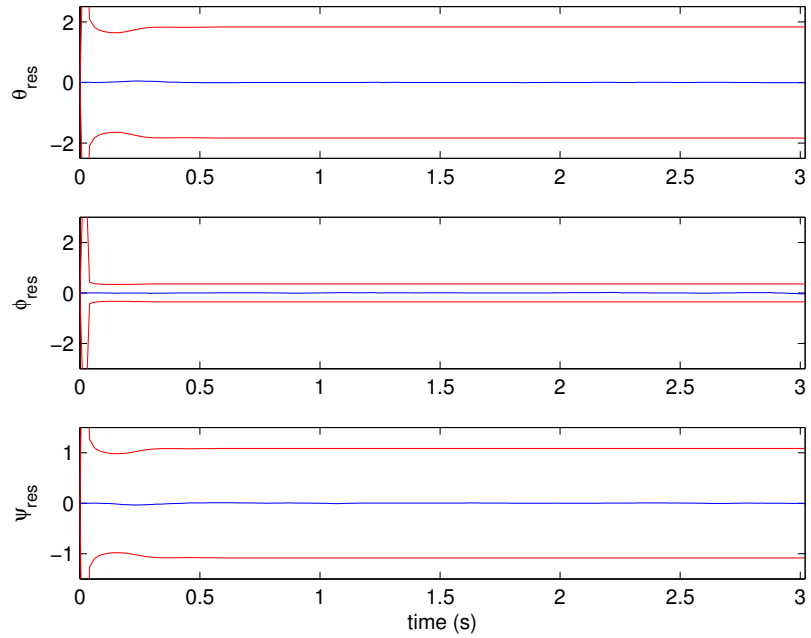

Figure 3.8: Attitude residuals for ϕ (top panel), θ (middle panel) and ψ (bottom panel). The red lines represent the 3σ limit.

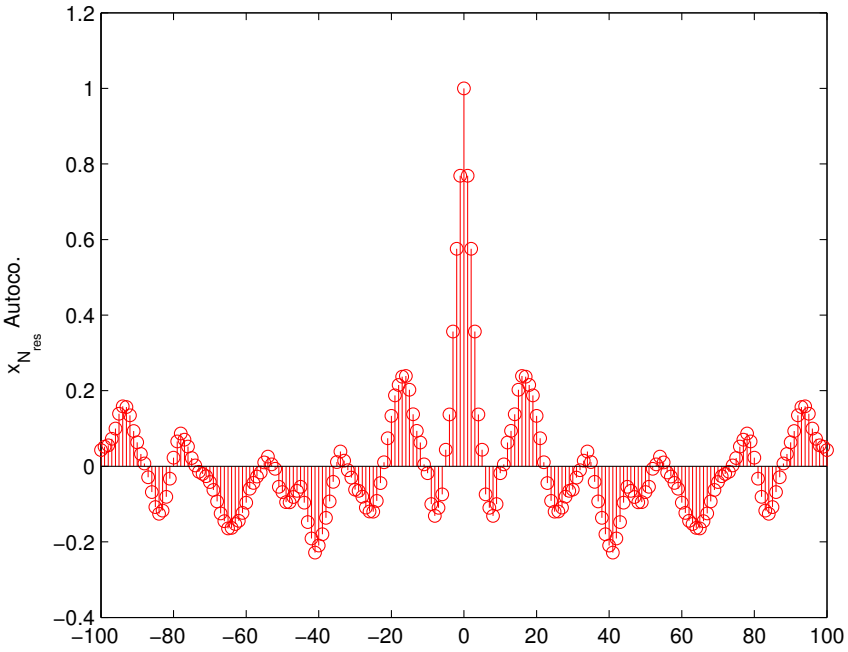

Figure 3.9: The autocorrelation profile for x_N.

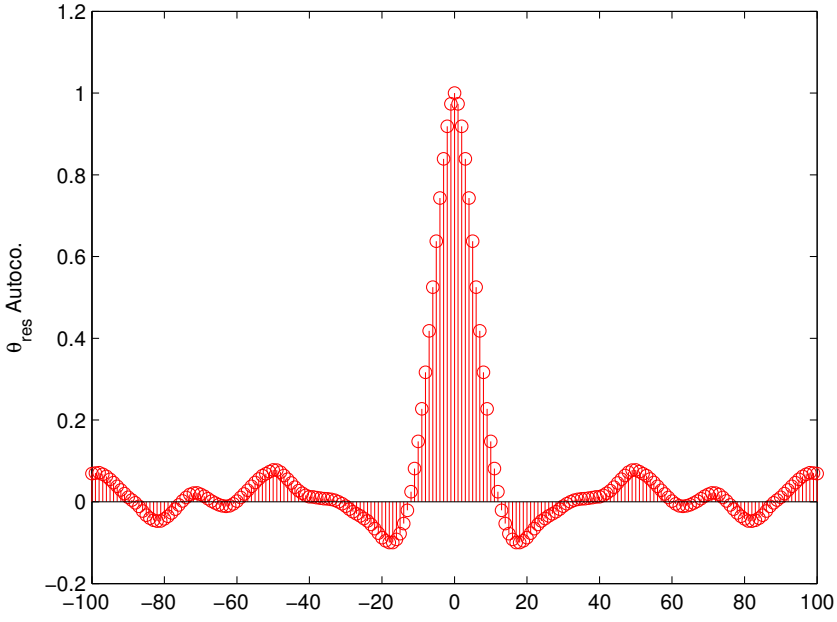

Figure 3.10: The autocorrelation profile for θ.

3.4 Summary of the Kalman filter

This chapter gives a general description of the Kalman filter and a specific explanation of the way in which it was implemented on the Butterfly MAV flight data to generate linear and angular velocities and accelerations. In this way the velocities and accelerations are not calculated numerically and amplified errors caused by data drops-outs are eliminated. A critique of the post-filter results is performed by generating residual and autocorrelation plots. The filtered data is required for the generation of aerodynamic coefficients in the following chapter.

Chapter 4

MAV aerodynamics

The previous chapter described a journey through the green block (MAV experiment diagram, Chapter 1) that lead to the production of mathematically filtered linear and angular positions, velocities and accelerations. This chapter describes the next phase of the analysis (pink block) where aerodynamic forces, moments, angles and coefficients are extracted from these data. It is a detailed and complex procedure requiring several steps. The aerodynamic equations, assumptions and procedure necessary for performing the extraction are presented in this chapter.

4.1 Coordinate transformation

Before the linear and angular velocities and accelerations calculated in Chapter 3 can be used to derive the aerodynamic coefficients, they need to be transformed from the room-referenced (inertial) frame into the aircraft body reference frame. This coordinate transformation is performed using the standard rotation matrix (Equation 4.1) that is associated with the $\Theta = [\phi\theta\psi]^T$ Euler rotations (Stevens and Lewis 1992).

$$R(\Theta) = \begin{bmatrix} cos\theta cos\psi & sin\psi cos\theta & -sin\theta \\ -sin\psi cos\phi + sin\theta sin\phi cos\psi & sin\psi sin\phi sin\theta + cos\phi cos\psi & cos\theta sin\phi \\ sin\psi sin\phi + cos\phi sin\theta cos\psi & -cos\psi sin\phi + sin\theta cos\phi sin\psi & cos\phi cos\theta \end{bmatrix}. \quad (4.1)$$

To give an example, the velocities in the body frame are computed as follows:

$$v_b = [uvw]^T = R \cdot [v_N v_E v_D]^T . \quad (4.2)$$

4.2 Extraction of aerodynamic forces and moments

The following two figures define some of the aircraft angles and forces that are used in the equations presented in this chapter.

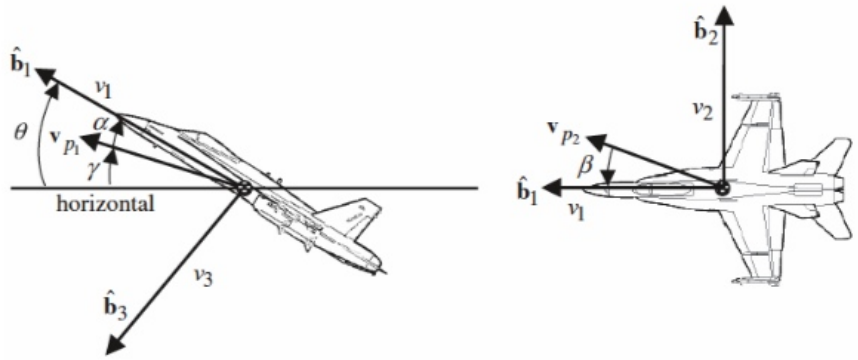

Figure 4.1: Definition of various aircraft angles (taken from Crassisis and Junkins 2004).

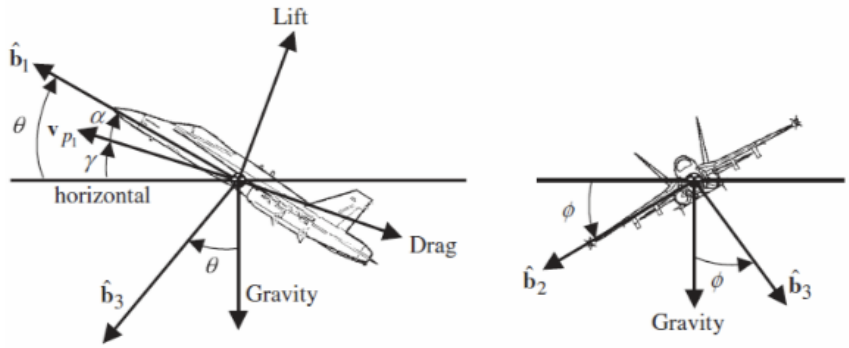

Figure 4.2: Aircraft forces (taken from Crassisis and Junkins 2004).

The angle of attack (α) is given by the angle between $\hat{\mathbf{b}}_\mathbf{1}$ and $\mathbf{v_{p1}}$ (free-stream velocity vector) on the $\hat{\mathbf{b}}_\mathbf{1} - \hat{\mathbf{b}}_\mathbf{3}$ (body axis) plane. Similarly, the side-slip angle (β) is the angle between $\hat{\mathbf{b}}_\mathbf{1}$ and $\mathbf{v_{p2}}$ on the $\hat{\mathbf{b}}_\mathbf{1} - \hat{\mathbf{b}}_\mathbf{2}$ plane. The flight path angle (γ) is defined as the angle between the horizon and the $\mathbf{v_{p1}}$ axis, and the pitch angle (θ) is the angle between the horizon and the $\hat{\mathbf{b}}_\mathbf{1}$ body axis. Finally, the roll angle (ϕ) is the angle between the horizon and the $\hat{\mathbf{b}}_\mathbf{2}$ body axis.

According to Newton's second law the sum of the external forces and moments acting on the aircraft must be equal to the aircraft's change in linear and angular momentum with respect to time (Stengle 2004). When the atmospheric disturbances are neglected, as can

be done in our controlled indoor environment using a propulsionless aircraft, the inertial acceleration of the aircraft is simply made up of the gravitational forces and aerodynamic forces alone. Thus the rigid-body equations of motion used to describe the translational and rotational aircraft motion are as follows:

$$\frac{d(m\mathbf{v})}{dt} = F_{\text{ext}}(t) = F_{\text{aero}}(t) + F_{\text{gravity}}(t); \tag{4.3}$$

$$\frac{d(\mathbf{I}w)}{dt} = M_{\text{ext}}(t) = M_{\text{aero}}(t), \tag{4.4}$$

where m represents the aircraft mass and $\mathbf{I}$ represents the moment of inertia expressed in the inertial frame. Since the gravitational force in Equation 4.3 is known, the aerodynamic forces may simply be calculated as follows, where v is the linear velocity obtained from the data.

$$F_{\text{aero}}(t) = m\frac{d^2\mathbf{v}}{d^2t} - F_{\text{gravity}}. \tag{4.5}$$

In the inertial frame the matrix of inertia is dependent upon the Euler angles and therefore it is more convenient to calculate the aerodynamic moments in the body-fixed frame (where $\mathbf{I_B}$ is constant):

$$\mathbf{I_B}\frac{d^2w_B(t)}{d^2t} = M_{\text{aero}}(t) + w_B \times \mathbf{I_B}w_B. \tag{4.6}$$

The body angular rate ($\mathbf{w_B}$) is computed from the Euler-angle rate in the following way:

$$w_B(t) = \begin{bmatrix} p(t) \\ q(t) \\ r(t) \end{bmatrix} = \begin{bmatrix} 1 & 0 & -\sin\theta \\ 0 & \cos\phi & \sin\phi\cos\theta \\ 0 & -\sin\phi & \cos\phi\cos\theta \end{bmatrix} \cdot \begin{bmatrix} \dot{\phi} \\ \dot{\theta} \\ \dot{\psi} \end{bmatrix}. \tag{4.7}$$

Using the CAD model displayed in Chapter 2, the inertia tensor for the body-frame coordinates is given by Equation 4.8.

$$\mathbf{I_B} = \begin{bmatrix} 4.06 & -0.1 & -0.58 \\ -0.1 & 10.3 & 0.001 \\ -0.53 & 0.001 & 16.8 \end{bmatrix} 10^{-6}\text{kg m}^2. \tag{4.8}$$

The next step is to use the rotation matrix (R) to convert the aerodynamic forces into the body frame. These may be computed as follows:

$$X_{\text{aero}} = [F_xF_yF_z] = R \cdot F_{\text{aero}}. \tag{4.9}$$

4.3 Computing aerodynamic angles

For the butterfly flights, the airspeed is set equal to the ground speed because there are no significant atmospheric disturbances in the laboratory environment. Thus the airspeed is calculated to be:

$$\mathbf{V}(t) = \sqrt{u(t)^2 + v(t)^2 + w(t)^2}. \tag{4.10}$$

The aerodynamic angles are simply given by:

- angle of attack

$$\alpha(t) = arctan\frac{w(t)}{u(t)} \tag{4.11}$$

and

- side-slip angle

$$\beta(t) = arcsin\frac{v(t)}{\mathbf{V}(t)}. \tag{4.12}$$

The aerodynamic forces, moments and angles computed above provide enough information to proceed with the determination of the aerodynamic coefficients.

4.4 Determining aerodynamic coefficients

Each butterfly trajectory is made up of a sequence of data points spaced at regular time intervals. The previous equations in this chapter allow a force and a moment to be calculated at each of these points along the trajectory.

The body force can be broken down into three components, the normal force N=-F_z, the axial force A=-F_x and the side-force Y=-F_y. The drag (D) and lift (L) forces are defined as being parallel and perpendicular to the relative airflow (Anderson 2001) and are given below:

$$D = Nsin\alpha - Acos\alpha, \tag{4.13}$$

and

$$L = Ncos\alpha - Asin\alpha. \tag{4.14}$$

The non-dimensional aerodynamic coefficients (Equations 4.15 through 4.20) may be calculated directly from the kinematic and dynamic variables. These are the drag coefficient, the side-force coefficient and the lift coefficient respectively (Crassisis and Junkins 2004).

$$C_D = \frac{2D}{\rho \mathbf{V}^2 A_{AC}}, \tag{4.15}$$

$$C_Y = \frac{2Y}{\rho \mathbf{V}^2 A_{AC}}, \tag{4.16}$$

$$C_L = \frac{2L}{\rho \mathbf{V}^2 A_{AC}}. \tag{4.17}$$

The aerodynamic moment coefficients, roll, pitch and yaw, may be calculated in a similar fashion and are given as follows (Crassisis and Junkins 2004):

$$C_l = \frac{2M_x}{\rho \mathbf{V}^2 A_{AC} \cdot b}, \tag{4.18}$$

$$C_m = \frac{2M_y}{\rho \mathbf{V}^2 A_{AC} \cdot c}, \tag{4.19}$$

$$C_n = \frac{2M_z}{\rho \mathbf{V}^2 A_{AC} \cdot b}. \tag{4.20}$$

In the previous six equations $A_{AC} = 0.016\,\mathrm{m}^2$ (total wing surface area), $b = 0.18\,\mathrm{m}$ (wingspan) and $c = 0.066\,\mathrm{m}$ (chord length).

4.5 Summary of MAV aerodynamics

This chapter described the method for extracting aerodynamic forces, moments and angles from the flight data, which are needed for calculating the aerodynamic coefficients. All the coefficients are calculated from and correspond to an individual data point within each trajectory. In order to obtain an understanding of how these vary during the flight they must be plotted against other coefficients or as a function of time. Analyzing the nature of the change in these coefficients along each trajectory is the main focus of Chapter 5.

Chapter 5

Determination of linear stability derivatives

The work presented in this chapter corresponds to the blue section of the MAV experiment flow diagram in Chapter 1. A detailed description of the procedure for extracting linear stability derivatives from the filtered flight trajectories is given. An extended analysis is performed on portions of the flight trajectories that appear to exhibit non-linear aerodynamic properties. It is important to emphasize and study these regions as they provide further insight into the aircraft aerodynamics that may help with the refinement of future experimental and analytical techniques.

5.1 Origin of stability derivatives

During the flight a number of parameters (e.g altitude, airspeed, angle of attack etc.) are continuously varying or oscillating as a result of the changing aerodynamic moments and forces on the aircraft. In order to understand and analyze these changes, and hence the overall aircraft stability, the equations of motion pertaining to the general behavior of the aircraft must be studied. These equations can be rather complex and may be simplified (linearized) using stability and/or control derivatives. Stability derivatives are a measure of how certain aerodynamic forces and moments vary with respect to the change in flight parameters such as those mentioned at the beginning of this section (airspeed etc.). Making this simplification allows the state of the aircraft's stability to be more easily interpreted (Roskam 1986).

A collection of stability derivatives as they vary throughout the flight envelop is known as an aerodynamic model. The use of aerodynamic models in engineering is extremely important for continued advancements in the field. Examples of where they are employed are in flight simulators, for the purpose of stability analysis, and in real-time flight simulators, both for training and entertainment (Sequeira et al. 2006).

5.2 Aerodynamic coefficient equations

In the previous chapter, Equations 4.15 through 4.20 were given for the calculation of six aerodynamic coefficients (C_D, C_Y, C_L, C_l, C_m, C_n). These equations were derived using the forces and moments acting on the aircraft, and the particular aircraft specifications (i.e. wingspan, chord length and total wing surface area). These same aerodynamic coefficients may also be calculated in another way with six different equations. Instead of using the forces, moments and wingspan etc. to determine these coefficients, they may be calculated as the summation of several related stability derivatives (Crassisis and Junkins 2004). This is revealed in Equations 5.1 through 5.6.

$$C_D = C_{D0} + C_{D\alpha}\alpha + C_{D\delta_E}\delta_E. \tag{5.1}$$

C_D is the total drag coefficient, C_{D0} is the drag coefficient at zero angle of attack and zero elevator input ($\alpha = \delta_E = 0$), $C_{D\alpha}$ is the drag coefficient due to angle of attack (α), and $C_{D\delta_E}$ is the drag coefficient due to the elevator input (δ_E).

$$C_Y = C_{Y0} + C_{Y\beta}\beta + C_{Y\delta_R}\delta_R + C_{Y\delta_A}\delta_A. \tag{5.2}$$

C_Y is the total side-force coefficient, C_{Y0} is the side-force coefficient at zero side-slip angle and zero rudder input ($\beta = \delta_R = 0$), $C_{Y\beta}$ is the side-force coefficient due to side-slip angle (β), $C_{Y\delta_R}$ is the side-force coefficient due to the rudder input (δ_R), and $C_{Y\delta_A}$ is the side-force coefficient due to the aileron input (δ_A).

$$C_L = C_{L0} + C_{L\alpha}\alpha + C_{L\delta_E}\delta_E. \tag{5.3}$$

C_L is the total lift coefficient, C_{L0} is the lift coefficient at zero angle of attack and zero elevator input ($\alpha = \delta_E = 0$), $C_{L\alpha}$ is the lift coefficient due to angle of attack (α), and $C_{L\delta_E}$ is the lift coefficient due to the elevator input (δ_E).

$$C_l = C_{l0} + C_{l\beta}\beta + C_{l\delta_R}\delta_R + C_{l\delta_A}\delta_A + C_{lp}\frac{ub}{2||\mathbf{V}||^2} + C_{lr}\frac{wb}{2||\mathbf{V}||^2}. \tag{5.4}$$

C_l is the roll moment coefficient, C_{l0} is the roll moment coefficient at zero angle of attack and zero rudder and aileron input ($\alpha = \delta_R = \delta_A = 0$), $C_{l\beta}$ is the roll moment coefficient due to side-slip angle (β), $C_{l\delta_R}$ is the roll moment coefficient due to rudder input (δ_R), $C_{l\delta_A}$ is the roll moment coefficient due to aileron input (δ_A), C_{lp} is the roll moment coefficient due to roll rate ($p = \frac{ub}{2||\mathbf{V}||^2}$), and C_{lr} is the roll moment coefficient due to yaw rate ($r = \frac{wb}{2||\mathbf{V}||^2}$).

$$C_m = C_{m0} + C_{m\alpha}\alpha + C_{m\delta_E}\delta_E + C_{mq}\frac{vc}{2||\mathbf{V}||^2}. \tag{5.5}$$

C_m is the pitch moment coefficient, C_{m0} is the pitch moment coefficient at zero angle of attack and zero elevator input ($\alpha = \delta_E = 0$), $C_{m\alpha}$ is the pitch moment coefficient due to angle of attack (α), $C_{m\delta_E}$ is the pitch momemt coefficient due to elevator input (δ_E), and C_{mq} is the pitch moment coefficient due to pitch rate ($q = \frac{vb}{2||\mathbf{V}||^2}$).

$$C_n = C_{n0} + C_{n\beta}\beta + C_{n\delta_R}\delta_R + C_{n\delta_A}\delta_A + C_{np}\frac{ub}{2||\mathbf{V}||^2} + C_{nr}\frac{wb}{2||\mathbf{V}||^2}. \tag{5.6}$$

C_n is the yaw moment coefficient, C_{n0} is the yaw moment coefficient at zero angle of attack and zero rudder and aileron input ($\alpha = \delta_R = \delta_A = 0$), $C_{n\beta}$ is the yaw moment coefficient due to side-slip angle (β), $C_{n\delta R}$ is the yaw moment coefficient due to rudder input (δ_R), $C_{n\delta_A}$ is the yaw moment coefficient due to aileron input (δ_A), C_{np} is the yaw moment coefficient due to yaw rate ($p = \frac{ub}{2||\mathbf{V}||^2}$), and C_{nr} is the yaw moment coefficient due to yaw rate ($r = \frac{wb}{2||\mathbf{V}||^2}$).

The six equations in Chapter 4 (Equations 4.15 - 4.20), utilized the aerodynamic forces, moments and particular aircraft specifications in order for the aerodynamic coefficients to be calculated. Plotting these coefficients against some selected variables from Equations 5.1 through 5.6, allows their corresponding stability derivatives to be determined. For example, take Equation 5.1 and assume that there is no elevator input ($\delta_E = 0$, which is the case for this MAV data). Thus Equation 5.1 is reduced to the form $y = mx + b$.

$$C_D = C_{D0} + C_{D\alpha}\alpha. \tag{5.7}$$

Creating a plot of C_D vs α will allow $C_{D\alpha}$, the gradient, and C_{D0}, the y - intercept, to be determined from the plot. Both $C_{D\alpha}$ and C_{D0} are stability derivatives as they provide information about the variations in C_D (hence aerodynamic forces and moments) with respect to an aerodynamic parameter (i.e. α).

5.3 Calculation of stability derivatives

In order to generate basic linear stability derivatives for a baseline simulation, a series of flights were conducted which included climbs, dives, rolls and turns. All flight maneuvers were executed by imparting various initial conditions on the butterfly glider. The following series of plots, Figures 5.1 through 5.11, show the compiled results of 28 trajectories. Rhinehart and Mettler (2008) showed that different coefficients dominate to a greater or lesser extent during different flight maneuvers. Thus using matlab, all the flights were manually split up into predominantly lateral-directional motion (green) and predominantly

vertical-longitudinal motion (blue). Each dot in the plots represents a discrete time instant. The black and red lines overlaid are the linear regression fit to the predominantly lateral-directional and predominantly vertical-longitudinal data respectively. The gradient and y intercept of this line each correspond to a specific stability derivative. Table 5.1 presents a summary of the resulting stability derivatives for the lateral-directional and vertical-longitudinal cases respectively. Since these values are all initial estimates, to be used and refined with the MLE simulation algorithm, no uncertainties have been calculated as the MLE algorithm developed and used for this analysis does not require them.

Table 5.1: Butterfly linear stability derivatives.

Coefficient	Lateral-directional	Vertical-longitudinal
C_{D0}	0.3360	-0.6080
$C_{D\alpha}$	0.0849	0.1423
C_{Y0}	-0.5611	-0.4882
$C_{Y\beta}$	-0.0743	-0.0773
C_{L0}	1.9099	1.9169
$C_{L\alpha}$	0.2915	0.3870
C_{l0}	0.0014	-0.0352
$C_{l\beta}$	-0.0069	-0.0121
C_{lp}	-0.1734	-0.1744
C_{lr}	-0.4415	0.9665
C_{m0}	-0.0032	-0.0326
$C_{m\alpha}$	0.0001	0.0107
C_{mq}	-0.0870	-0.8934
C_{n0}	-0.0088	0.0226
$C_{n\beta}$	-0.0054	0.0066
C_{np}	0.0955	-0.1864
C_{nr}	-0.5802	-0.4044

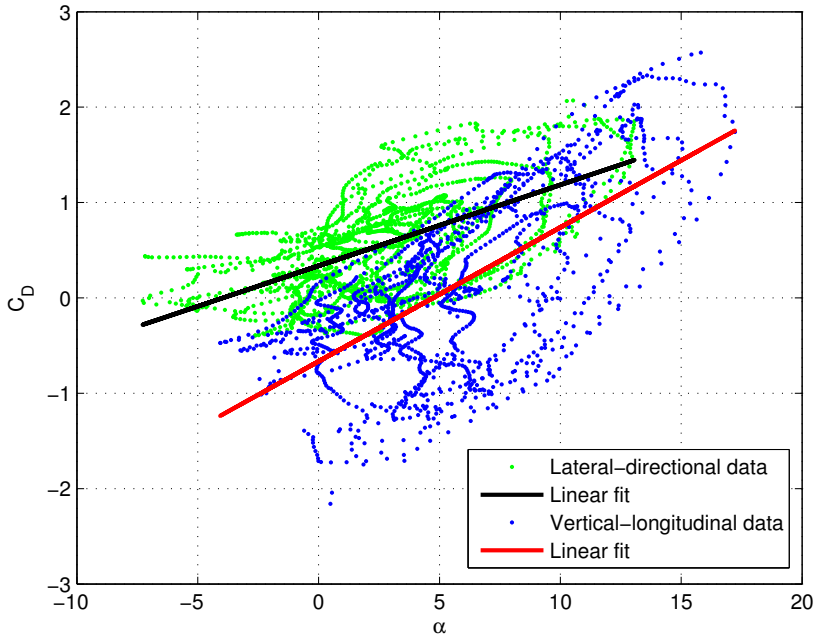

Figure 5.1: Drag force coefficient due to angle of attack.

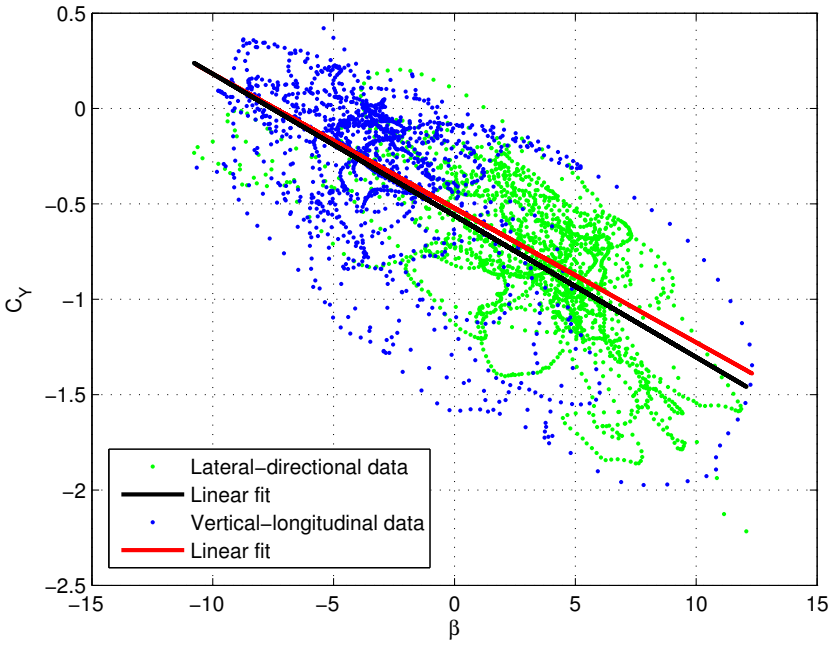

Figure 5.2: Side force coefficient due to side-slip angle.

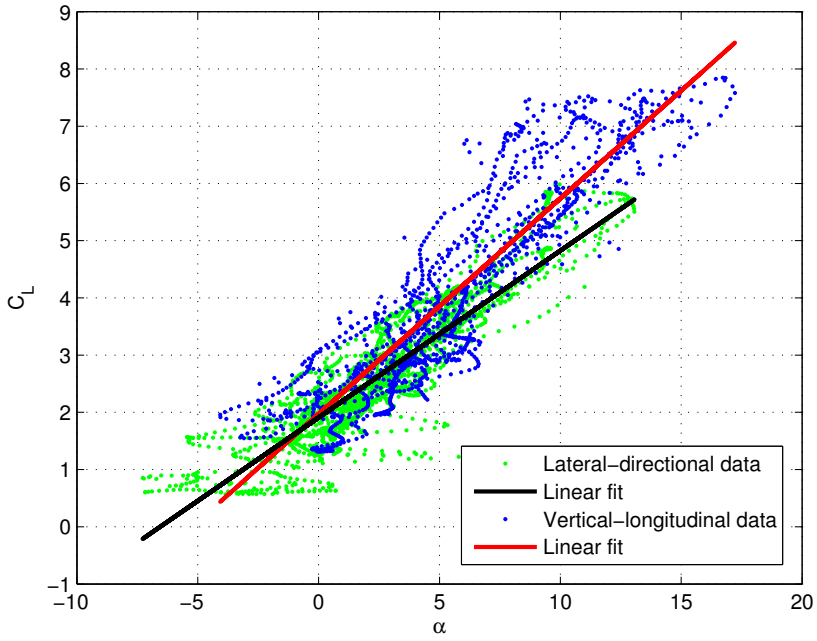

Figure 5.3: Lift force coefficient due to angle of attack.

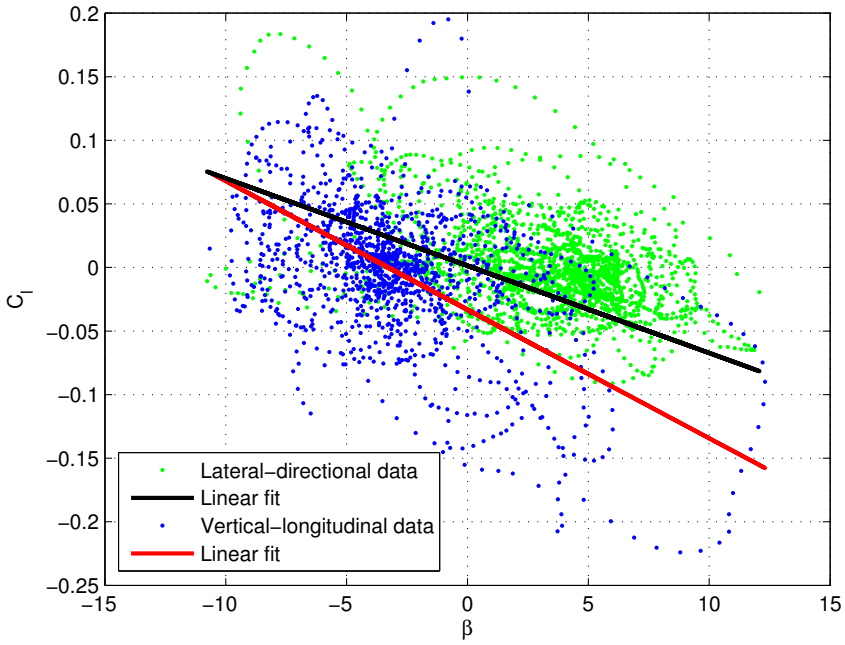

Figure 5.4: Rolling moment coefficient due to side-slip angle.

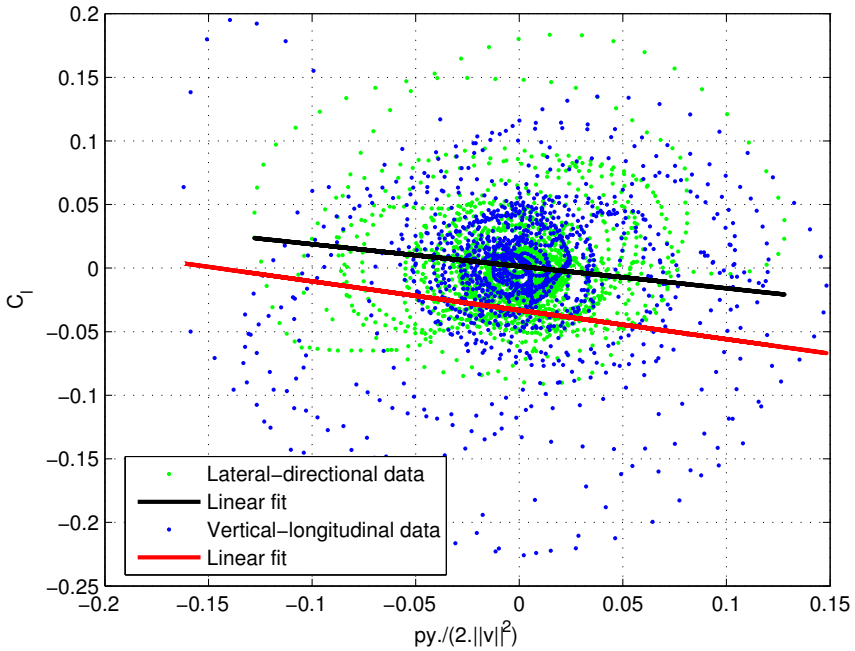

Figure 5.5: Rolling moment coefficient due to roll rate.

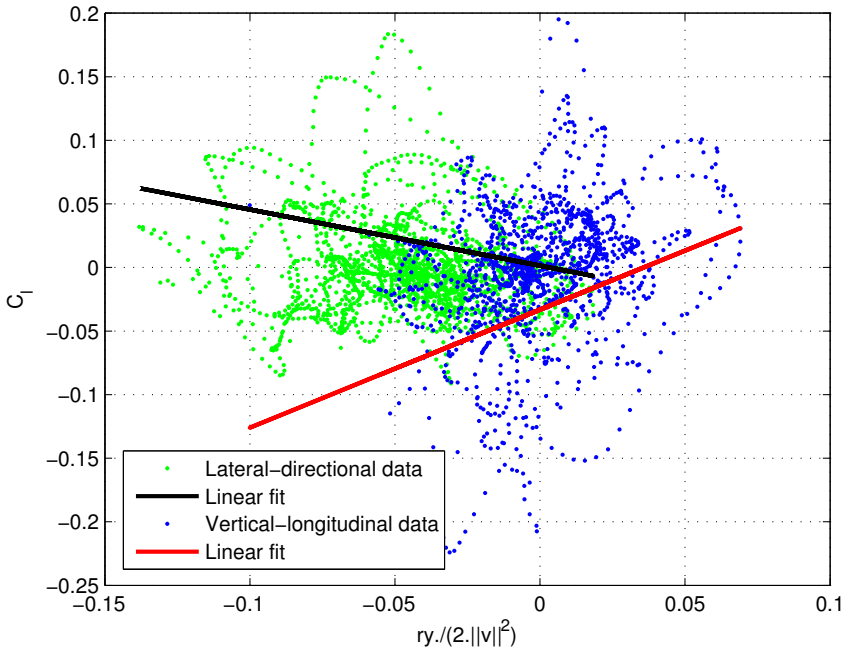

Figure 5.6: Rolling moment coefficient due to yaw rate.

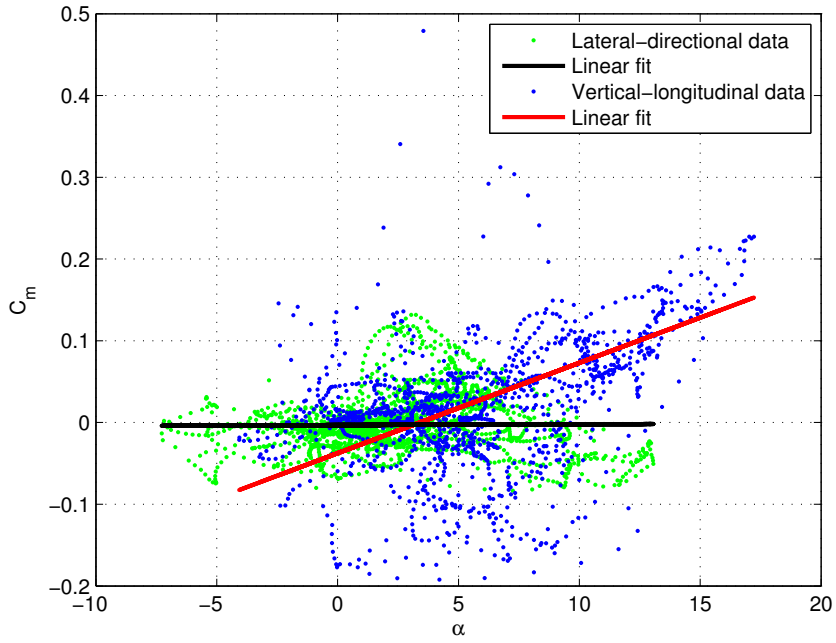

Figure 5.7: Pitch moment coefficient due to angle of attack.

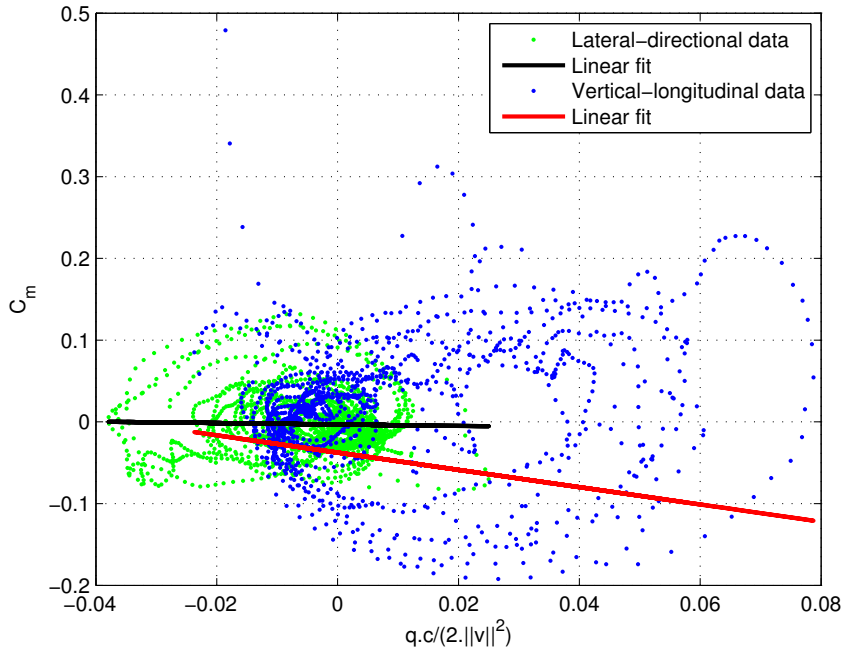

Figure 5.8: Pitch moment coefficient due to pitch rate.

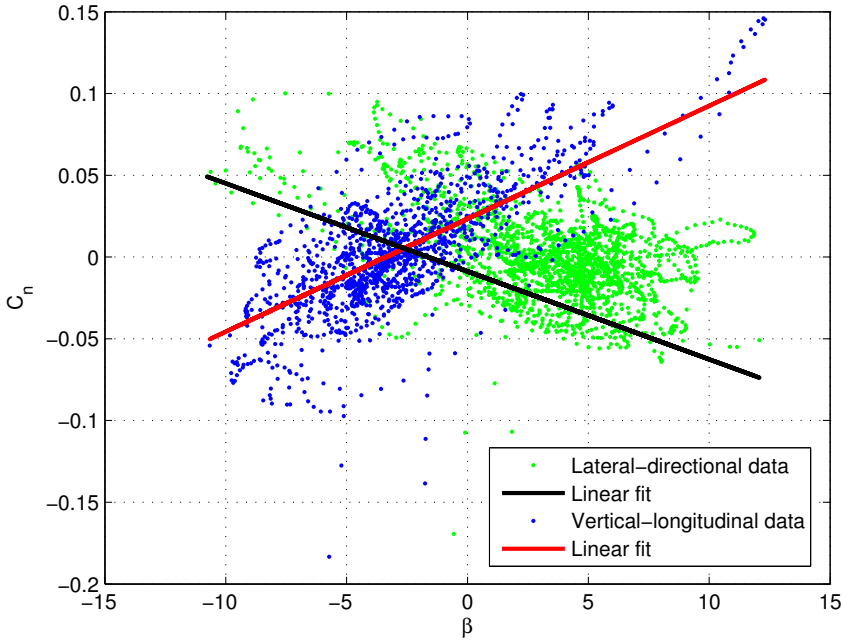

Figure 5.9: Yaw moment coefficient due to side-slip angle.

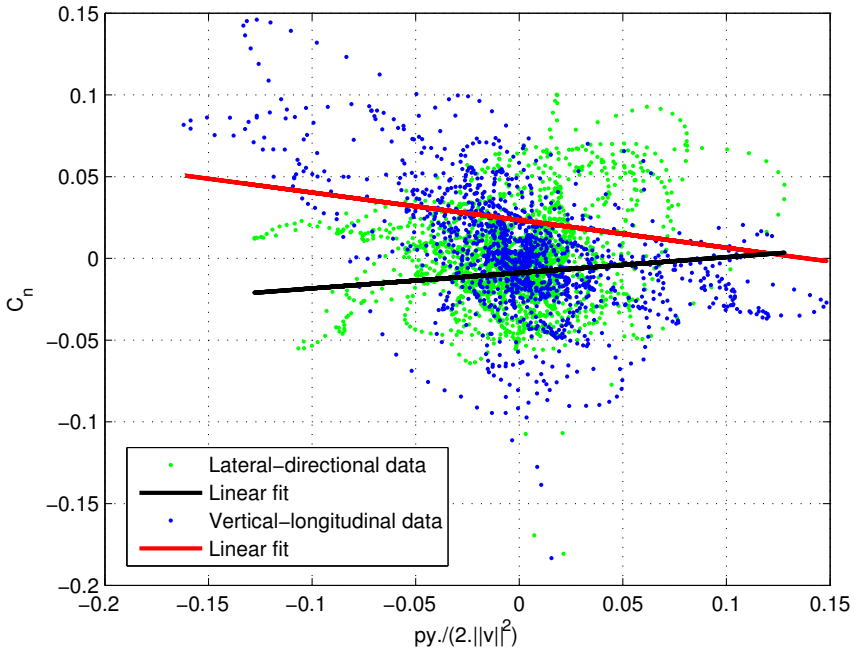

Figure 5.10: Yaw moment coefficient due to roll rate.

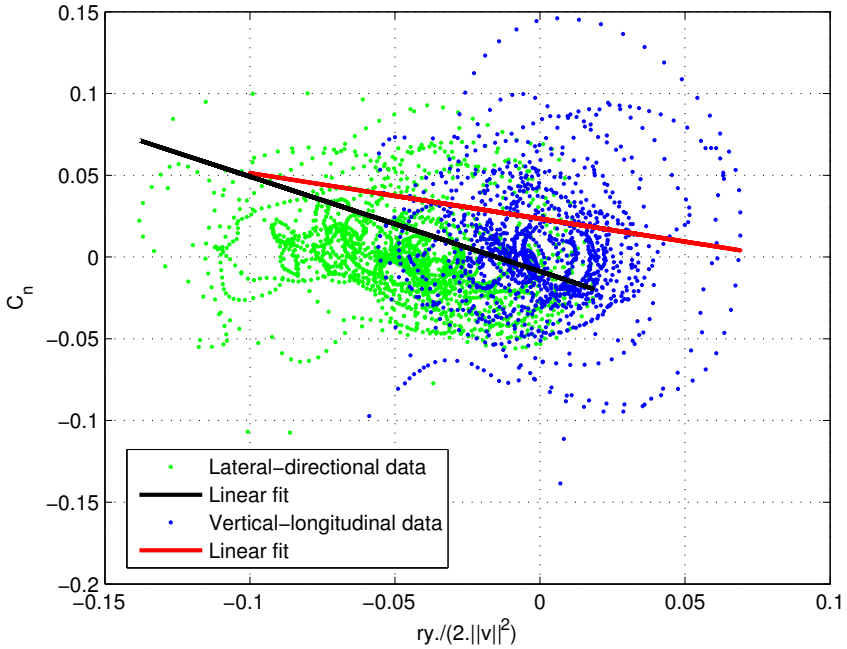

Figure 5.11: Yaw moment coefficient due to yaw rate.

The lateral-directional and vertical-longitudinal data displayed in Figures 5.1, 5.2 and 5.3 are in good agreement, with both data sets revealing strong trends. For aircraft stability C_{D0}, $C_{D\alpha}$, C_{L0} and $C_{L\alpha}$ should all have positive values. Figure 5.3 shows that this is the case for the stability derivatives relating to C_L but from Figure 5.1 it is clear that the linear regression produced by the vertical-longitudinal data does not result in a positive value for C_{D0}. For flight stability in the lateral regime, C_{Y0} and $C_{Y\beta}$ must have values of zero and a negative number respectively. This is true for $C_{Y\beta}$ but not for C_{Y0}. A value of zero for C_{Y0} indicates that there is no side force acting on the aircraft. The data in Figure 5.2 implies the presence of a side force for both the lateral-directional and vertical-longitudinal data - possibly suggesting a hint of instability.

Figures 5.4, 5.5 and 5.6 display the stability derivatives related to C_l - the roll moment coefficient. For stability C_{l0} should have a value of zero with $C_{l\beta}$ being negative. $C_{l\beta}$ is the aerodynamic coefficient related to static roll and comes into play as a result of the dihedral effect from the wings. The linear regression fits for C_{l0} and $C_{l\beta}$ (Figure 5.4) appear to satisfy the requirements for stability.

Figure 5.5 reveals a slightly negative trend line for C_{lp} - the coefficient responsible for roll damping. For stability a negative value for C_{lp} is desired, however it is clear that the data in Figure 5.5 lack a strong trend. Thus the fitted trend line may not give an entirely accurate representation of the true value of the stability derivative. The circular/bunched nature of the data in Figure 5.5 may also demonstrate the presence of a limit cycle. More details relating to this phenomenon are covered in the next section.

The linear regression for C_{lr} displays two distinctly disagreeing trends. For stability C_{lr} must be positive, it's contribution arising mainly from the vertical tail. The vertical-longitudinal data reveal a positive gradient whereas the lateral-directional data show an opposing negative trend. Such a large disagreement is uncanny and could imply some instability in the lateral-directional flight data.

The stability derivatives relating to C_m are given in Figures 5.7 and 5.8. For stability the value of C_{m0} should be positive as it is required to trim the plane at a positive angle of attack. This is not evident in the trend line associated with the lateral-directional nor the vertical-longitudinal data. $C_{m\alpha}$ is important for pitch stability and must take on a negative value. Again, this is not apparent in either of the trend lines in Figure 5.7.

C_{mq} is the aerodynamic coefficient responsible for pitch damping and should maintain a negative value. Figure 5.8 shows a negative linear regression line for the longitudinal-vertical data and a horizontal trend line for the lateral-directional data. Similar to Figure 5.5, a cyclic characteristic is present in the data displayed in Figure 5.8 - suggesting more evidence for the existence of limit cycles within this flight data.

Figures 5.9, 5.10 and 5.11 display the stability derivatives relating to the coefficient of yaw moment (C_n). Aircraft flight stability requires that C_{n0} be zero and $C_{n\beta}$ be positive. Referring to Figure 5.9 is is clear that the values of C_{n0} for the respective data sets fall close to zero, however there is a marked difference in the gradients of the fitted trend lines. The longitudinal-vertical data displays a positive trend, indicating stability, but the lateral-directional data reveals a strong negative trend.

The stability derivatives C_{np} and C_{nr} should both take on negative values for aircraft stability, and Figures 5.10 and 5.11 show that this is the case. However, an interesting point to note is yet again the occurrence of a cyclic trend in the data (Figure 5.11).

5.3.1 Oscillations

Three of the figures mentioned in the previous section (Figures 5.5, 5.8 and 5.11) demonstrate strong cyclic trends which may be indicative of the presence of a limit-cycle[1]. A stable limit-cycle suggests the occurrence self-sustained oscillations (Strogatz 1994). As a result, any small perturbation from the trajectory would cause a stable system to return to the limit-cycle. A reason for self-sustained oscillations in aircraft flight data (Figures 5.5 and 5.11) may be a result of the Dutch roll phenomenon. Dutch roll is the combined effect of oscillations in yaw and roll, where the yaw motion leads roll by one quarter of a cycle. The overall effect

[1]A limit-cycle is a closed trajectory in phase space possessing the property that at least one other trajectory spirals into it as time approaches either positive or negative infinity (Strogatz). Such a phenomenon is characteristic of some non-linear dynamical systems. In the case of a stable or attractive limit-cycle, as time approaches infinity ($+\infty$) all the local trajectories approach the limit-cycle. On the other hand, if all the local trajectories approach the limit-cycle as time tends to negative infinity ($-\infty$) it is known as an unstable or non-attractive limit cycle.

results in the wing tips tracing out an elliptical path with respect to the aircraft fuselage. The short duration (few seconds) of the butterfly flights made observing this phenomenon by eye during the data collection process impossible. However, small variations in the angular position (see Figure 5.12) may provide some evidence to support the occurrence of Dutch roll.

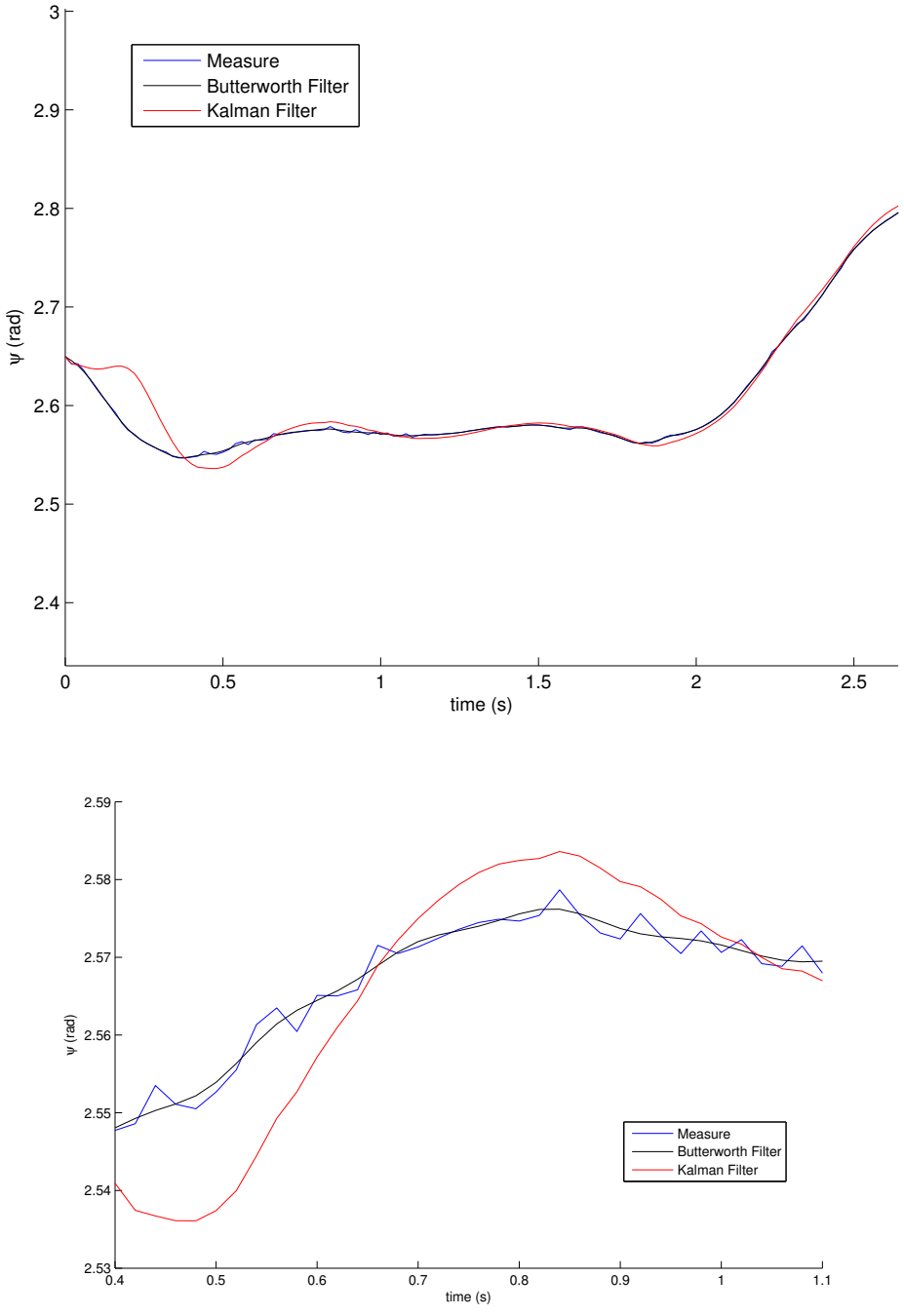

Figure 5.12: The top figure is the angular position (ψ - yaw) which reveals small oscillations that might indicate the presence of the Dutch roll phenonenon (butterflyJul13_04 flight data). The measured data is plotted in blue and the black and red data are filtered with the Butterworth and Kalman filters respectively. The bottom figure is an enlargement of a portion of the top figure.

The Dutch Roll phenomenon dominates the lateral-directional flight regime, however cyclic trends are also apparent in Figure 5.8 which represents dynamic behavior purely in the vertical-longitudinal domain. An effect associated with oscillations in vertical-longitudinal flight dynamics is the phugoid mode (Walter 1967). This is a longer period mode in which large amplitude variations in air-speed, altitude and pitch angle occur. The phugoid mode is a process whereby a slow interchange of kinetic energy (velocity) and potential energy (height) occur about a certain equilibrium energy level. The oscillatory nature depicted in Figure 5.8 may be the result of phugoid mode oscillation, but as with the Dutch Roll, the short duration of the MAV flights prevented these phenomena from being detected by eye during the data collection process.

The discussion on the nature of the stability derivatives presented in this section is important as it allows the aircraft stability to be assessed. Several of the stability derivatives appear to suggest some form of instability present in the flights. The conclusions regarding the stability of the various stability derivatives are drawn based on material published in books by the following authors: Cook 2007; Shevell 1989; Stribling 1984; Babister 1961; Duncan 1959. Further details relating to mathematical phenomena and physical effects associated with aerodynamic stability derivatives may be found by referring to these sources.

5.4 Non-linearities

The stability derivatives discussed in the previous section were derived using a linear aerodynamic model and it is clear that some regions of the data plotted in Figures 5.1 through 5.11 do not conform well to the linear trend lines. To investigate this further the difference between each data point and the corresponding position on the trend line was calculated and normalized. These normalized difference values were used to create a color map and the data were re-plotted to reveal the regions of the trajectory that exhibit strong linear aerodynamic characteristics and regions that reveal less of a linear trend. The plots of C_D, C_Y and C_L display the most prominent trends and figures corresponding to these stability derivatives are presented.

5.4.1 Non-linearities in C_D - lateral-directional data

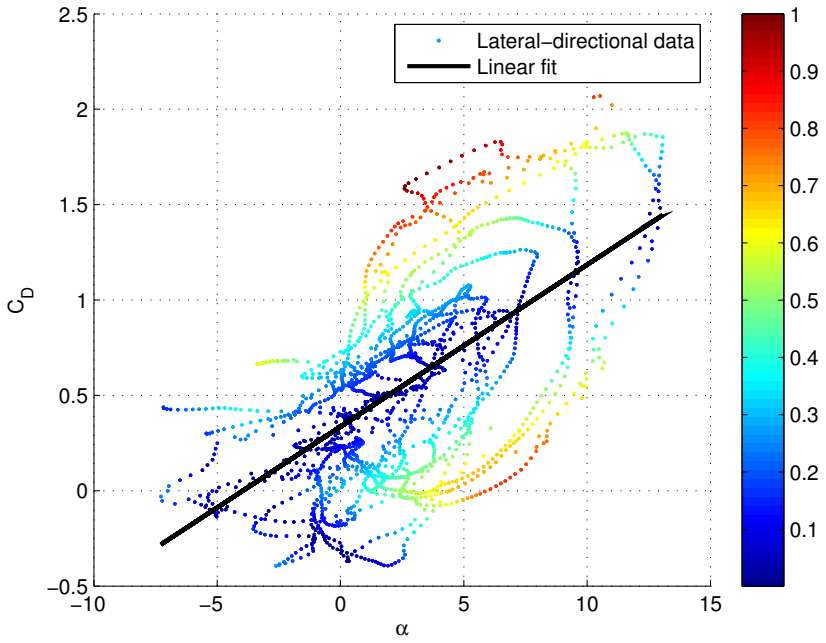

Figure 5.13: Drag force coefficient due to angle of attack (lateral-directional data). The data is color-coded to reveal portions of the trajectory that are in good agreement with the linear aerodynamic model (blue) and those that are not (red).

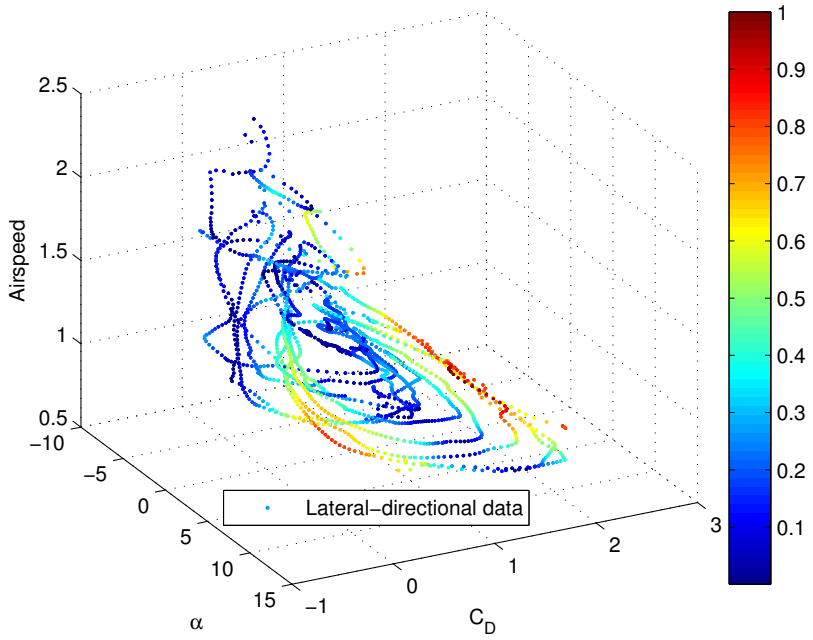

Figure 5.14: The data in Figure 5.13 plotted as a function of airspeed. The data is color-coded to reveal portions of the trajectory that are in good agreement with the linear aerodynamic model (blue) and those that are not (red).

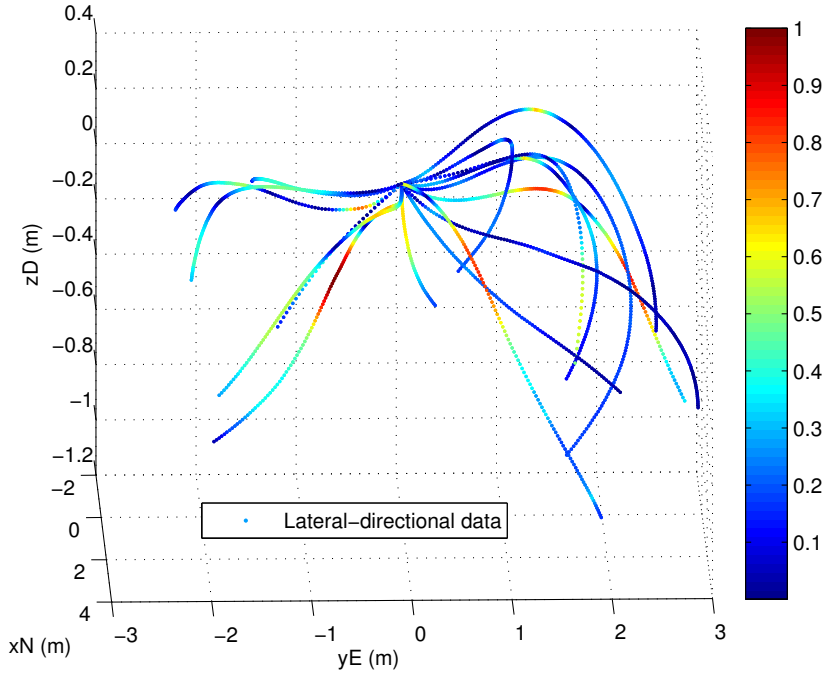

Figure 5.15: Lateral-directional trajectory data color-coded with the same color map used in Figures 5.13 and 5.14. It reveals regions of the trajectory that are in good agreement with the linear aerodynamic model (blue) and those that are not (red).

In Figure 5.13 it appears that most of the trajectories follow a similar path for which the majority of the flight data points exhibit linear aerodynamic properties (shades of blue). Only five trajectories reveal regions of "extreme" non-linearity (shades of orange/red). These regions occur in the vicinity of $\alpha = 5^\circ$ and correspond to both high and low values of C_D - possibly suggesting their independence from C_D. Figure 5.14 displays this data plotted with an additional dimension - angle of attack. As expected, the airspeed declines as angle of attack increases. Most of the trajectories seem to follow a loop starting with high initial airspeed that drops off as C_D increases and then increases again as C_D decreases due to the change in angle of attack.

Figure 5.15 shows the 3-dimensional trajectories with the same color map as that generated for Figures 5.13 and 5.14. The five non-linear regions are color-coded in red as before. Three of these are located at an extreme vertical gradient. The other two occur at places where the trajectory appears to plateau shortly before it dives. These plateau and extreme vertical regions indicate the aircraft transitioning through a stall. Although these flights are characterized as predominantly lateral-directional motion, they still possess a significant vertical component (due to gravity) and thus may undergo a simultaneous turning-stall.

During a stall the airflow shifts from laminar to turbulent, thus leading to a breakdown of linear aerodynamic properties. Although intriguing, a further investigation of these anomalies will be left as future work because their presence in Figure 5.13 does not effect the overall value of the related stability derivatives.

5.4.2 Non-linearities in C_Y - lateral-directional data

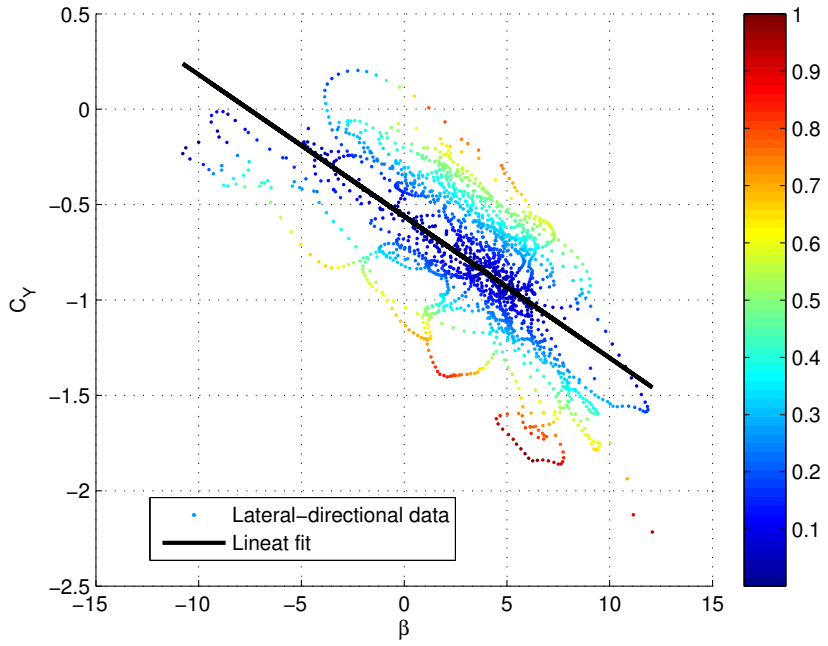

Figure 5.16: Side force coefficient due to side-slip angle (lateral-directional data). The data is color-coded to reveal portions of the trajectory that are in good agreement with the linear aerodynamic model (blue) and those that are not (red).

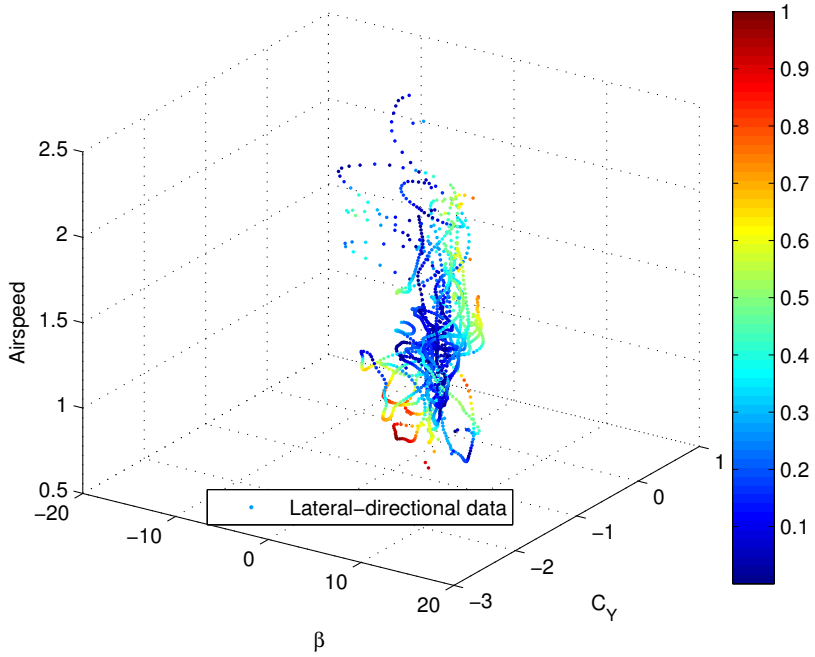

Figure 5.17: The data in Figure 5.16 plotted as a function of airspeed. The data is color-coded to reveal portions of the trajectory that are in good agreement with the linear aerodynamic model (blue) and those that are not (red).

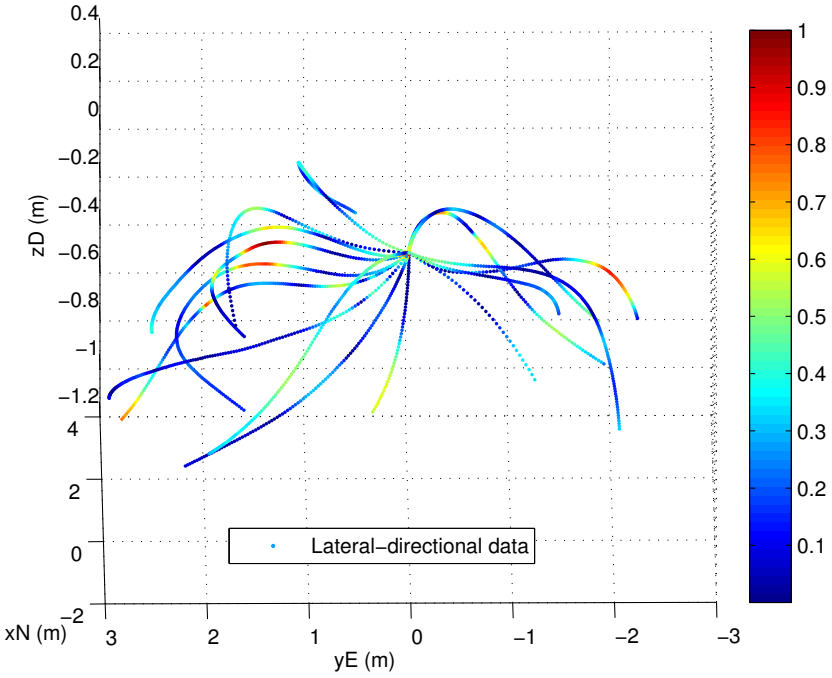

Figure 5.18: Lateral-directional trajectory data color-coded with the same color map used in Figures 5.16 and 5.17. It reveals regions of the trajectory that are in good agreement with the linear aerodynamic model (blue) and those that are not (red).

The side-slip generates a side-slip force due to incident air on the fuselage and fin. This is a restoring force bringing the plane back to equilibrium ($\beta = 0$). Referring to Figure 5.16 it is evident that the data is not centrally situated about $\beta = 0$. This reveals that for the majority of the flights the plane was out of equilibrium or imbalanced. Two possible reasons for this imbalance could be that the plane was not correctly trimmed, or that the majority of the flights involved a "strange" attitude i.e. a banking turn. The first reason is unlikely, and since in all cases the plane was turning the more reasonable conclusion for the central offset is the latter.

Figure 5.17 displays a 3-dimensional plot of C_Y vs β vs airspeed. It is apparent that the maximum airspeed occurs at an angle of $\beta = 0$. This would correspond to the airflow incident directly on the nose which also represents the plane in it's best aerodynamic configuration - thus it is not surprising that the airspeed is a maximum at this point. Similar to the C_D case, the color map used in Figures 5.16 and 5.17 is implemented in Figure 5.18. There are five places (orange/red data) in the trajectories where linear aerodynamics ceases to exist. These all occur where the turn gradient, and hence side-force, is a maximum. As before, a deeper investigation of these enigmatic regions is left for future work because their effect will not cause a significant change in the stability derivatives derived from the fitted trend line.

5.4.3 Non-linearities in C_L - lateral-directional data

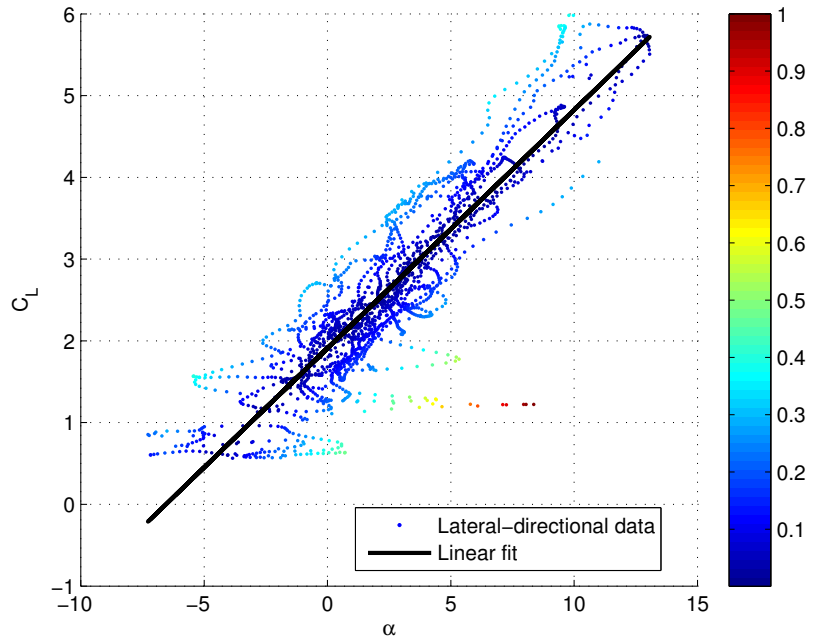

Figure 5.19: Lift force coefficient due to angle of attack (lateral-directional data). The data is color-coded to reveal portions of the trajectory that are in good agreement with the linear aerodynamic model (blue) and those that are not (red).

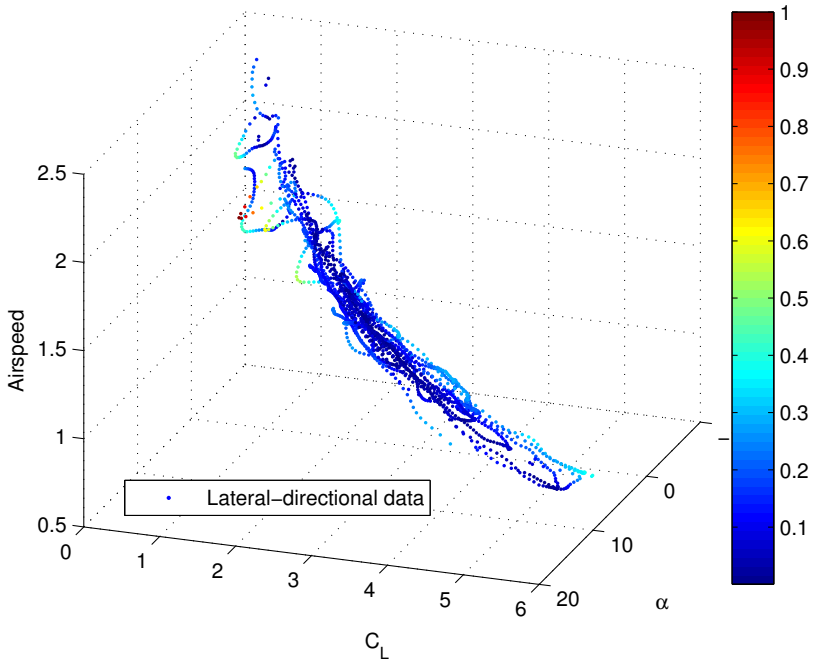

Figure 5.20: The data in Figure 5.19 plotted as a function of airspeed. The data is color-coded to reveal portions of the trajectory that are in good agreement with the linear aerodynamic model (blue) and those that are not (red).

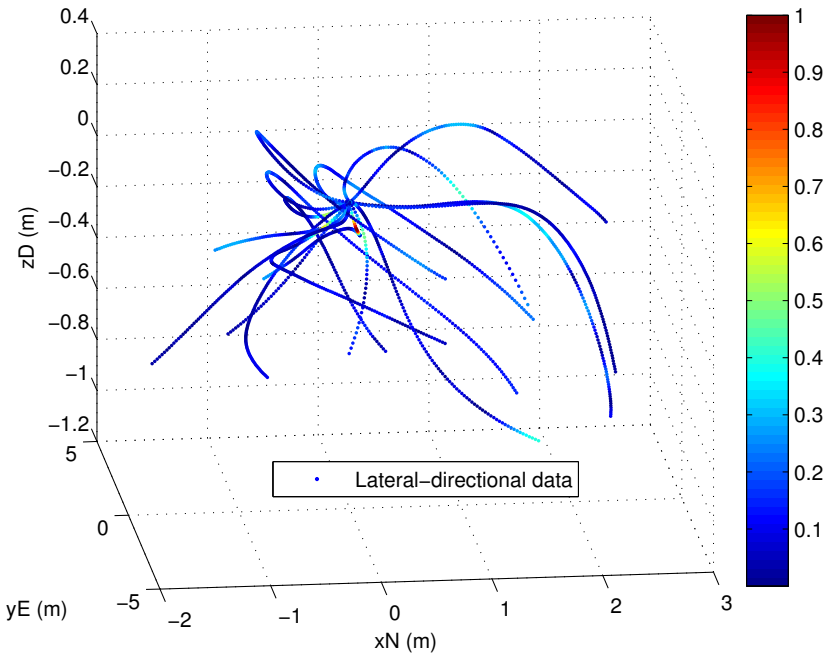

Figure 5.21: Lateral-directional trajectory data color-coded with the same color map used in Figures 5.19 and 5.20. It reveals regions of the trajectory that are in good agreement with the linear aerodynamic model (blue) and those that are not (red).

Figure 5.19 shows a strong positive relationship between C_L and α. Most of the trajectories fall within the dark blue region of the color map indicating good compliance with the linear aerodynamics describing the flight. There is only one particular flight in which a few data points do not conform to the linear aerodynamics (orange/red data). This occurs at a relatively large angle of attack and might be due to the plane undergoing a stall.

In Figure 5.20 the data is plotted in 3-dimensions to include the airspeed. Again very strong relationships are present and it is clear that airspeed falls off as the angle of attack grows - as expected. At high airspeeds it is also apparent that the coefficient of lift is low. Considering that the plane is most likely in a dive attitude during times of high speed, one would expect the coefficient of lift to be low or negative at this point. Finally the color mapped trajectories are displayed in Figure 5.21, as was done for the previous coefficients.

5.4.4 Non-linearities in C_D - vertical-longitudinal data

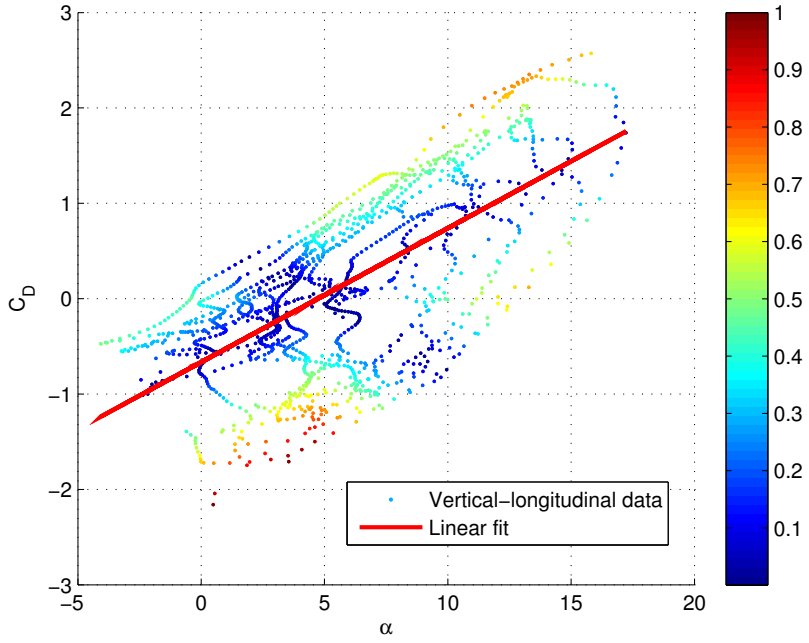

Figure 5.22: Drag force coefficient due to angle of attack (vertical-longitudinal data). The data is color-coded to reveal portions of the trajectory that are in good agreement with the linear aerodynamic model (blue) and those that are not (red).

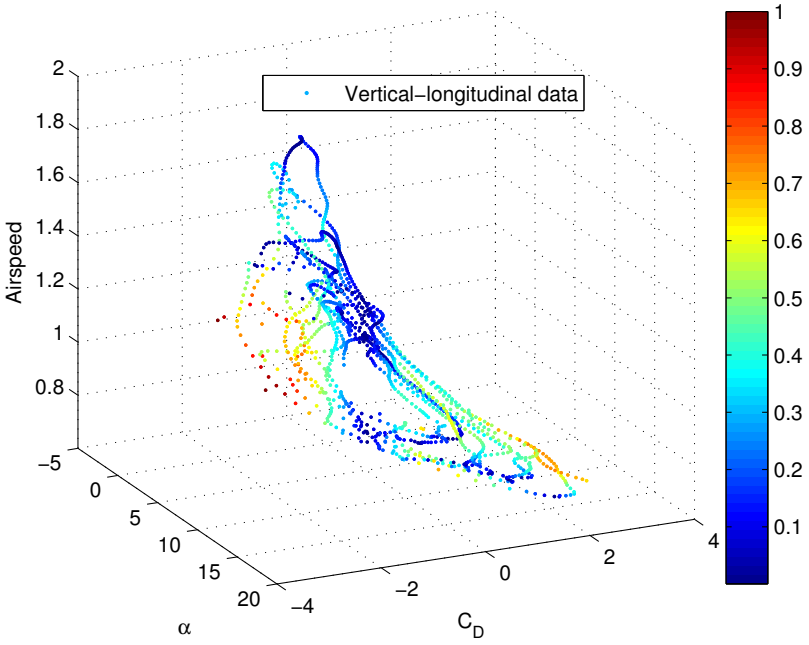

Figure 5.23: The data in Figure 5.22 plotted as a function of airspeed. The data is color-coded to reveal portions of the trajectory that are in good agreement with the linear aerodynamic model (blue) and those that are not (red).

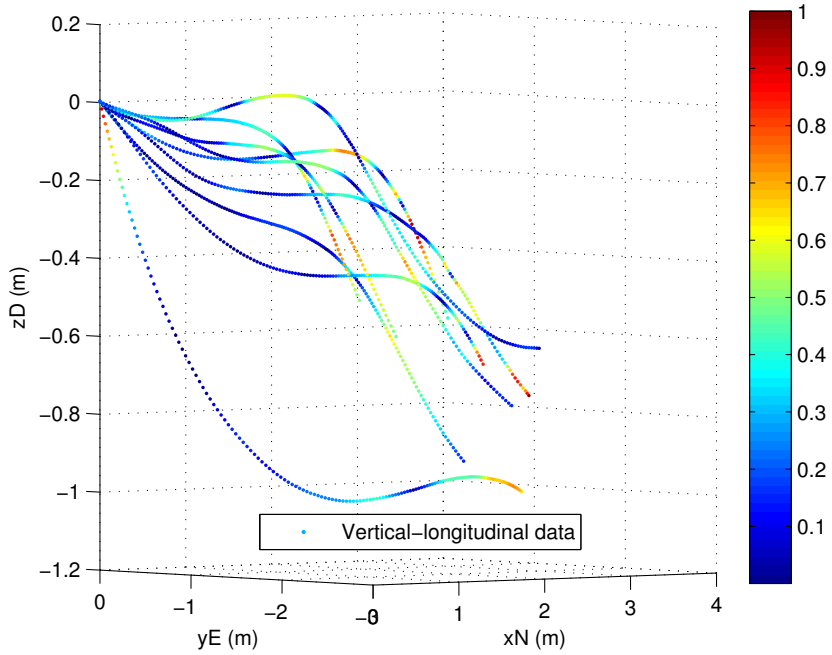

Figure 5.24: Vertical-longitudinal trajectory data color-coded with the same color map used in Figures 5.22 and 5.23. It reveals regions of the trajectory that are in good agreement with the linear aerodynamic model (blue) and those that are not (red).

Figures 5.22 and 5.23 show the trajectories tracing out a loop path, similar to what occurred in the lateral-directional case (Figure 5.13). As expected there is a distinct increase in C_D with rising α. The difference in this plot compared with the lateral-directional case is that a higher fraction of the data falls into the orange/red category. This is confirmed in Figure 5.24 and is most likely a result of more stalls occurring in this vertical-longitudinal data, leading to more instances when the airflow is turbulent and thus use of the linear aerodynamic model becomes inadequate.

5.4.5 Non-linearities in C_Y - vertical-longitudinal data

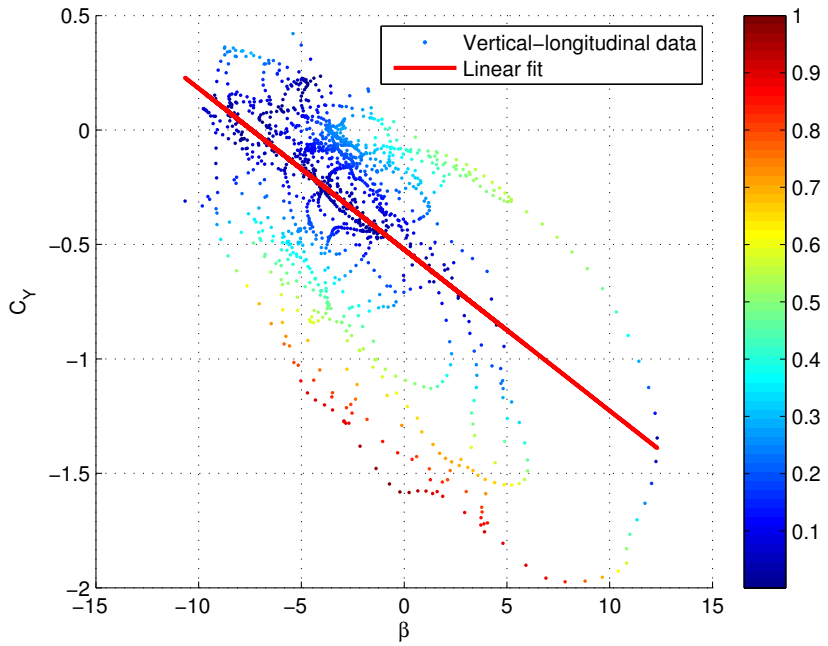

Figure 5.25: Side force coefficient due to side-slip angle (vertical-longitudinal data). The data is color-coded to reveal portions of the trajectory that are in good agreement with the linear aerodynamic model (blue) and those that are not (red).

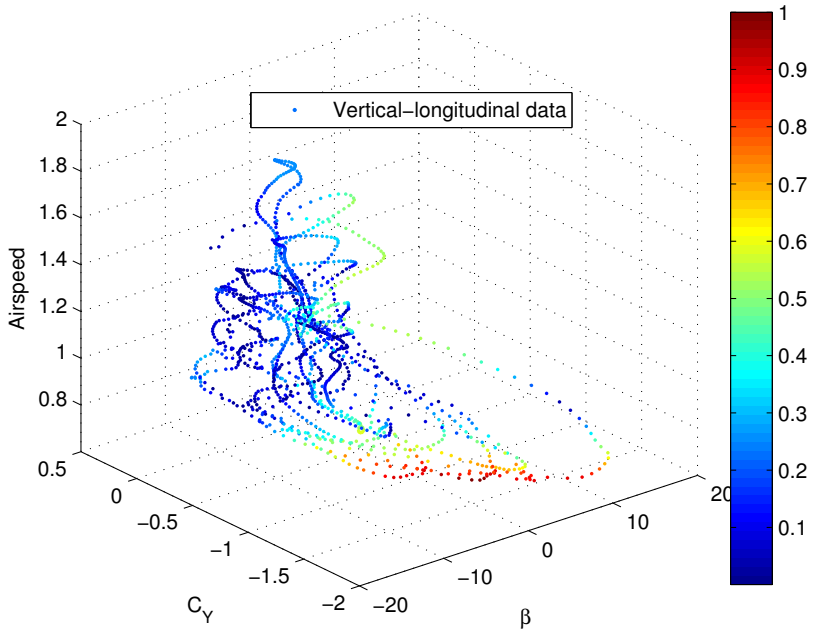

Figure 5.26: The data in Figure 5.25 plotted as a function of airspeed. The data is color-coded to reveal portions of the trajectory that are in good agreement with the linear aerodynamic model (blue) and those that are not (red).

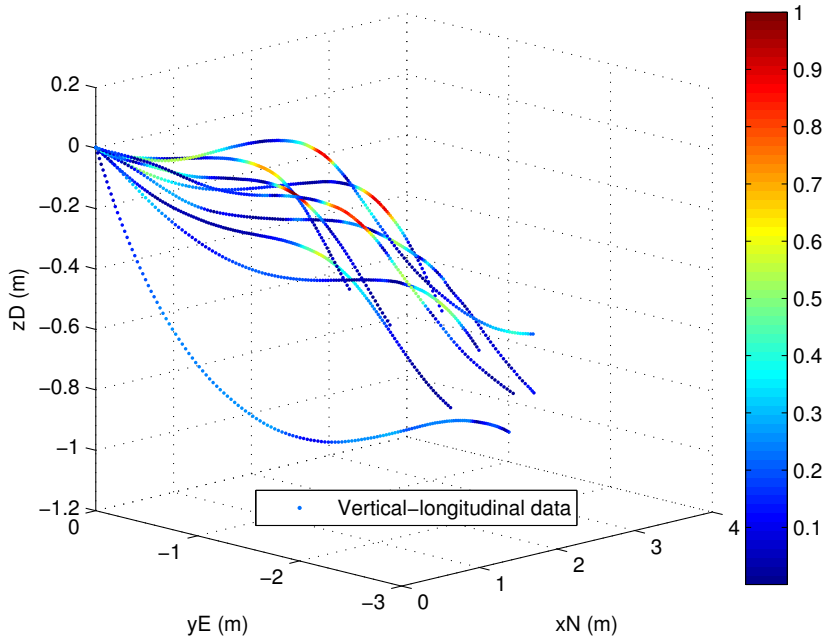

Figure 5.27: Vertical-longitudinal trajectory data color-coded with the same color map used in Figures 5.25 and 5.26. It reveals regions of the trajectory that are in good agreement with the linear aerodynamic model (blue) and those that are not (red).

Figures 5.26 and 5.27 reveal more spread in the data compared with the corresponding lateral-directional data plots in Section 5.4.2. The vertical-longitudinal data also seems to be more centrally distributed than in the lateral-directional case (i.e the data is centered around $\beta = 0$). This may be attributed to the horizontal motion, and hence the magnitude of the side-force, being a minimum during predominantly vertical-longitudinal flights - thus implying that the aircraft spent a greater part of each flight in balance compared with the lateral-directional flights. Again the maximum airspeed occurs near to $\beta = 0$ which is similar to the lateral-directional data and the same explanation may be applied (Section 5.4.2). Figure 5.18 displays the color mapped trajectories revealing areas that stray from the linear aerodynamic conditions (orange/red data). These occur at the point of maximum curvature from the horizontal to vertical direction. As such these regions are indicative of a stall and hence prevent the use of linear aerodynamic models for an accurate description of the entire flight.

5.4.6 Non-linearities in C_L - vertical-longitudinal data

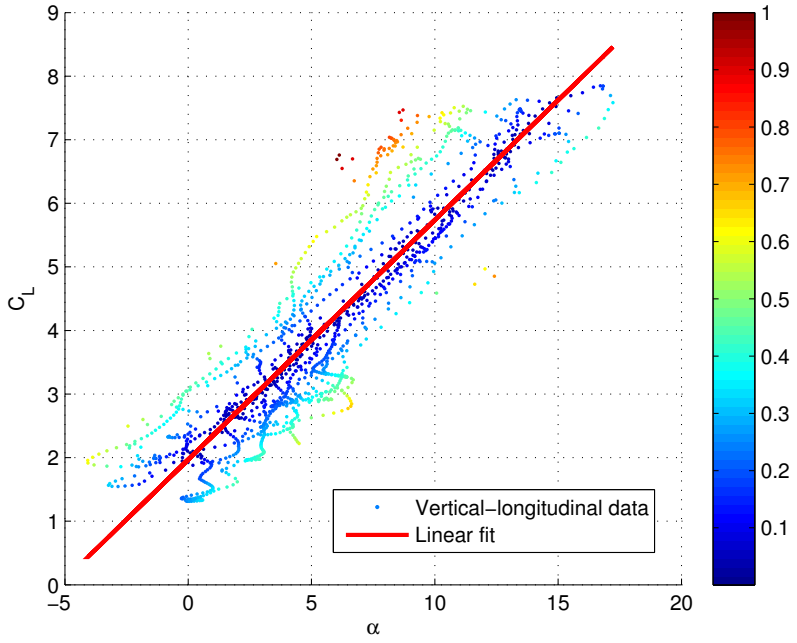

Figure 5.28: Lift force coefficient due to angle of attack (vertical-longitudinal data). The data is color-coded to reveal portions of the trajectory that are in good agreement with the linear aerodynamic model (blue) and those that are not (red).

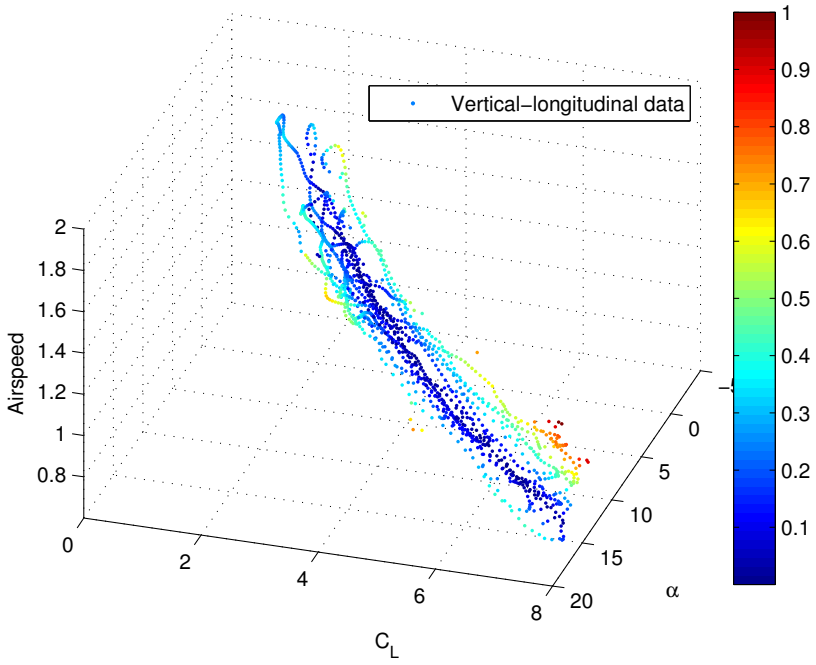

Figure 5.29: The data in Figure 5.28 plotted as a function of airspeed. The data is color-coded to reveal portions of the trajectory that are in good agreement with the linear aerodynamic model (blue) and those that are not (red).

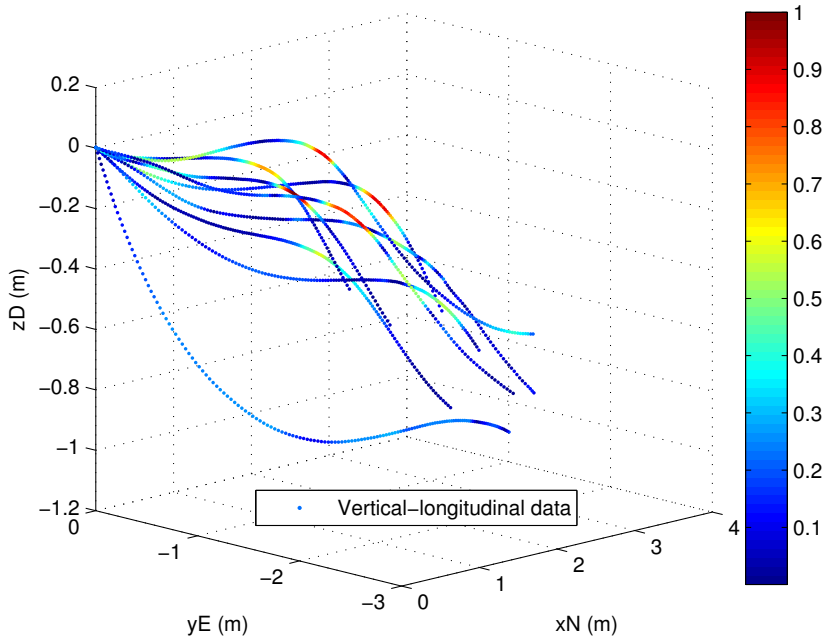

Figure 5.30: Vertical-longitudinal trajectory data color-coded with the same color map used in Figures 5.28 and 5.29. It reveals regions of the trajectory that are in good agreement with the linear aerodynamic model (blue) and those that are not (red).

Both the C_L coefficients for the lateral-directional and vertical-longitudinal cases show the strongest linear trend out of all the other stability derivatives. Figures 5.28 and 5.29 show that the majority of the data takes on a shade of blue, however slightly more data than in the lateral-directional case falls into the non-linear (orange) domain. Again this implies that the linear aerodynamic conditions are disobeyed during a stall. The other trends (i.e. increase in α with an increase in C_L) are the same as those described in Section 5.4.3. Figure 5.30 shows the corresponding color mapped trajectories.

5.5 Summary of stability derivative analysis

This chapter discusses the procedure for generating linear stability derivatives from coefficients extracted from the MAV experimental flight data. In order to produce reliable stability derivatives a sample of trajectories covering a broad range of the flight envelope must be studied (i.e turns, stalls, helical glides etc.). The calculation of stability derivatives in this chapter gives an interesting insight into this relatively unexplored flight regime for MAVs.

During the stability derivative analysis, several regions in the flight trajectories revealed that they could not be well approximated using a linear aerodynamic model. Further investigation lead to the assumption that these regions are the result of the aircraft transitioning through a stall - thus leading to turbulent airflow and a breakdown in the credibility of the equations used to describe the aerodynamics at these particular locations.

Although the linear aerodynamic model cannot be used to generate reliable coefficients for the entire flight trajectory, it performs reputably for the majority of the data and thus the overall fitted trend lines are not significantly altered with the inclusion of all these flight trajectories. However, regions demonstrating severe non-linearity are avoided during further calculations undertaken for this thesis.

Some of the trend lines indicate an instability in the flights, however these stability derivatives are the best that can currently be achieved with this Butterfly MAV data and thus they are used as initial estimates within the maximum likelihood estimation flight simulation presented in Chapter 6.

Chapter 6

System identification

System identification, using the method of Maximum Likelihood Estimation (MLE), is the final part of this thesis and corresponds to the yellow section in the MAV flow diagram presented in Chapter 1. This chapter presents a detailed description of MLE and it's purpose - identification and validation of the MAV aerodynamic model - designed using experimental data (Chapter 2), aerodynamic coefficients and stability derivatives (Chapters 4 and 5), and published aerodynamic equations (Crassisis and Junkins 2004). All 28 trajectories studied in this thesis were run through the MLE algorithm and the best results are presented and discussed in this chapter.

6.1 System identification and MLE description

The following sections provide some details relating to the theoretical nature of system identification and MLE. A more thorough description may be found by referring to Jategaonkar (2006) and Crassisis and Junkins (2004).

6.1.1 System identification

System identification may be quoted as follows: "Given the answer, what are the questions, i.e., look at the results and try to figure out what situation caused those results." (Hamel and Jategaonkar 1996). In order to do this a mathematical model describing the unknown dynamic system must be determined or "identified". The first step in the process to achieving this is to make an estimate of the initial parameters and then allow them to be quantified using a numerical algorithm. For a flight simulation model this would be an initial estimate of the stability derivatives. Some of the ways to acquire these initial estimates are through wind tunnel techniques, computational fluid dynamics and for the work presented in this thesis, in-flight vision based motion tracking. These initial estimates are then loaded into a simulation model and a validation is performed to check the model fidelity. At this point

if the model does not meet the required specifications, the model structure must be altered and the entire process repeated until the requirements are met. This iterative process forms part of the MLE algorithm presented in the following sections.

System identification and validation (Schlesinger et al. 1974) is vital for the development and enhancement of flight vehicles as it allows their performance to be quantified. This is of particular importance when it comes to MAVs as the models used can increase the design manifold for these automated unpiloted vehicles. Parameter identification undertaken using experimental flight data permits the ultimate verification of simulation models, thus allowing future flight tests to be conducted using the computer simulation rather than experimentally in the laboratory environment.

Various methods for identifying and refining aircraft coefficients and stability derivatives have been studied over the years, from basic detection of frequencies and damping ratios in the 1920s, to the least squares approach in the 1940s and 1950s (Iliff 1989). A paper published by Suit (1972) on the extraction of aerodynamic parameters from flight data for the Navion aircraft employed the method of MLE. Today this is the most widely used technique for aircraft parameter identification (Jategaonkar 2006). The approach and MLE technique described in Suit (1972) is used as a guide for the analysis undertaken in this thesis.

6.1.2 Maximum Likelihood Estimation

MLE was introduced by Fisher in the 1920's with the aim of producing estimates for certain unknown quantities that maximize the probability of obtaining the observed data set. A collection of experimental data can be approximated by a Gaussian distribution and the probability of a data point belonging to that distribution is given by the probability density function (Equation 6.1). In Equation 6.1, $\tilde{y}$ is taken as a random sample from a simple Gaussian distribution, π is the mean and σ^2 is the variance.

$$f(\tilde{y};x) = \left(\frac{1}{2\pi\sigma^2}\right)^{m/2} e^{\left[-\sum_{i=1}^{m}(\tilde{y}_i-\mu)^2/(2\sigma^2)\right]} \tag{6.1}$$

Since this function is monotonic (i.e. it will either always increase or always decrease) taking the natural logarithm of Equation 6.1 will not effect the distribution nor the results, and it allows for easier computational handling. Thus the logarithm of the probability density function is as follows:

$$ln\left[f(\tilde{y};x)\right] = -\frac{m}{2} ln\left(2\pi\sigma^2\right) - \frac{1}{2\sigma^2}\sum_{i=1}^{m}(\tilde{y}_i-\mu)^2. \tag{6.2}$$

Equation 6.2, the probability density function, is also referred to as the likelihood function when implemented in an MLE algorithm. The aim of MLE is to maximize the likelihood

function, i.e. determine the maximum likelihood estimate ($\hat{x}$) for the value of x that maximizes $f(\tilde{y};x)$. Solving for the maximum requires satisfying the following necessary (Equation 6.3) and sufficient (Equation 6.4) conditions.

$$\left\{\frac{\partial}{\partial x} ln\left[L(\tilde{y};x)\right]\right\}\Bigg|_{\hat{x}} = 0 \tag{6.3}$$

$$\frac{\partial^2}{\partial x \partial x^T} ln\left[L(\tilde{y};x)\right] < 0. \tag{6.4}$$

The likelihood function is composed of parameters that describe the distribution. These parameters, the mean (μ) and covariance (σ^2), must be known before a maximization of the likelihood function can performed. For a linear model given by Equation 6.5, assuming v has a zero mean Gaussian distribution (perfect measurements) with a covariance of $cov\{v\} = R = E\left\{vv^T\right\}$, the mean and covariance for the likelihood function may be calculated as shown in Equations 6.6 and 6.7.

$$\overset{(m\times 1)}{\tilde{y}} = \overset{(m\times n)}{H}\overset{(n\times 1)}{x} + \overset{(m\times 1)}{v} \tag{6.5}$$

The mean is given by the expected value of $\tilde{y}$,

$$\mu = E\left\{\tilde{y}\right\} = E\left\{Hx\right\} + E\left\{v\right\}, \tag{6.6}$$

leading to $\mu = Hx$, and the covariance may be calculated as

$$cov\left\{\tilde{y}\right\} = E\left\{(\tilde{y}-\mu)(\tilde{y}-\mu)^T\right\} = R. \tag{6.7}$$

Thus, making the relevant substitutions for the mean and covariance results in the following normal distribution for the likelihood function:

$$L(\tilde{y};x) = \frac{1}{(2\pi)^{m/2}\left[det(R)\right]^{1/2}} exp\left\{-\frac{1}{2}\left[\tilde{y}-Hx\right]^T R^{-1}\left[\tilde{y}-Hx\right]\right\}. \tag{6.8}$$

As previously demonstrated, taking the natural logarithm of this function is a legitimate procedure that leads to

$$ln\left[L(\tilde{y};x)\right] = -\frac{1}{2}\left[\tilde{y}-Hx\right]^T R^{-1}\left[\tilde{y}-Hx\right] - \frac{m}{2} ln(2\pi) - \frac{1}{2} ln\left[det(R)\right]. \tag{6.9}$$

The last two terms on the right hand side of Equation 6.9 are independent of x and they can be ignored. Taking the negative of what remains results in Equation 6.10, which is known as the loss function. Maximizing the likelihood function (Equation 6.9 - x dependent terms

only) is the same as minimizing the loss function (Equation 6.10). Section 6.1.3 discusses a mathematical method for minimizing the loss function.

$$J(\hat{x}) = \frac{1}{2}\left[\tilde{y} - H\hat{x}\right]^T R^{-1}\left[\tilde{y} - H\hat{x}\right]. \tag{6.10}$$

6.1.3 Minimizing the loss function

The previous section outlined a number of mathematical steps leading to the derivation of the loss function. The loss function (J) used in MLE algorithm for this thesis is given by Equation 6.11.

$$J(\hat{\mathbf{p}}) = \frac{1}{2}\sum_{k=1}^{N}(\tilde{\mathbf{y}}_k - \hat{\mathbf{y}}_k)^T R^{-1}(\tilde{\mathbf{y}}_k - \hat{\mathbf{y}}_k). \tag{6.11}$$

In this equation $\tilde{y}_k$ is a point from the experimental trajectory at time k, $\hat{y}_k$ is the corresponding point from the simulated trajectory (see Section 6.2), R is the covariance matrix, $\hat{\mathbf{p}}$ is a value of the unknown parameter (e.g. stability derivative) and N is the total number of measurements.

One technique for minimizing the loss function entails the use of the Newton-Raphson algorithm presented in Equations 6.12 through 6.15. This algorithm is taken from page 214 of Crassisis and Junkins (2004). Here i is the iteration number with the $i + 1$ estimate of $\hat{\mathbf{p}}$ defined as follows:

$$\hat{\mathbf{p}}_{i+1} = \hat{\mathbf{p}}_i - \left[\nabla^2_{\hat{\mathbf{p}}} J(\hat{\mathbf{p}})\right]^{-1}\left[\nabla_{\hat{\mathbf{p}}} J(\hat{\mathbf{p}})\right]. \tag{6.12}$$

The first and second gradients in Equation 6.12 are given by Equations 6.13 and 6.14, where $\nabla_{\hat{p}}$ and $\nabla^2_{\hat{p}}$ represent the Jacobian vector and Hessian matrix respectively. For the Butterfly flight data, the gradient is given by the change in the trajectory with respect to the change of a stability derivative (see Section 6.3).

$$\left[\nabla_{\hat{\mathbf{p}}} J(\hat{\mathbf{p}})\right] = -\sum_{k=1}^{N}\left[\nabla_{\hat{\mathbf{p}}}\hat{\mathbf{y}}_k\right]^T R^{-1}(\tilde{\mathbf{y}}_k - \hat{\mathbf{y}}_k) \tag{6.13}$$

and

$$\left[\nabla^2_{\hat{\mathbf{p}}} J(\hat{\mathbf{p}})\right] = \sum_{k=1}^{N}\left[\nabla_{\hat{\mathbf{p}}}\hat{\mathbf{y}}_k\right]^T R^{-1}\left[\nabla_{\hat{\mathbf{p}}}\hat{\mathbf{y}}_k\right] - \sum_{k=1}^{N}\left[\nabla^2_{\hat{\mathbf{p}}}\hat{\mathbf{y}}_k\right] R^{-1}(\tilde{\mathbf{y}}_k - \hat{\mathbf{y}}_k). \tag{6.14}$$

The second gradient may be approximated using the Gauss-Newton approach and its simplified form is shown in Equation 6.15.

$$\nabla^2_{\hat{\mathbf{p}}} J(\hat{\mathbf{p}}) \approx \sum_{k=1}^{N} \left[\nabla_{\hat{\mathbf{p}}} \hat{\mathbf{y}}_k\right]^T R^{-1} \left[\nabla_{\hat{\mathbf{p}}} \hat{\mathbf{y}}_k\right]. \tag{6.15}$$

The method for minimizing the loss function is an iterative process. Each time a J value is calculated it is checked in order to determine whether it falls below the required threshold value (see Section 6.3). If it does not, the stability derivative values are altered slightly and the process is repeated until this threshold requirement is satisfied. In each case the J is a measure of the fit between the experimental and simulated trajectories. The aim is to iterate until a J value that represents the best match for the experimental and simulated trajectories is achieved. The following section provides an explanation pertaining to the generation of the simulated trajectories using a flight dynamic simulation model.

6.2 Flight simulation model

This section describes the flight dynamic model used for simulating trajectories from the stability derivatives and initial flight conditions. The model comprises several steps, the first of which is defining the initial conditions. After Kalman filtering (Chapter 3) the trajectories for each variable, for each flight are stored in matrix form. The initial flight conditions are taken as the fourth point in the trajectory for each of the following parameters stored in this matrix: x_{N0}, y_{E0}, z_{D0}, ϕ_0, θ_0, ψ_0, v_{N0}, v_{E0}, v_{D0}, p_0, q_0, r_0. Using these initial conditions the airspeed, angle of attack and side-slip angle are calculated in the same way as shown in Chapter 4 (Equations 4.10 through 4.12). The aerodynamic coefficients C_L, C_D and C_Y are calculated using Equations 5.1, 5.2 and 5.3 (Chapter 5), where the stability derivatives are those calculated in Chapter 5, and the aerodynamic angles are calculated as described above. The aerodynamic forces D, Y and L are calculated using Equations 4.15 to 4.17.

The aerodynamic moments C_l, C_m and C_n are calculated using Equations 5.4 to 5.6 where the values for the stability derivatives and aerodynamic angles are the same as those mentioned at the beginning of this section. Some of the terms in these equations involve velocities, airspeed and other aircraft constants. During the first simulation the terms containing velocities are calculated using the initial velocities loaded at the beginning of this section, but in later simulations these are replaced by the most recently simulated values. The aerodynamic moments M_x, M_y and M_z are calculated from Equations 4.18 to 4.20.

Using this information the derivatives of the linear velocities ($\dot{u}$, $\dot{v}$, $\dot{w}$) are calculated from Equations 6.16, 6.17 and 6.18. A similar form of these equations is presented on page 166 of Crassisis and Junkins (2004).

$$\dot{u} = vr - wq - gsin\theta + \frac{Lsin\alpha - Dcos\alpha}{m} \tag{6.16}$$

$$\dot{v} = wp - ur + gcos\theta sin\phi + \frac{Y}{m} \tag{6.17}$$

$$\dot{w} = uq - vp + gcos\theta cos\phi - \frac{Dsin\alpha + Lcos\alpha}{m}. \tag{6.18}$$

In Equations 6.16 to 6.18 the linear velocities are given by u, v, w, the angular velocities are given by p, q, r, the aircraft mass is m, gravity is g, and the angle of attack, side-slip and roll angle are given by α, β and ϕ respectively. All the other variables included in these equations are defined in the opening paragraphs of this section.

In a similar fashion, Equations 6.19, 6.20 and 6.21 allow derivatives of the angular velocities ($\dot{p}$, $\dot{q}$, $\dot{r}$) to be obtained. Again, definitions for all these variables except the mass moments of inertia (I_{xx}, I_{yy}, I_{zz}), may be found in the immediately preceding paragraphs. Equivalent forms of these equations are also given on page 166 of Crassisis and Junkins (2004).

$$\dot{p} = \frac{M_x - (I_{zz} - I_{yy})qr}{I_{xx}} \tag{6.19}$$

$$\dot{q} = \frac{M_y - (I_{xx} - I_{zz})pr}{I_{yy}} \tag{6.20}$$

$$\dot{r} = \frac{M_z - (I_{yy} - I_{xx})pq}{I_{zz}}. \tag{6.21}$$

Once derivatives of the linear and angular velocities have been determined they may used, along with a time increment, dt, to calculate the corresponding velocities. Equations 6.22 through 6.27 reveal the required mathematics:

$$u = u + \dot{u}\,dt, \tag{6.22}$$

$$v = v + \dot{v}\,dt, \tag{6.23}$$

$$w = w + \dot{w}\,dt, \tag{6.24}$$

$$p = p + \dot{p}\,dt, \tag{6.25}$$

$$q = q + \dot{q}\,dt, \tag{6.26}$$

$$r = r + \dot{r}\,dt. \tag{6.27}$$

Position and angular derivatives are defined in the following way (Equation 6.28 and 6.29) and are calculated with the results from previous equations presented in this chapter. The same equations are used by Crassisis and Junkins (2004) on page 167.

$$\begin{bmatrix} \dot{x} \\ \dot{y} \\ \dot{z} \end{bmatrix} = \begin{bmatrix} c\theta c\psi & s\phi s\theta c\psi - c\phi s\psi & c\phi s\theta c\psi + s\phi s\psi \\ c\theta s\psi & s\phi s\theta s\psi + c\phi c\psi & c\phi s\theta s\psi - s\phi c\psi \\ -s\theta & s\phi c\theta & c\phi c\theta \end{bmatrix} \begin{bmatrix} u \\ v \\ w \end{bmatrix}, \tag{6.28}$$

$$\begin{bmatrix} \dot{\phi} \\ \dot{\theta} \\ \dot{\psi} \end{bmatrix} = \begin{bmatrix} 1 & sin\phi tan\theta & cos\phi tan\theta \\ 0 & cos\phi & -sin\phi \\ 0 & sin\phi sec\theta & cos\phi sec\theta \end{bmatrix} \begin{bmatrix} p \\ q \\ r \end{bmatrix}. \tag{6.29}$$

Finally the positions and angles may be calculated as follows:

$$x = x + \dot{x}\,dt, \tag{6.30}$$

$$y = y + \dot{y}\,dt, \tag{6.31}$$

$$z = z + \dot{z}\,dt, \tag{6.32}$$

$$\phi = \phi + \dot{\phi}\,dt, \tag{6.33}$$

$$\theta = \theta + \dot{\theta}\,dt, \tag{6.34}$$

$$\psi = \psi + \dot{\psi}\,dt. \tag{6.35}$$

The first flight simulation is run with the initial conditions (fourth point of each experimental trajectory) to generate a trajectory for four of the 16 parameters ("interested outputs") selected for optimization from the Kalman filter output matrix (see Section 6.3). These trajectories are mathematically compared (see Section 6.1.3) to their corresponding experimental trajectories. If they disagree by more than a specified threshold value, each stability derivative is perturbed slightly and the simulation is repeated until the desired

level of agreement is met. This optimization procedure allows the stability derivatives for a particular trajectory to be refined. Each successive simulation entails the use of all the above equations, with the initial conditions and other parameters being updated with the most recently calculated simulated values as they become available. Specific details relating to the implementation of this simulation in the MLE algorithm are presented in Section 6.3.

6.3 MLE Algorithm

All the flight trajectories analyzed in this thesis were run through the MLE algorithm in order to perform a mathematical identification of the system. The data for each trajectory is loaded in matrix form with the following 16 column headers: x_N, y_E, z_D, ϕ, θ, ψ, V, α, β, v_N, v_E, v_D, p, q, r, t. This is a similar approach to that described in the previous section for the initial conditions - loading the desired parameters from a matrix created for storing the data after Kalman filtering (Chapter 3).

For the MLE, four parameters from these 16 are selected as "interested outputs" or variables that need to be optimized. Along with the "interested outputs", the lateral-directional and vertical-longitudinal stability derivatives calculated in Chapter 5 are loaded, and some are designated as parameters to be varied during the simulation. The nature of each flight being optimized determines whether the initial lateral-directional or vertical-longitudinal stability derivatives are used for a particular set of simulations. The covariance matrix is also an important part of the algorithm and is briefly mentioned in Section 6.1.3. For this simulation the covariance matrix is a 4 x 4 square zero matrix with the diagonals being the variance of each of the "interested outputs".

For a lateral-directional flight the following stability derivatives have a greater influence and are therefore selected as parameters to be varied/refined during the simulation: C_{Y0}, $C_{Y\beta}$, C_{l0}, $C_{l\beta}$, C_{n0}, $C_{n\beta}$. In addition to these six, C_{L0}, $C_{L\alpha}$, C_{D0} and $C_{D\alpha}$ are also included as variable parameters because they are relatively strong and although they play a greater role in vertical-longitudinal flight, their effect in lateral-directional flight is significant enough to warrant their inclusion. During the vertical-longitudinal flight simulations C_{L0}, $C_{L\alpha}$, C_{D0}, $C_{D\alpha}$, C_{m0} and $C_{m\alpha}$ are designated as free parameters to be varied and refined. The four remaining stability derivatives C_{lp}, C_{lr}, C_{mq}, C_{np} and C_{nr} are used in the flight simulation equations but are not permitted to vary. Determining which parameters to fix and which to vary during the simulations is a complex task. Some initial trials and preliminary results revealed that categorizing the stability derivatives as above provides the most meaningful results. Allowing too many free parameters during a simulation causes complications and in most of the trial cases yields simulated trajectories that rapidly approached $\pm\infty$. Since C_{lp}, C_{lr}, C_{mq}, C_{np} and C_{nr} are all extremely weak stability derivatives, whether or not they are permitted to vary during the simulation will not have a significant impact on the final trajectory.

6.4 MLE Outputs

Initial trials with the MLE revealed that when attempting the simulation with the entire trajectory, meaningful results are not achievable as the full simulated trajectory begins traveling rapidly toward $\pm\infty$ mid-way through the flight. This phenomenon is apparent in almost all the flight data and several factors could be responsible for the occurrence. The two most likely causes are that either an error exists in the flight simulation model, or that the instabilities portrayed by the stability derivatives in Chapter 5 indeed play a significant role in effecting the MLE simulation results.

The first is checked by running the simulation model with stability derivatives, initial conditions and physical parameters for the Boeing-747. These parameters were obtained from Crassisis and Junkins (2004) and the results are shown in Figures 6.1 and 6.2 for an initial forward velocity of 205.13 ms^{-1} and an initial altitude of 6096 m. The same simulations are performed for the Butterfly data and are shown in Figures 6.3 and 6.4, with initial forward velocity and altitude values of 2 ms^{-1} and 3 m respectively. Each of these figures displays a legend that includes a vector showing the values for the three initial angles, $[\phi\,\theta\,\psi]$. These figures clearly demonstrate the expected behavior for the Boeing-747, but in the case of the Butterfly the resulting flights are not as predictable and the trajectories all demonstrate severe turns which begin early on in the flight. Thus the nature of these results proves that the simulation is functioning correctly.

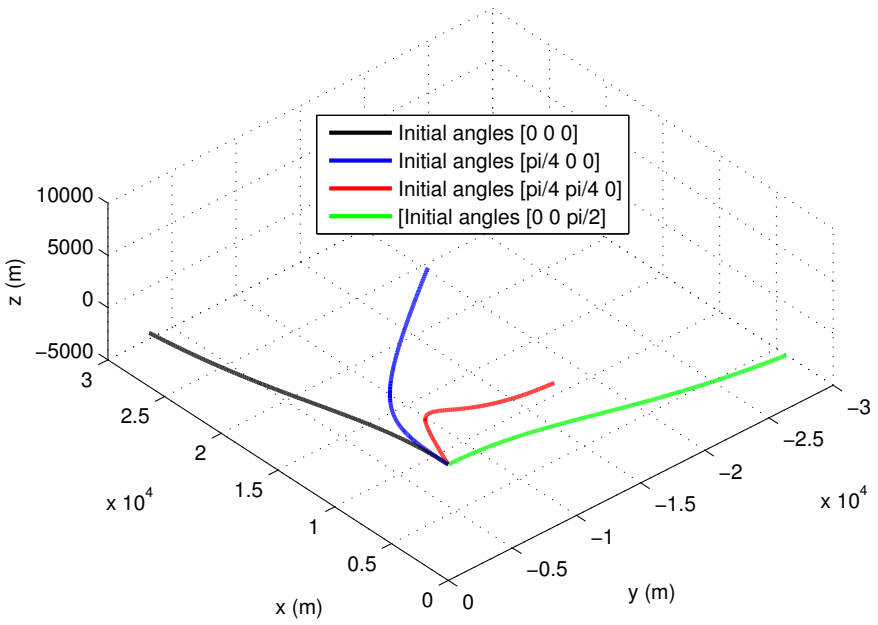

Figure 6.1: Various simulated trajectories (viewed from above) for the Boeing-747 all with an initial forward velocity of 205.13 ms^{-1} and an initial altitude of 6096 m.

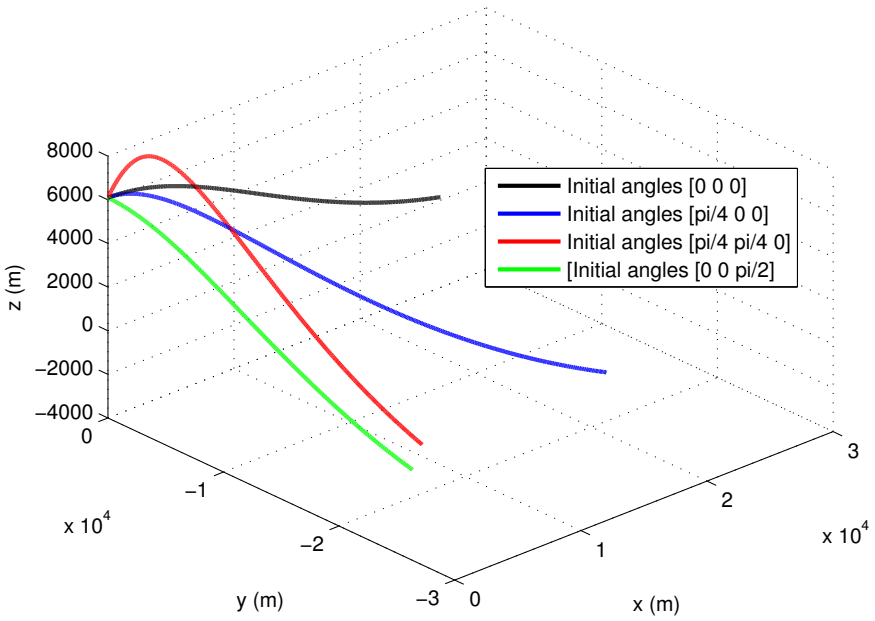

Figure 6.2: Various simulated trajectories (viewed side-on) for the Boeing-747 all with an initial forward velocity of 205.13 ms^{-1} and an initial altitude of 6096 m.

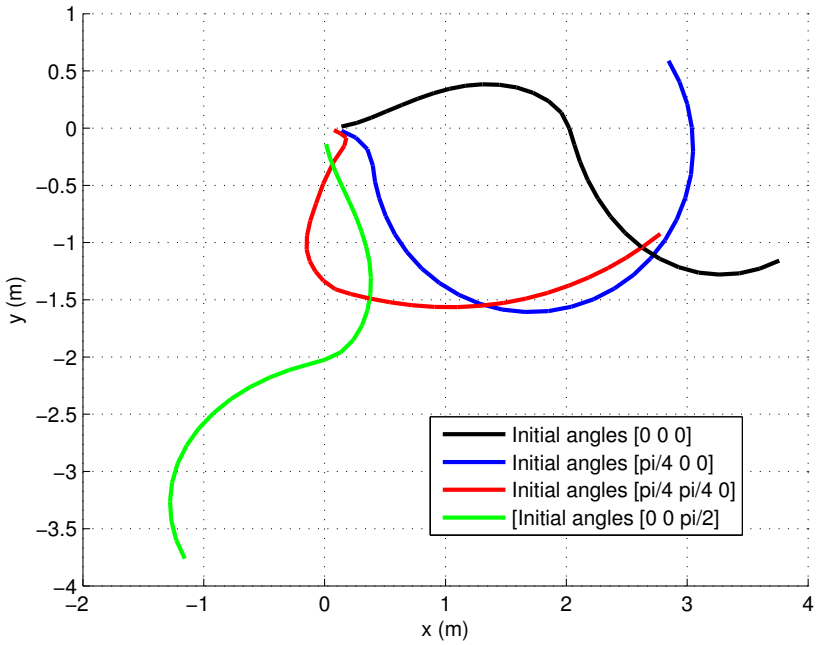

Figure 6.3: Simulated trajectories (viewed from above) for the MAV with the same color-coding as shown in Figure 6.1 for the simulated Boeing-747 trajectories. All the MAV simulations start with a forward velocity of 2 ms^{-1} and an initial altitude of 3 m.

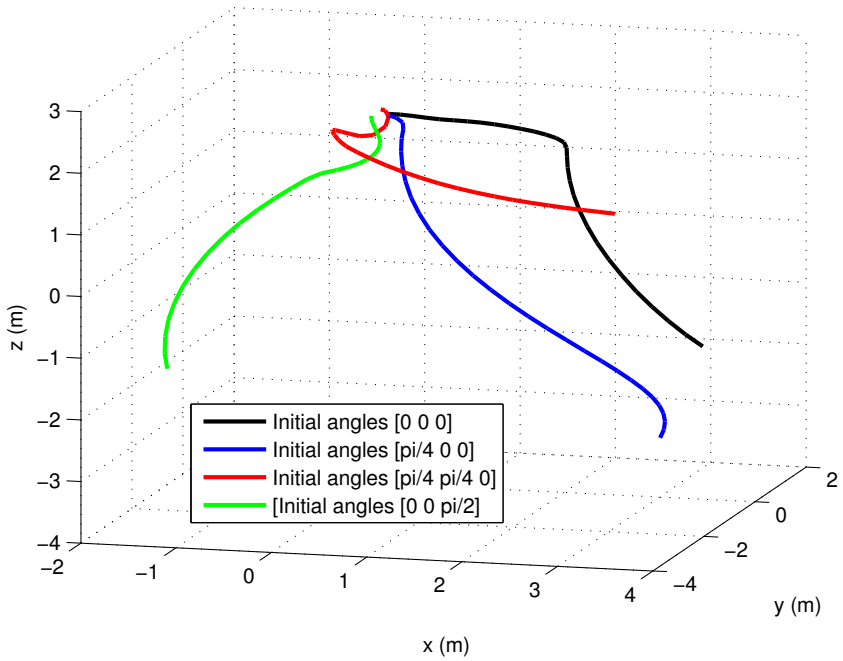

Figure 6.4: Simulated trajectories (viewed side-on) for the MAV with the same color-coding as shown in Figure 6.1 for the simulated Boeing-747 trajectories. All the MAV simulations start with a forward velocity of $2\,\mathrm{ms}^{-1}$ and an initial altitude of 3 m.

Eliminating the simulation model as the source of the observed discrepancy leaves only the stability derivatives as possible culprits. Chapter 5 reveals that several of the stability derivative values fall into an unstable category, and thus the obvious conclusion is that these result in the negative effects associated with the trajectories obtained during MLE. To investigate this further, plots of the time histories for various parameters involved in the flights are created and some are included in Figures 6.5, 6.6 and 6.7 for the Boeing-747 and Figures 6.8, 6.9 and 6.10 for the MAV. As with the simulated trajectories, the variation of the parameters for the Boeing-747 produces aerodynamically intuitive results. However, in the case of the MAV oscillations and instabilities are abundant.

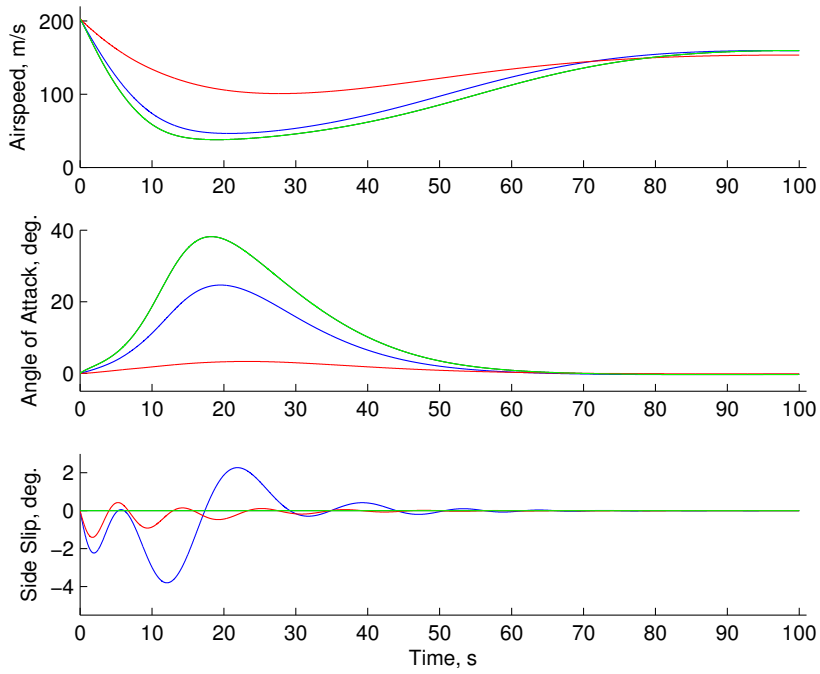

Figure 6.5: Airspeed, angle of attack and side-slip angle for the simulated Boeing-747 trajectories displayed in Figures 6.1 and 6.2. The previous color scheme is maintained in these plots.

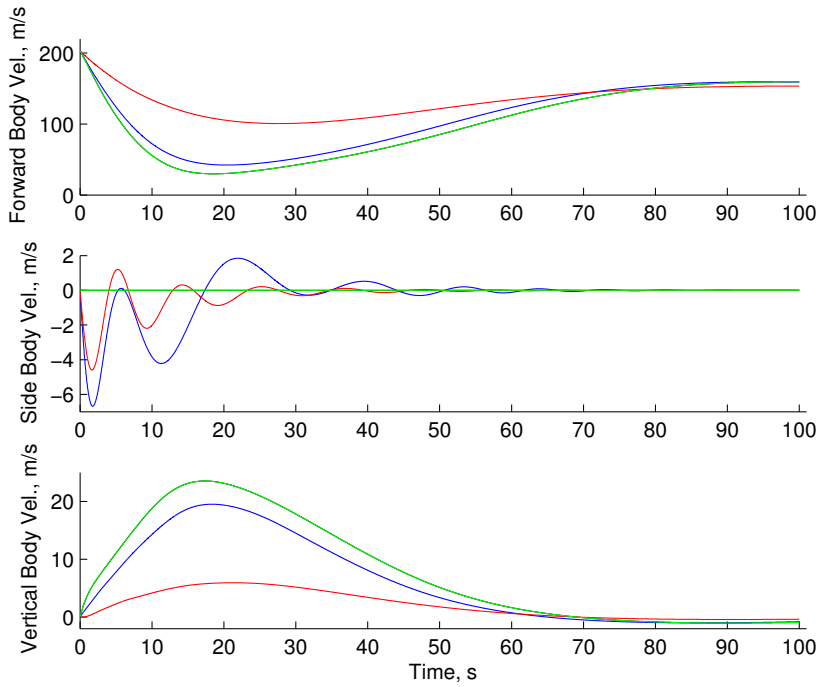

Figure 6.6: Forward body velocity, side body velocity and vertical body velocity for the simulated Boeing-747 trajectories displayed in Figures 6.1 and 6.2. The previous color scheme is maintained in these plots.

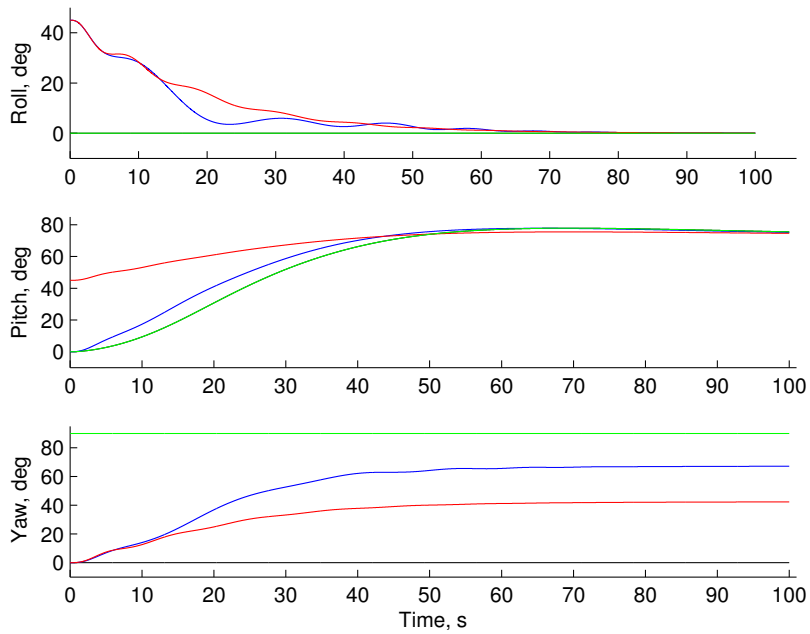

Figure 6.7: Roll angle, pitch angle and yaw angle for the simulated Boeing-747 trajectories displayed in Figures 6.1 and 6.2. The previous color scheme is maintained in these plots.

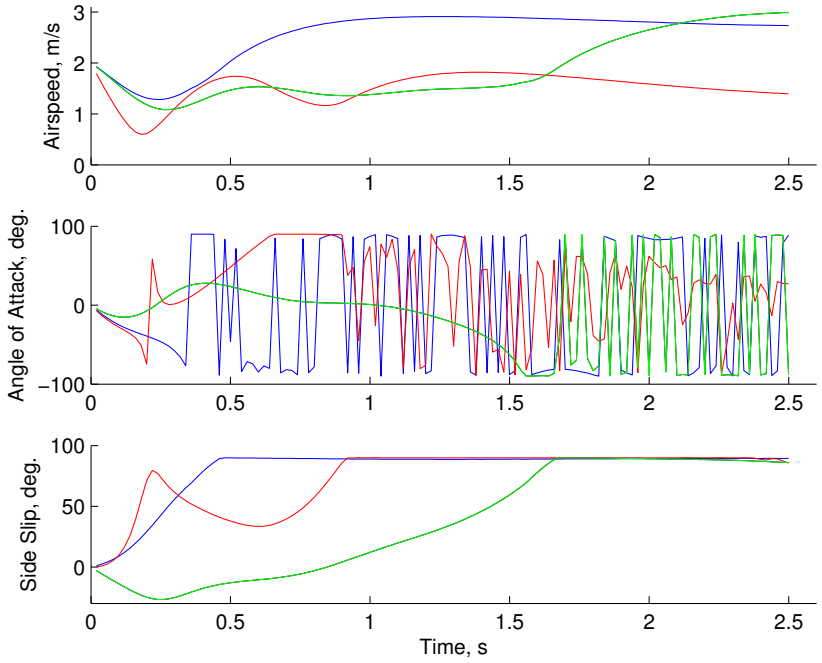

Figure 6.8: Airspeed, angle of attack and side-slip angle for the simulated MAV trajectories displayed in Figures 6.3 and 6.4. The previous color scheme is maintained in these plots.

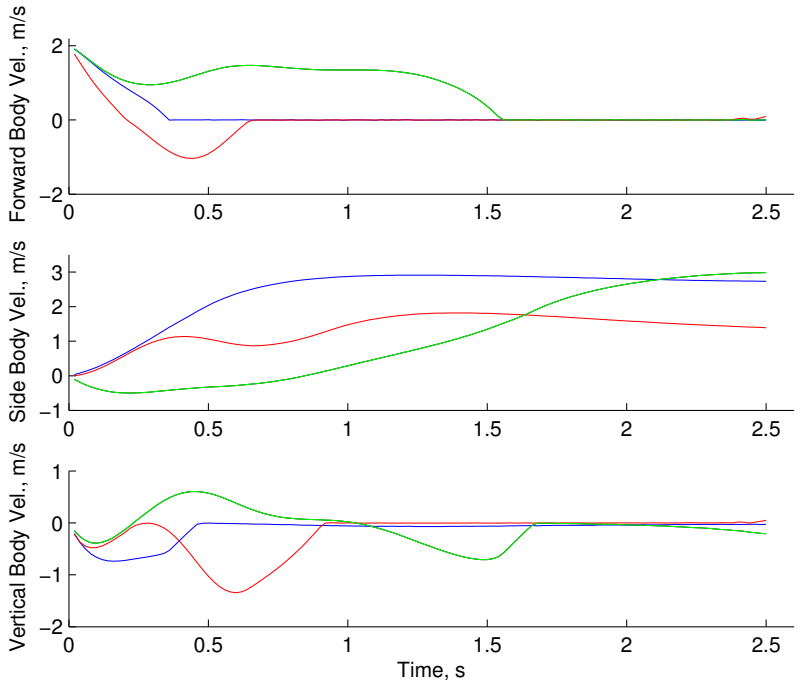

Figure 6.9: Forward body velocity, side body velocity and vertical body velocity for the simulated MAV trajectories displayed in Figures 6.3 and 6.4. The previous color scheme is maintained in these plots.

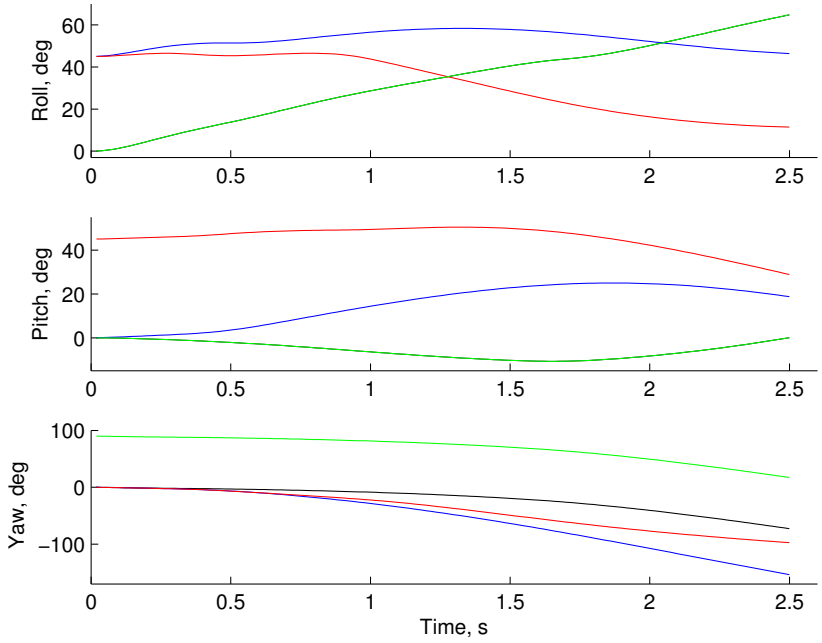

Figure 6.10: Roll angle, pitch angle and yaw angle for the simulated MAV trajectories displayed in Figures 6.3 and 6.4. The previous color scheme is maintained in these plots.

In order to pursue the MLE and achieve the desired goal of testing the algorithm and identifying the aerodynamic system, a small alteration to the analysis is make. Instead of using the entire MAV trajectory, only the first portion of the trajectory (about a third) is used for the remainder of the analysis. This is the stable part, before the severe turns starts to dominate and the other parameters become unstable. Although this development is not the ideal situation for testing the simulation, it provides the best option for attempting to validate the system - albeit with only a small sample of the full trajectory.

6.4.1 Lateral-directional example

At the beginning of Section 6.3 the technique for assigning the "free" stability derivatives during a particular set of simulations was discussed. In addition to correctly selecting the "free" stability derivatives, the choice of the "interested outputs" also need to be carefully considered as these play a role in the simulation through their influence within the covariance matrix (Section 6.3). Thus in order to achieve good results it is wise to assign "interested outputs" that are representative of the specific trajectory. After performing multiple simulation trial runs it became clear that superior results could be obtained when implementing x_N, y_E, airspeed and v_N as the four "interested outputs" for the lateral-directional simulation.

Figures 6.11, 6.12, 6.13 and 6.14 show the results of the simulation for butterflyJan10_04 with the threshold for the cost function being set as follows: $J < 0.01$ and $abs(J - Jprev) < 0.001$. In each plot the green data is the butterfly experimental trajectory, the red data is the trajectory after one iteration, and the blue data is the final trajectory. It is clear that in all four plots the initial estimated trajectory is well away from the experimental trajectory (red), but after about 60 iterations a much better match is achieved.

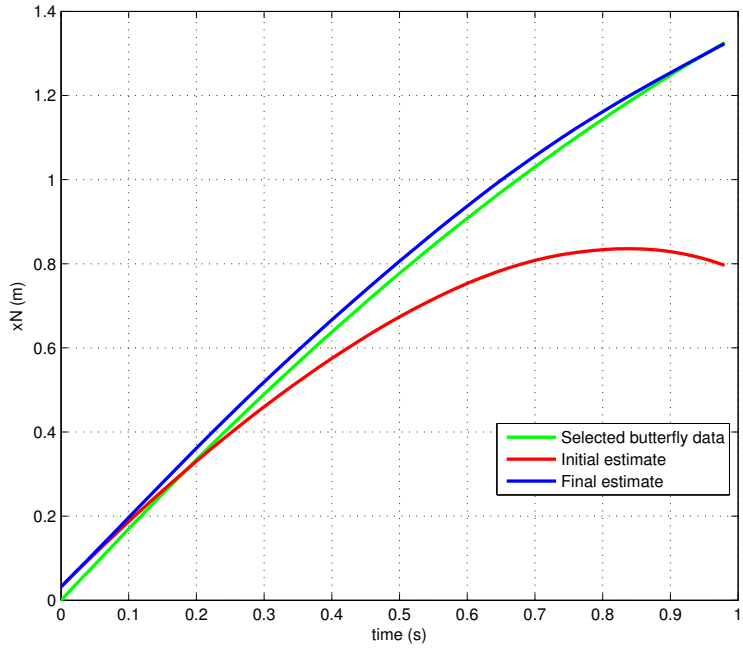

Figure 6.11: "North" x position for the butterflyJan10_04 flight trajectory (green). The initial estimate (red) is calculated through a simulation using the flight dynamic equations and the final estimate (blue) is obtained after implementing the iterative maximum likelihood estimation algorithm.

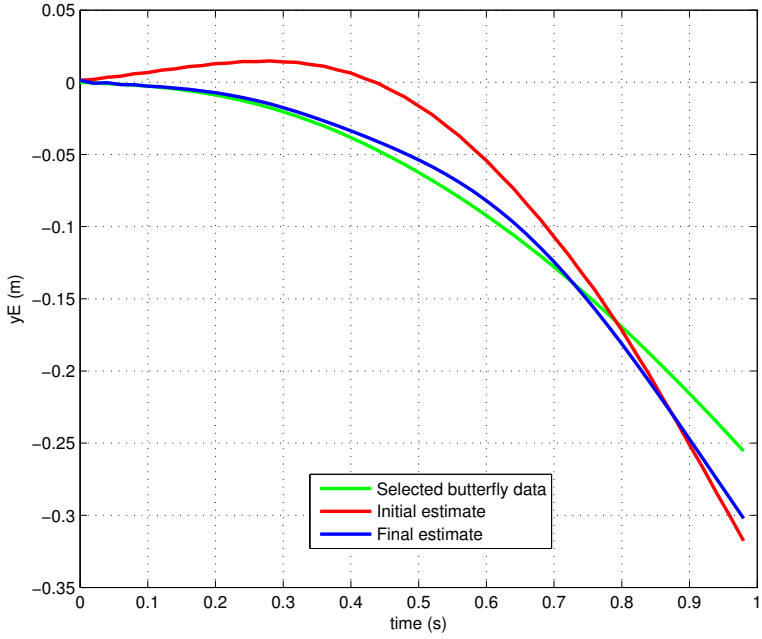

Figure 6.12: "East" y position for the butterflyJan10_04 flight trajectory (green). The initial estimate (red) is calculated through a simulation using the flight dynamic equations and the final estimate (blue) is obtained after implementing the iterative maximum likelihood estimation algorithm.

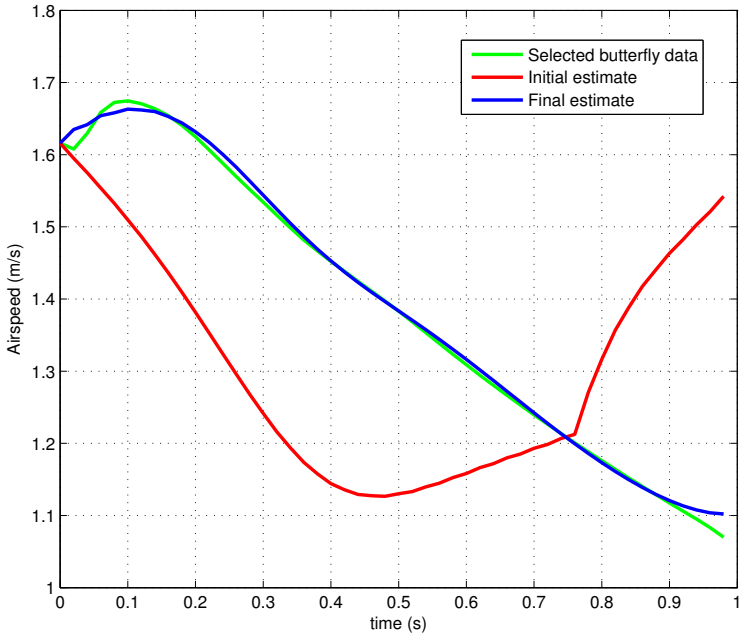

Figure 6.13: Airspeed for the butterflyJan10_04 flight trajectory (green). The initial estimate (red) is calculated through a simulation using the flight dynamic equations and the final estimate (blue) is obtained after implementing the iterative maximum likelihood estimation algorithm.

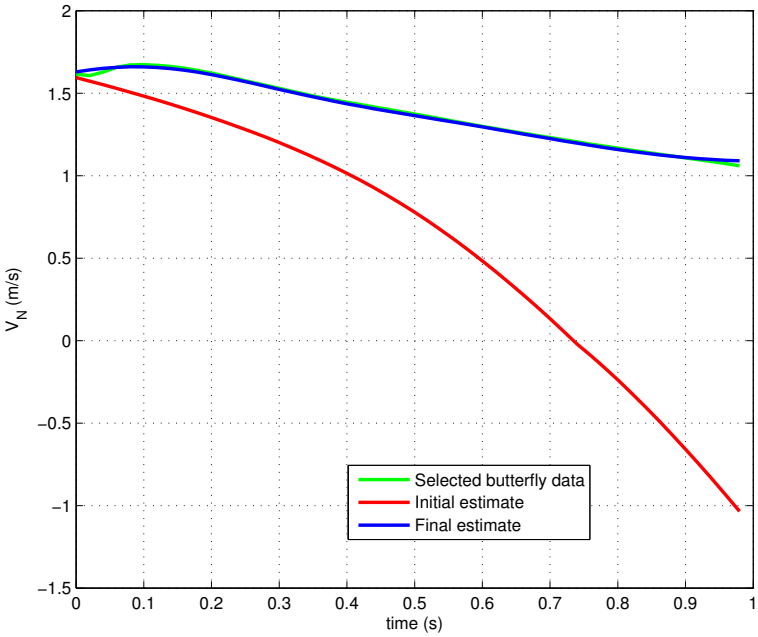

Figure 6.14: "North" velocity for the butterflyJan10_04 flight trajectory (green). The initial estimate (red) is calculated through a simulation using the flight dynamic equations and the final estimate (blue) is obtained after implementing the iterative maximum likelihood estimation algorithm.

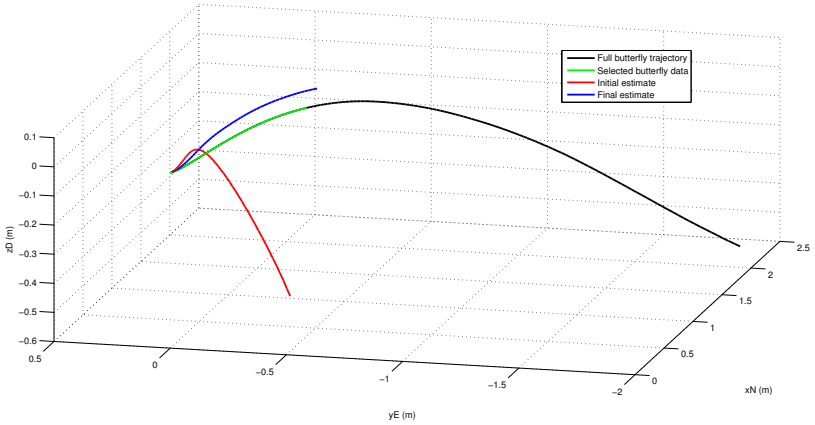

Figure 6.15: Three dimensional trajectories for butterflyJan10_04 showing the full butterfly trajectory (black), the selected data (green), the initial estimate (red) and the final estimate (blue).

The progression of each "free" stability derivative is monitored throughout the simulation and the results are presented in Figures 6.16 through 6.25. A log of the cost function (J) is created during each set of simulations and Figure 6.26 shows it waning with time as the simulated and experimental trajectories converge. The final stability derivatives, final cost function, and selected percentage of the full trajectory for each reliably simulated flight are included in Table 6.1. The final three rows of the table give the weighted mean, variance and initial estimate (Chapter 5) for each stability derivative. The weighted mean was calculated taking into account the value of the cost function, the variance and the fraction of the full experimental trajectory used. In most cases the difference between the two is not too great.

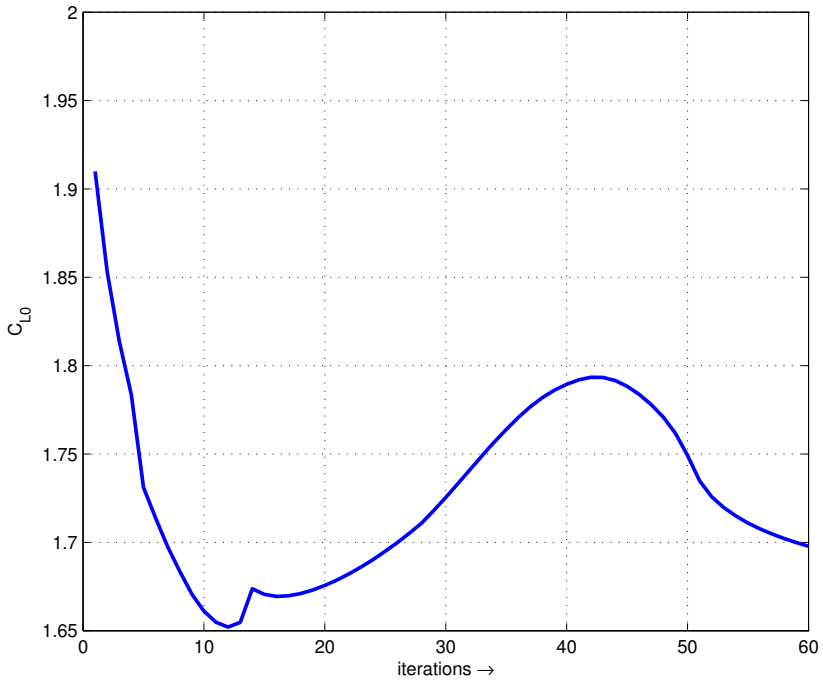

Figure 6.16: The progression of C_{L0} as a function of the number of iterations performed during the maximum likelihood estimation.

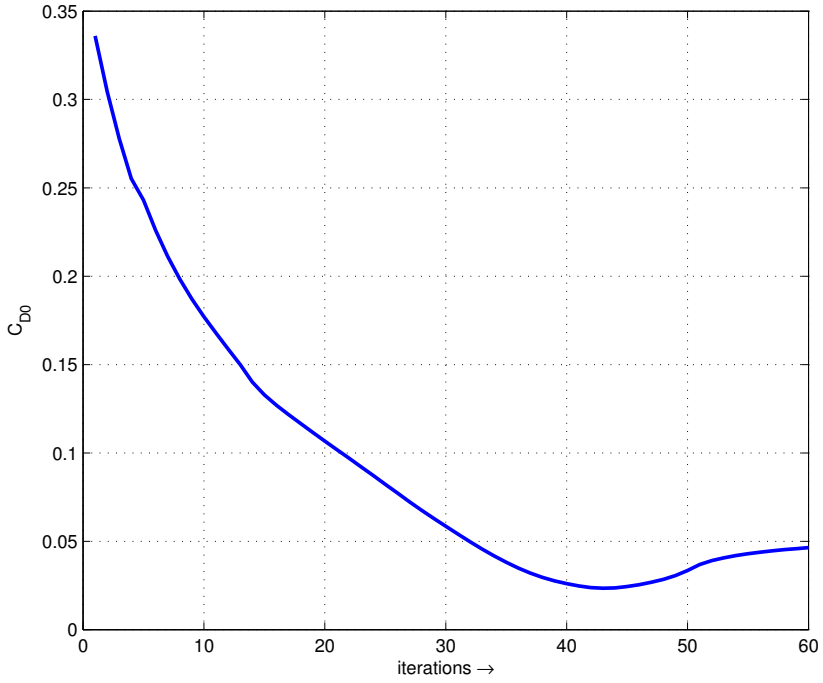

Figure 6.17: The progression of C_{D0} as a function of the number of iterations performed during the maximum likelihood estimation.

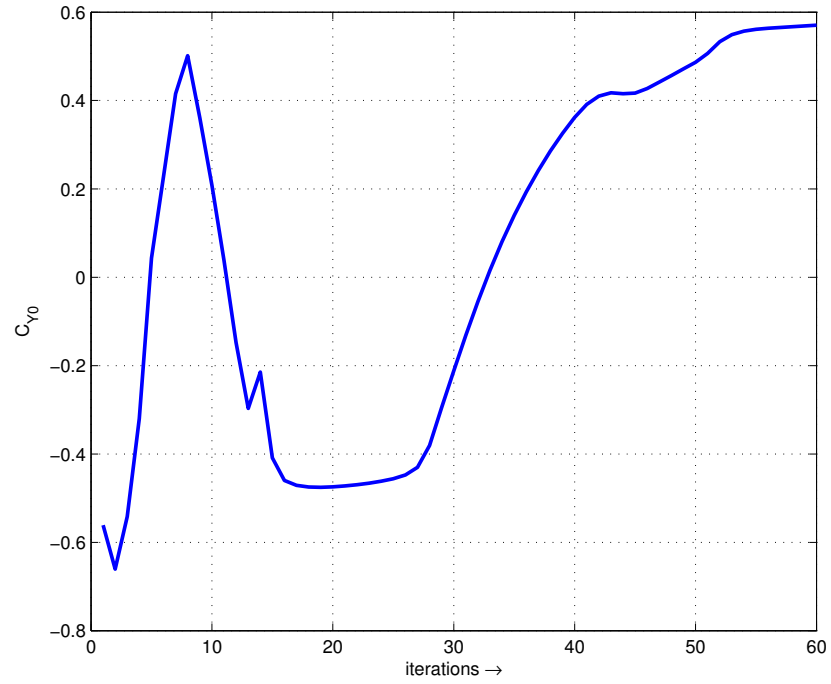

Figure 6.18: The progression of C_{Y0} as a function of the number of iterations performed during the maximum likelihood estimation.

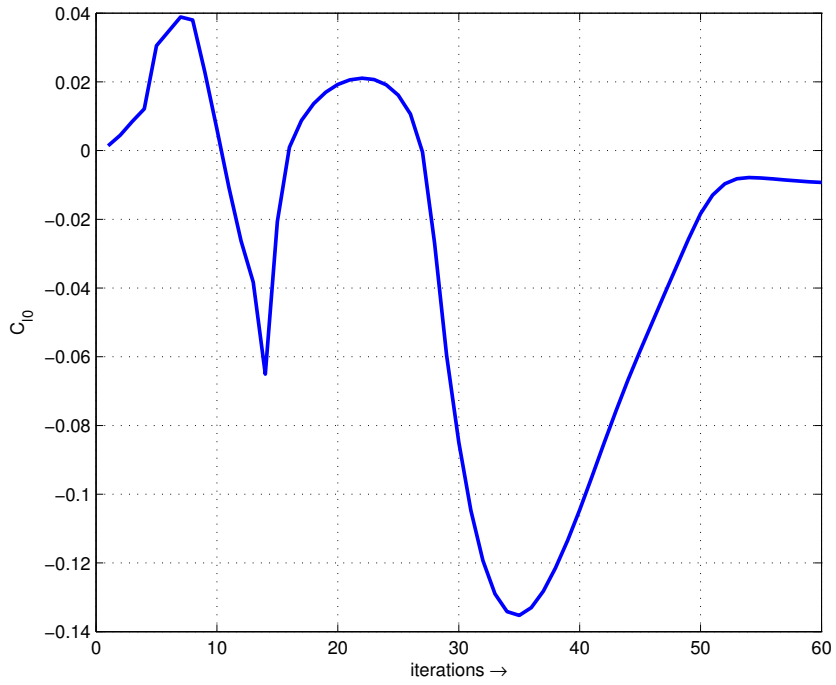

Figure 6.19: The progression of C_{l0} as a function of the number of iterations performed during the maximum likelihood estimation.

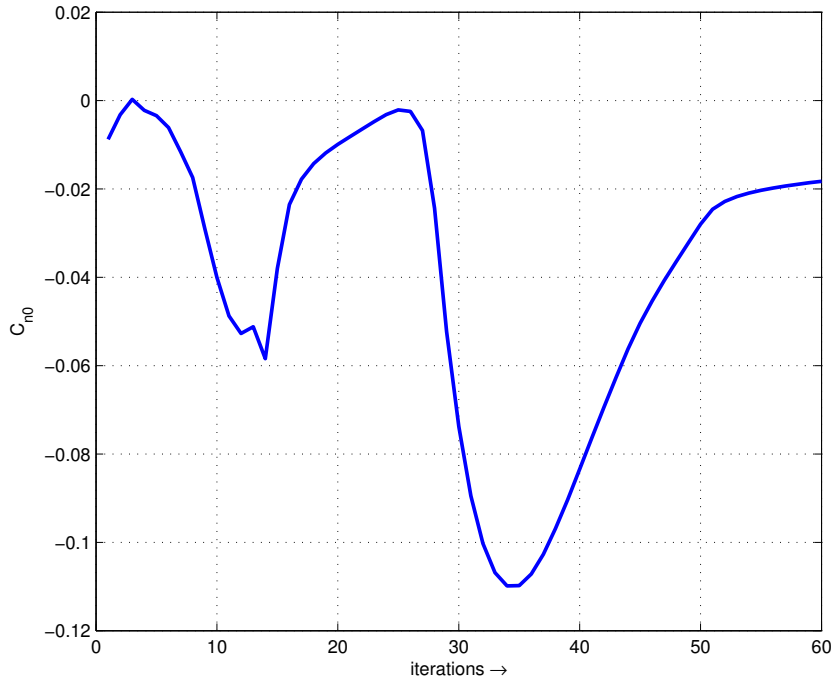

Figure 6.20: The progression of C_{n0} as a function of the number of iterations performed during the maximum likelihood estimation.

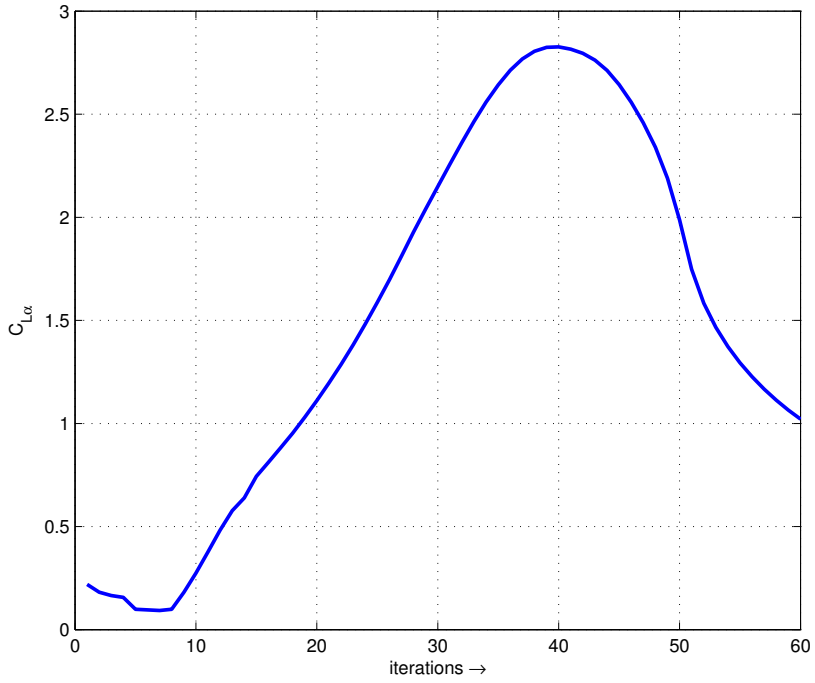

Figure 6.21: The progression of $C_{L\alpha}$ as a function of the number of iterations performed during the maximum likelihood estimation.

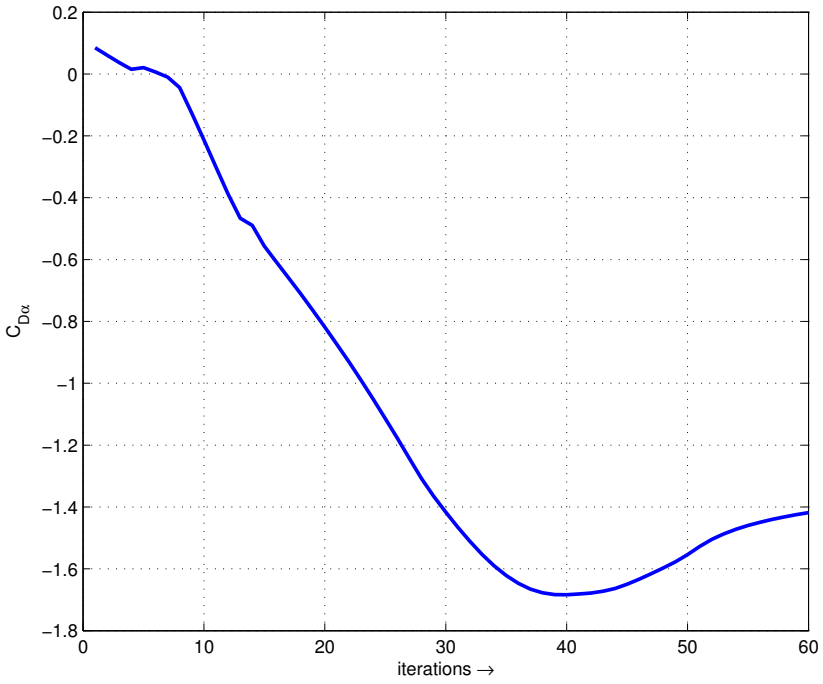

Figure 6.22: The progression of $C_{D\alpha}$ as a function of the number of iterations performed during the maximum likelihood estimation.

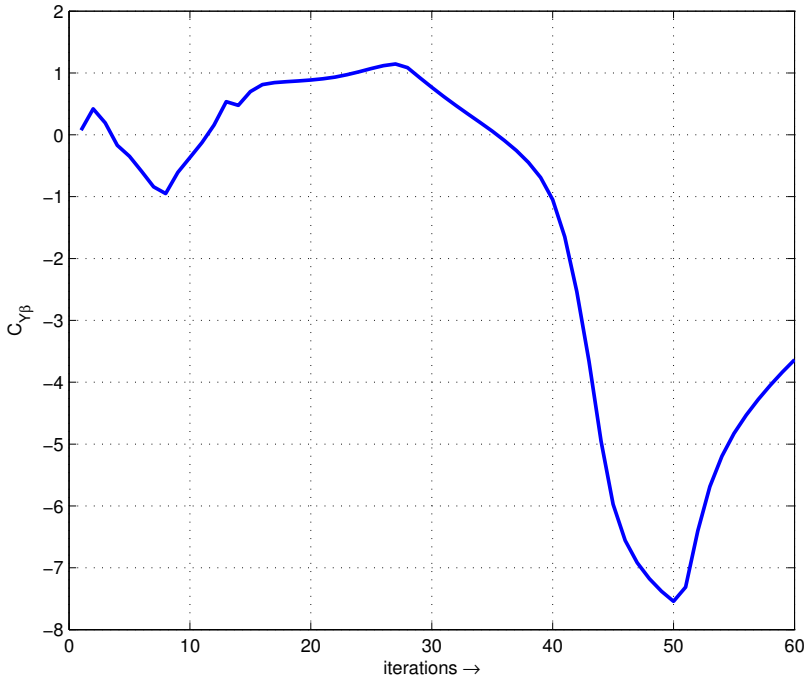

Figure 6.23: The progression of $C_{Y\beta}$ as a function of the number of iterations performed during the maximum likelihood estimation.

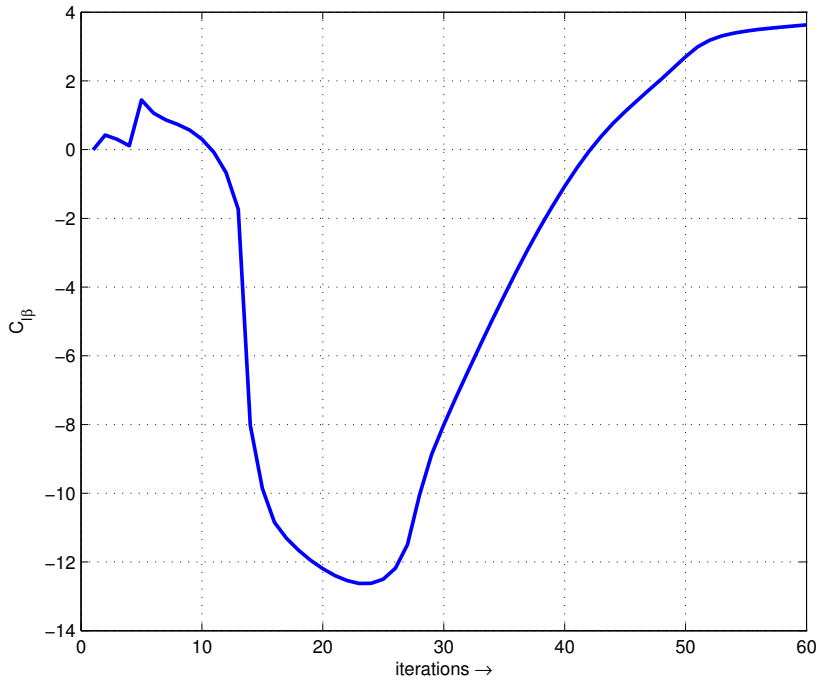

Figure 6.24: The progression of $C_{l\beta}$ as a function of the number of iterations performed during the maximum likelihood estimation.

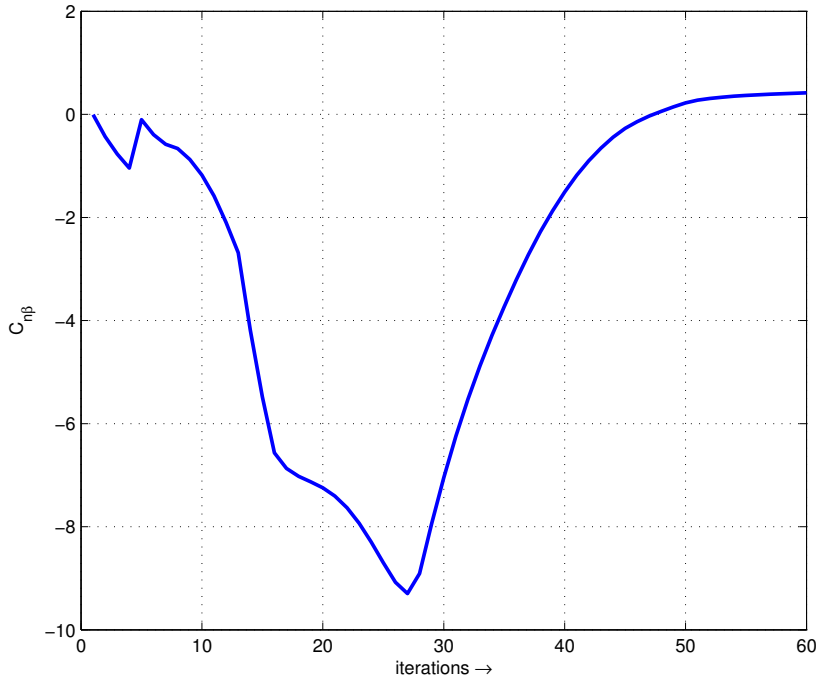

Figure 6.25: The progression of $C_{n\beta}$ as a function of the number of iterations performed during the maximum likelihood estimation.

Table 6.1: Refined lateral-directional stability derivatives obtained during the MLE.

Flight	C_{L0}	C_{D0}	C_{Y0}	C_{l0}	C_{n0}	$C_{L\alpha}$	$C_{D\alpha}$	$C_{Y\beta}$	$C_{l\beta}$	$C_{n\beta}$	J	%
b*Jan10_01	2.0858	-0.0684	-0.6796	-0.0426	-0.0408	6.6089	-3.8586	-8.4944	2.4452	-1.7150	0.0599	28.8
b*Jan10_04	1.6978	0.0464	0.5704	-0.0093	-0.0183	1.0215	-1.4186	-3.6367	3.6276	0.4165	0.0537	33.1
b*Jan10_08	1.3629	-0.0116	-1.9206	0.0898	-0.0597	7.3853	0.2649	-0.5499	-1.0983	-0.1774	0.0527	36.0
b*Jan10_16	2.3296	0.0088	-0.6288	-0.0911	-0.2587	6.2940	-3.4510	-2.1620	-0.6278	-3.1515	0.0818	31.2
b*Jan10_28	1.2611	0.1310	0.3898	0.2516	0.2799	3.8795	0.8102	-12.7957	-2.1301	-2.2162	0.0396	19.5
b*Jan10_29	2.9775	1.0876	-0.7951	-0.1667	0.0397	3.7996	-0.0747	3.9388	1.7968	-0.4472	0.0421	74.1
Average	**2.0603**	**0.2863**	**-0.5703**	**-0.0162**	**-0.0119**	**4.7522**	**-1.1854**	**-2.8990**	**0.8348**	**-1.0893**	–	–
Variance	-2.2924	0.1170	-0.8359	0.0050	-0.0098	-17.7519	-2.6931	-12.3542	-0.0280	-2.4017	–	–
Initial	1.9099	0.3360	-0.5611	0.0014	-0.0088	0.2915	0.0849	-0.0743	-0.0069	-0.0054	–	–

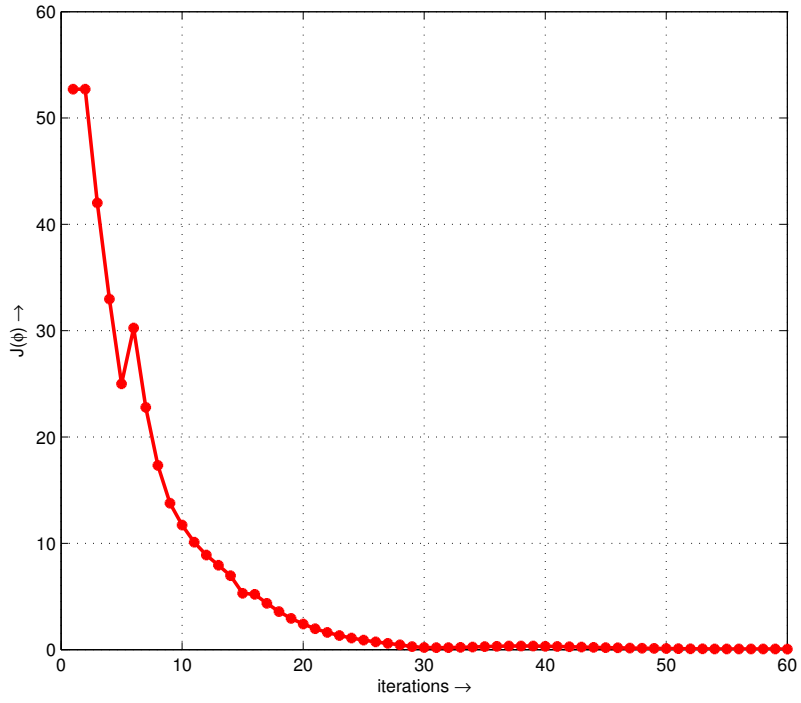

Figure 6.26: The progression of the cost function (J) as a function of the number of iterations performed during the maximum likelihood estimation.

6.4.2 Vertical-longitudinal example

Simulating the vertical trajectories involves a similar method to that explained in the preceding section, and as with the lateral-directional data, the choice of the "interested outputs" is important to the success of the simulation. Initial trials with the vertical-longitudinal data demonstrated satisfactory convergences between experimental and simulated trajectories when x_N, z_D, airspeed and v_N were designated as the "interested outputs". As such, these were used for all the vertical-longitudinal simulations and the results for butterflyJul13_07 are displayed in Figures 6.27 to 6.30.

As with the butterflyJan10_04 data discussed in the previous section, the initial estimate (red) lies far from the experimental trajectory (green) but after about 45 iterations the MLE algorithm generates a final trajectory (blue) with a cost value that falls below the threshold and the simulation is halted. The same cost function constraint as before is applied to the vertical-longitudinal simulations.

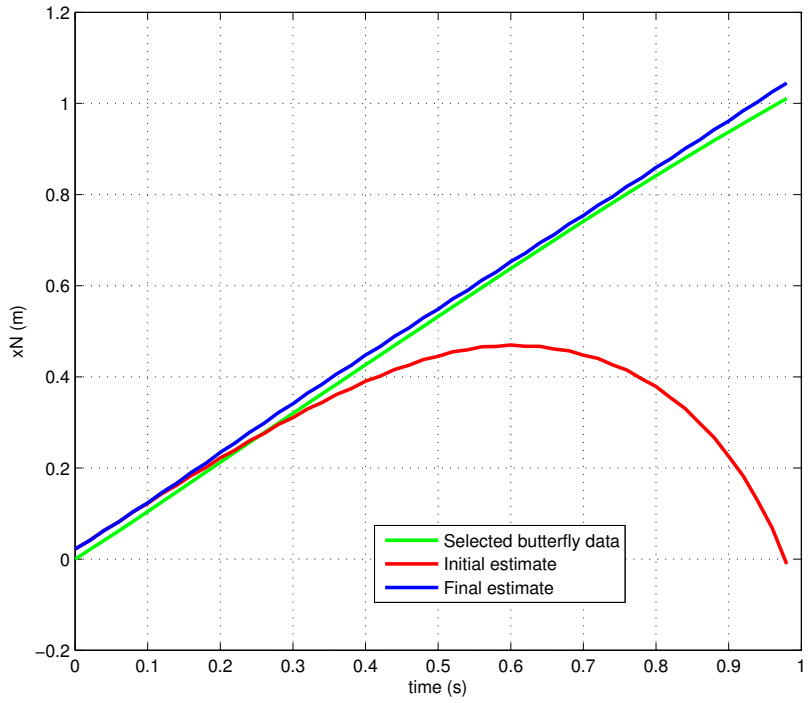

Figure 6.27: "North" x position for the butterflyJul13_07 flight trajectory (green). The initial estimate (red) is calculated through a simulation using the flight dynamic equations and the final estimate (blue) is obtained after implementing the iterative maximum likelihood estimation algorithm.

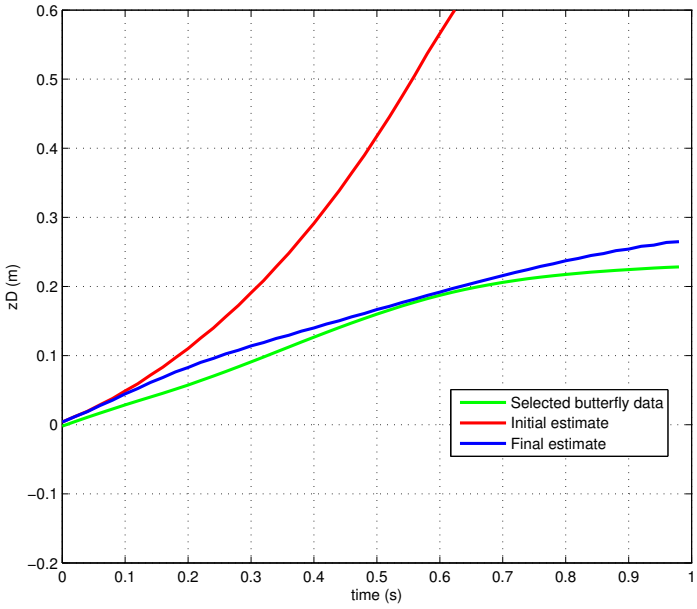

Figure 6.28: "East" z position for the butterflyJul13_07 flight trajectory (green). The initial estimate (red) is calculated through a simulation using the flight dynamic equations and the final estimate (blue) is obtained after implementing the iterative maximum likelihood estimation algorithm.

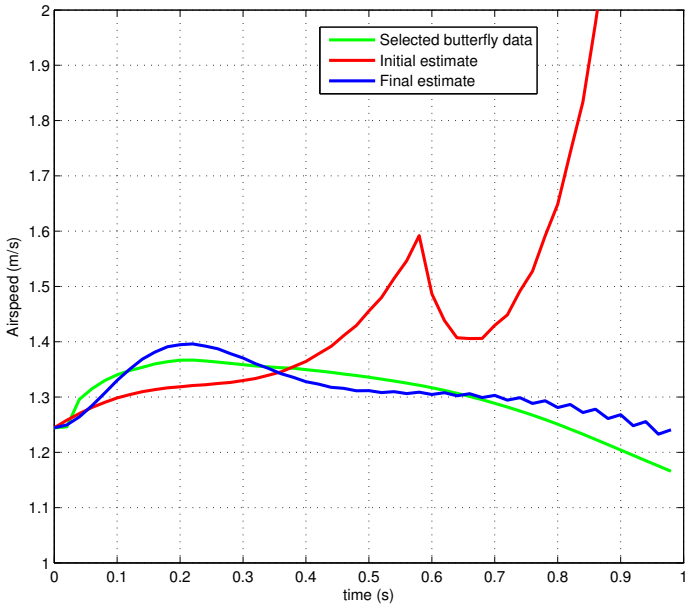

Figure 6.29: Airspeed for the butterflyJul13_07 flight trajectory (green). The initial estimate (red) is calculated through a simulation using the flight dynamic equations and the final estimate (blue) is obtained after implementing the iterative maximum likelihood estimation algorithm.

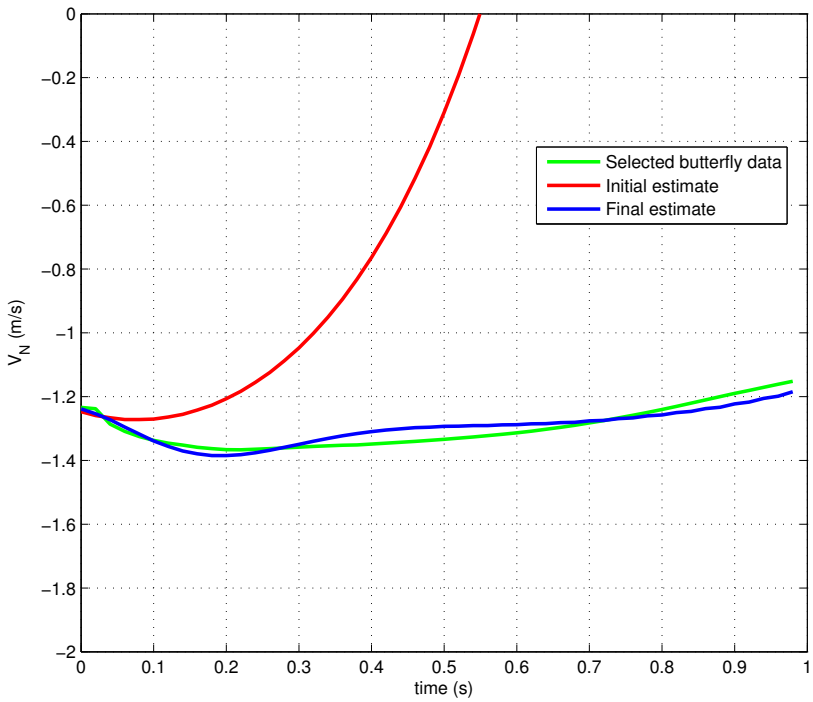

Figure 6.30: "North" velocity for the butterflyJul13_07 flight trajectory (green). The initial estimate (red) is calculated through a simulation using the flight dynamic equations and the final estimate (blue) is obtained after implementing the iterative maximum likelihood estimation algorithm.

It is not surprising that like the lateral-directional simulated trajectories, these vertical-longitudinal ones also only produce reliable results for the first third of the flight. The same explanation applies for this case and the portion of the trajectory used is shown in Figure 6.31.

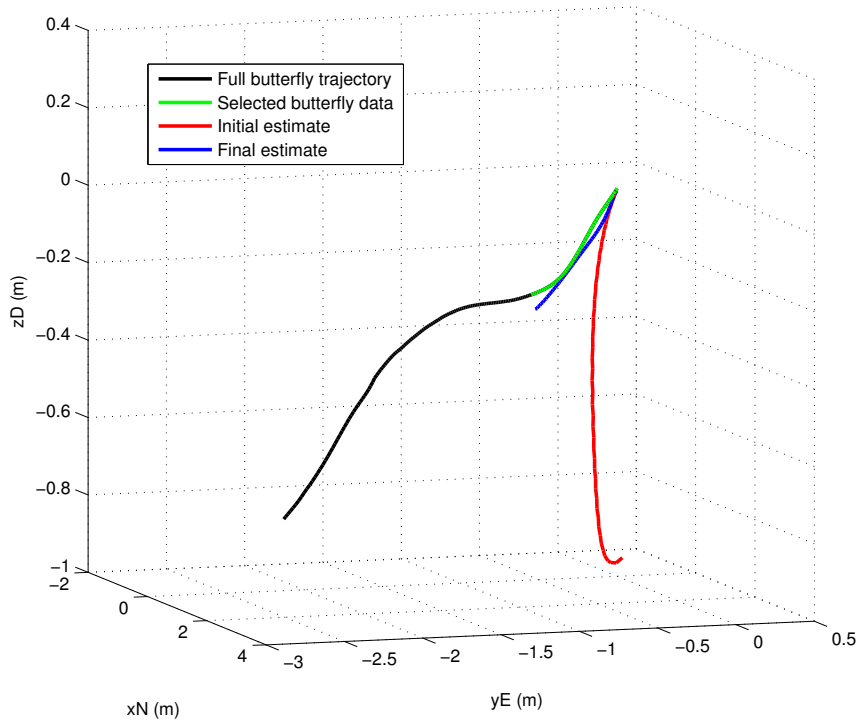

Figure 6.31: Three dimensional trajectories for butterflyJul13_07 showing the full butterfly trajectory (black), the selected data (green), the initial estimate (red) and the final estimate (blue).

The following six figures (Figures 6.32 to 6.37) show the progression of each of the selected stability derivatives as a function of MLE iteration number. The final figure (Figure 6.38) displays a declining cost function as the experimental and simulated trajectories converge during the 45 iterations. Table 6.2 summarizes the results from several vertical-longitudinal flight simulations. The final stability derivatives for each flight, the cost function, and the selected percentage of the full trajectory are tabulated. As with the Table 6.1, rows with the weighted mean, variance and the initial stability derivative values from Chapter 5 are included.

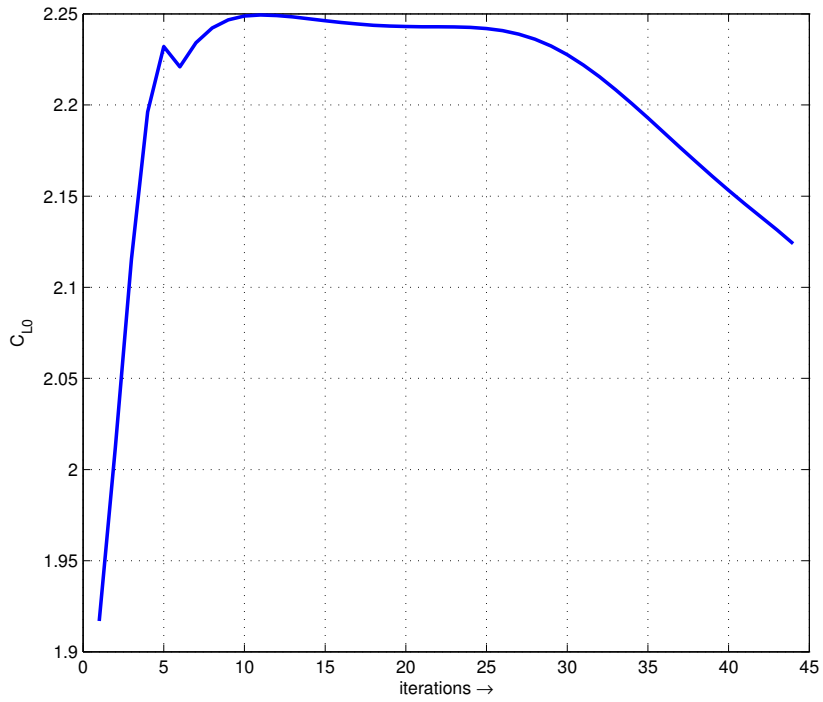

Figure 6.32: The progression of C_{L0} as a function of the number of iterations performed during the maximum likelihood estimation.

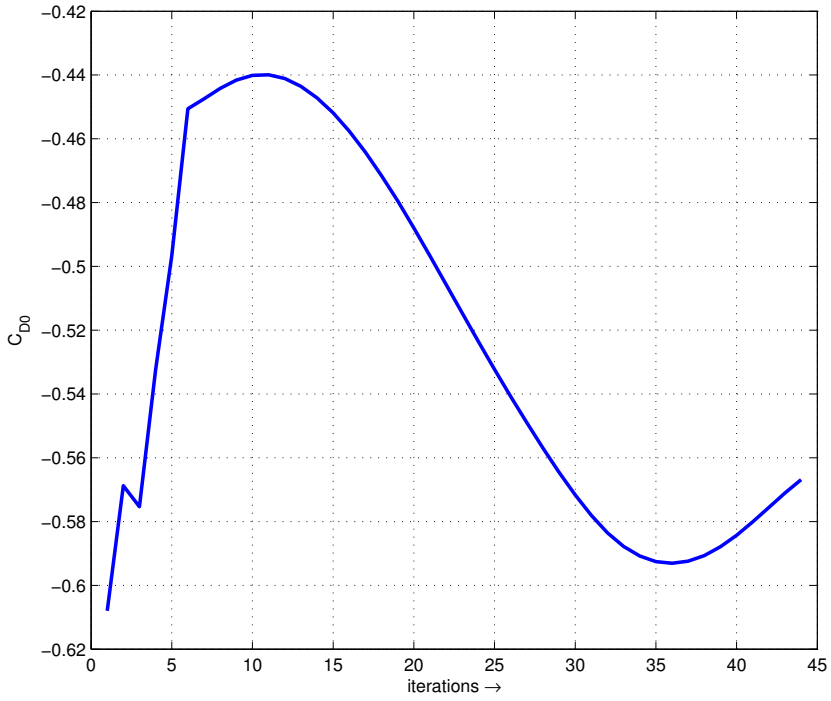

Figure 6.33: The progression of C_{D0} as a function of the number of iterations performed during the maximum likelihood estimation.

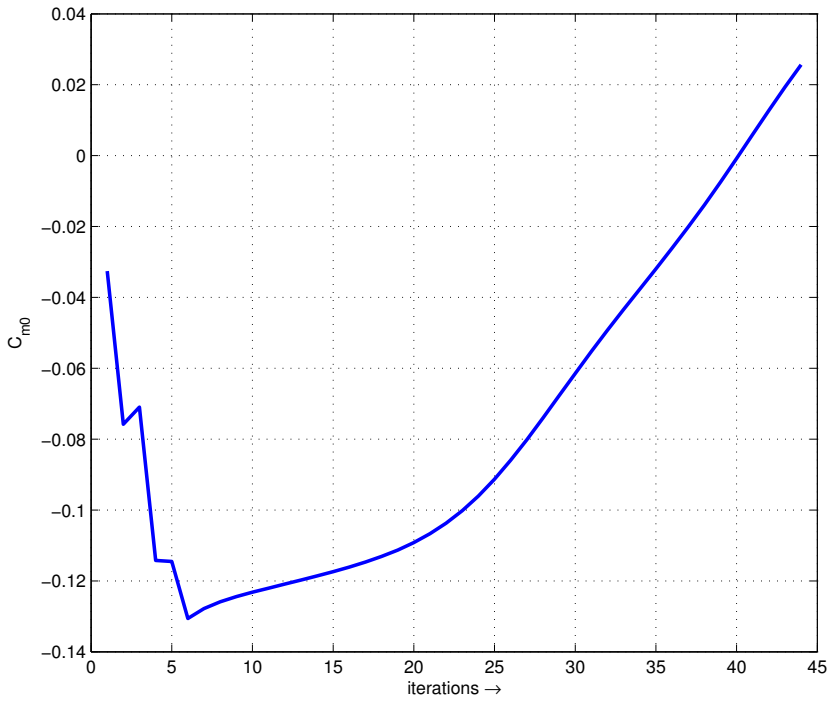

Figure 6.34: The progression of C_{m0} as a function of the number of iterations performed during the maximum likelihood estimation.

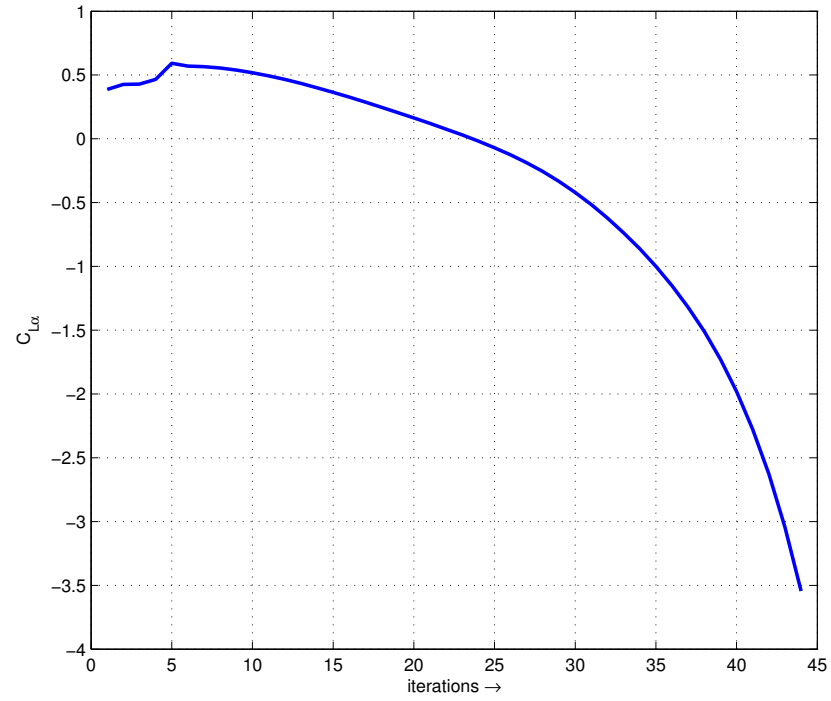

Figure 6.35: The progression of $C_{L\alpha}$ as a function of the number of iterations performed during the maximum likelihood estimation.

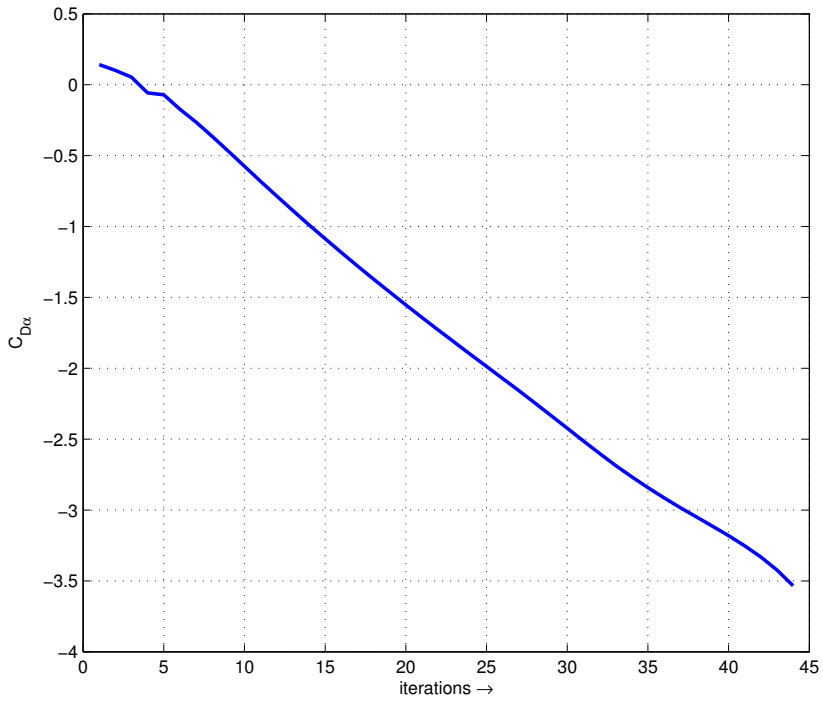

Figure 6.36: The progression of $C_{D\alpha}$ as a function of the number of iterations performed during the maximum likelihood estimation.

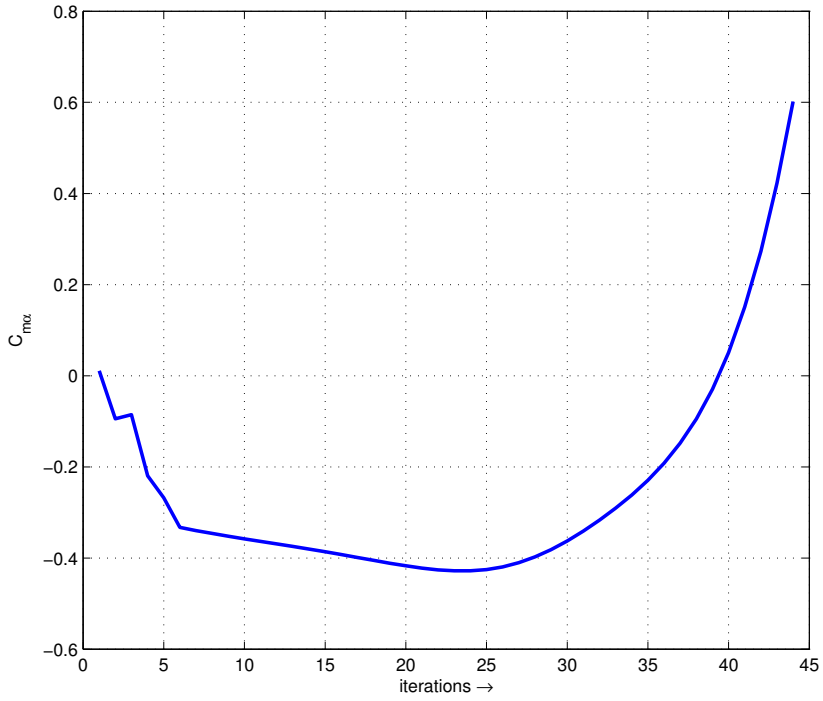

Figure 6.37: The progression of $C_{m\alpha}$ as a function of the number of iterations performed during the maximum likelihood estimation.

Table 6.2: Refined vertical-longitudinal stability derivatives obtained during the MLE.

Flight	C_{L0}	C_{D0}	C_{m0}	$C_{L\alpha}$	$C_{D\alpha}$	$C_{m\alpha}$	J	%
b*Jul13_01	2.4492	-0.2844	0.0061	0.3521	-0.8439	0.1719	0.4422	29.8
b*Jul13_02	2.6198	-0.0314	0.0163	-13.3298	-5.0035	-0.5585	0.1195	28.2
b*Jul13_04	2.8035	-0.1446	0.2569	-3.4964	1.2008	2.9226	0.1506	30.1
b*Jul13_05	2.1240	-0.5669	0.0256	-3.5443	-3.5341	0.6017	0.1169	28.4
b*Jul13_06	2.4068	-0.7258	0.0472	-8.5833	-10.2066	0.7298	0.1087	32.3
b*Jul13_07	1.9336	-0.6633	-0.0182	-10.8072	6.1257	4.2901	0.0543	27.2
b*Jul13_10	3.2317	-0.9487	-0.0137	-2.1822	-1.4979	-0.7352	0.1052	30.9
b*Jul13_13	1.9272	-0.2572	-0.0137	-2.3583	-2.1882	-0.4749	0.1420	36
b*Jul13_15	2.5284	-0.0994	0.0001	-6.3952	-2.7737	-0.7599	0.0755	37.3
Average	**2.4454**	**-0.4138**	**0.0333**	**-5.6899**	**-2.1551**	**0.6588**	–	–
Variance	0.1576	0.0919	0.0066	18.0831	17.4678	2.8088		
Initial	1.9169	-0.6080	-0.0326	0.3870	0.1423	0.0107	–	–

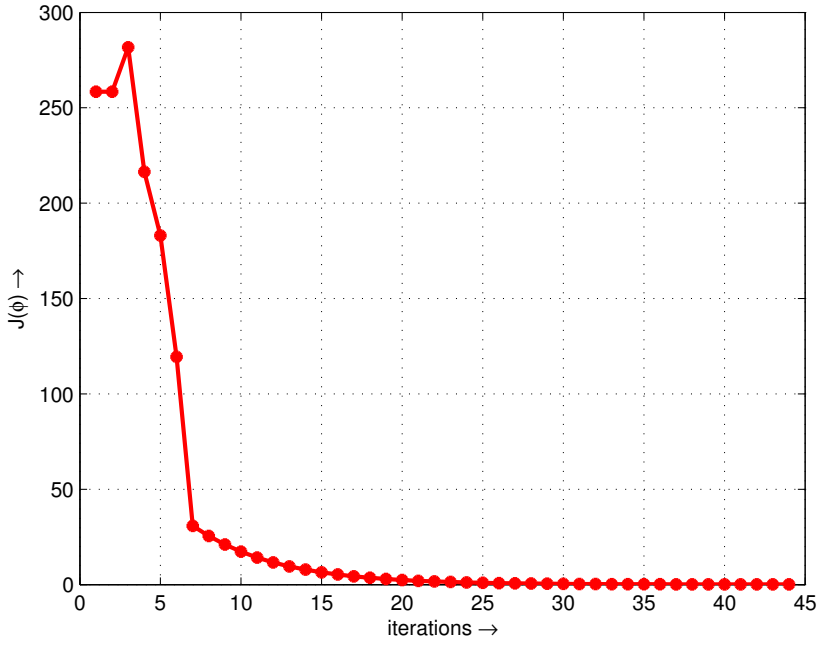

Figure 6.38: The progression of the cost function (J) as a function of the number of iterations performed during the maximum likelihood estimation.

6.5 System validation

The weighted means of the stability derivatives displayed in Tables 6.1 and 6.2 are the most accurate stability derivatives for the butterfly aircraft, derived from experimental flight data using the method of MLE. To test the quality of these stability derivatives, and hence the validity of the aircraft model, they are loaded into the MLE algorithm and one flight is simulated. To claim a validated aerodynamic model for the aircraft, these new stability derivatives must reproduce any experimental trajectory using the corresponding initial conditions.

This procedure was performed for all the data and the best match (butterflyJul13_05) is displayed in Figure 6.39. The black trajectory represents the experimental data, the green trajectory represents the selected experimental data, the blue trajectory represents the final estimate after iterating, and the red trajectory represents the validated trajectory. The trajectory is generated using the averaged vertical-longitudinal stability derivatives and the initial conditions for butterflyJul13_05.

For a single simulation without iterating, this is an excellent result. It reveals that through the MLE simulation the initial estimates for the vertical-longitudinal stability derivatives calculated in Chapter 5 have been refined such that they "almost" reproduce the experimental trajectory. Although a satisfying result, this success is limited to only a few vertical-longitudinal cases and is even less likely when performing a similar test for the lateral-directional data.

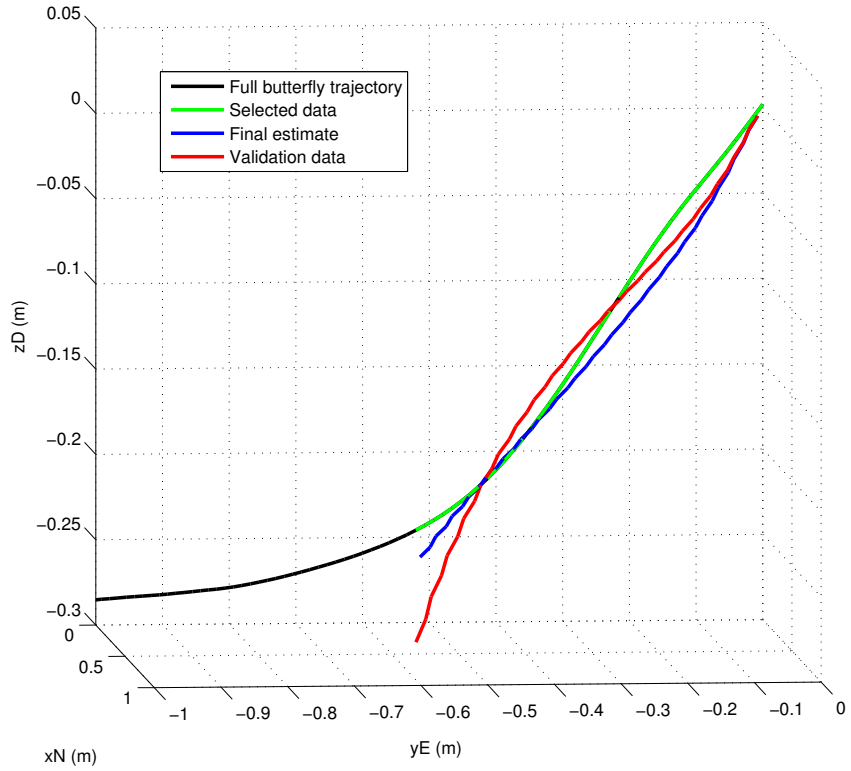

Figure 6.39: The butterflyJul13_07 flight trajectory showing the experimental data (black), selected experimental data (green), final estimate after iterating (blue) and the validated trajectory (red).

6.6 System identification summary

This chapter describes the concept of system identification and a technique (Maximum Likelihood Estimation) for performing it. For each of the 28 flights, the initial conditions and initial stability derivatives (Chapter 5) are used in an aerodynamic simulation to generate a flight trajectory. This new trajectory is mathematically compared with the corresponding experimental trajectory, and if the two disagree by more than a certain specified threshold value (cost function, J), the stability derivatives are perturbed slightly and the simulation is repeated with the new stability derivatives and the most recent initial conditions. This iterative MLE process allows the stability derivatives to be refined as the experimental and simulated trajectories converge.

This method is carried out on the lateral-directional and vertical-longitudinal data separately, using the associated initial stability derivatives. Example plots for one lateral-directional and one vertical-longitudinal case are presented. For each flight the refined stability derivatives, cost function, and portion of the flight used are tabulated. The weighted average for each stability derivative is then re-load and the algorithm is re-run to produce a final trajectory from which a system validation can be made.

Ideally, re-running the simulation with these averaged stability derivatives and the initial conditions for any experimental trajectory should result in a simulated trajectory that closely matches the experimental trajectory. In this analysis only a few vertical-longitudinal trajectories produced comparable results. This demonstrates the creation of a successful aerodynamic model, but further refinement is necessary before a confident claim regarding the system validation can be made.

Chapter 7

Conclusion and future work

The work presented in this thesis explores an exciting, new approach for studying the aerodynamic behavior of micro aerial vehicles (MAVs). To date the commonly used techniques for investigating MAV aerodynamics are similar to those employed for large scale aircraft and usually involve wind tunnels (Shields and Mohseni 2010) and/or computational fluid dynamic algorithms (Shyy et al. 2008). This alternate method, vision based motion tracking, is unique in that it allows trajectory data from a full experimental flight to be captured as the aircraft position and attitude vary naturally throughout the flight - unlike the two techniques mentioned above.

The aim is to extract and refine aerodynamic coefficients and stability derivatives to create a validated aerodynamic simulation model. The aerodynamic model could eventually be used to replace or supplement the experimental data, i.e. experimental MAV flight data could be generated with the simulation model rather than physically in the laboratory.

The aircraft selected for this project is the remote controlled Butterfly (Plantraco 2008). The motor and other electronics are removed to allow it to be used as a glider, thus providing the advantage of performing the experiment in stationary atmospheric conditions which result in reduced complexity of the aerodynamic equations required for the analysis (Kundak and Mettler 2007). The experiment is conducted in a laboratory that is fitted with six Vicon cameras (Vicon 2006). Reflective markers located on the aircraft enable it to be tracked, thus permitting the collection of position and attitude data throughout each flight.

Following successful data collection, a Kalman filter (Chapter 3) is implemented to minimize the effects caused by drop-outs in the data, and to generate linear and angular velocities and accelerations. Aerodynamic forces, moments and angles are extracted from the filtered flight data and are required for calculating the aerodynamic coefficients (Chapter 4).

The bulk of the analysis for this thesis is presented in Chapters 5 and 6. Here the procedure for generating linear stability derivatives from the aerodynamic coefficients is carried out. During the stability derivative analysis, several regions in the flight trajectories revealed that they could not be well approximated using a linear aerodynamic model. Further invest-

igation led to the assumption that these regions are the result of the aircraft transitioning through a stall - thus leading to turbulent airflow and a breakdown in the credibility of the equations used to describe the aerodynamics at these particular locations.

Although the linear aerodynamic model cannot be used to generate reliable coefficients for the entire flight trajectory, it performs reputably for the majority of the flight data. Since these stability derivatives are the best that can currently be obtained with the Butterfly data, they are used as initial estimates within the maximum likelihood estimation simulation (Chapter 6).

For each of the 28 flights analyzed in this thesis, the initial conditions and initial stability derivatives are used in an aerodynamic simulation to generate a new flight trajectory. This new trajectory is mathematically compared with the corresponding experimental trajectory, and if the two disagree by more than a certain specified threshold value (cost function, J), the stability derivatives are perturbed slightly and the simulation is repeated with the new stability derivatives and most recent initial conditions. This iterative process is defined as maximum likelihood estimation and allows the stability derivatives to be refined as the experimental and simulated trajectories converge.

The weighted average for each stability derivative is then computed and the simulation is re-run to produce a final trajectory from which a system validation can be made. Ideally, re-running the simulation with these averaged stability derivatives and the initial conditions, for any experimental trajectory, should result in a simulated trajectory that closely matches the experimental trajectory. In this analysis only a few vertical-longitudinal trajectories produced comparable results. This demonstrates the creation of a successful aerodynamic simulation model, but further refinement is necessary before a confident claim regarding the system validation can be made.

A number of tasks should be attempted in the future to further the current standing of the work presented in this thesis. Collecting additional data in order to obtain more representative initial estimates for the stability derivatives, as well as to reduce the instabilities detected in the data is one such task. In addition, increasing the length of the flight or the portion that exhibits laminar flow is essential for success. As well as these modifictions, including into the simulation model some effects related to the aeroelastic properties and behavior of the aircraft would certainly be beneficial. So far, this analysis has focussed only on aerodynamic effects and all aeroelastic properties are neglegted. Once a stable validated model is produced, the next step would be to introduce and model contol inputs and effects.

The work undertaken for this thesis may be thought of as the pilot project for the pursuit of greater research in this area. During this thesis a number of challenges have been encountered and overcome, while at the same time new ones are revealed as the exploration of this unchartered MAV aerodynamic territory is advanced. This research has outlined a clear pathway along which significant future discoveries relating to the host of fascinating MAV aerodynamic phenomena can be made.

Bibliography

Anderson, J. D. (**2001**). *Fundamentals of Aerodynamics, third edition edn.* McGraw-Hill.

Babister, A. W. (**1961**). *Aircraft Stability and Control.* Pergamon Press, London, England.

Bar-Shalom, Y., Li, X. R., and Kirubarajan, T. (**2001**). *Estimation with Application to Tracking and Navigation.* John Wiley and Sons.

Burk, S. C. W. (**1975**). "Radio-Controlled Model Design and Testing Techniques for Stall/Spin Evaluation of General-Aviation Aircraft." *National Business Aircraft Meeting.*

Campbell, C. C. and Maciejowski, J. M. (**2009**). "Control and guidance of a highly-flexible micro air vehicle using predictive control." *AIAA conference on Guidance, Navigation and Control.*

Chabalko, C. C., Snyder, R. D., and Beran, P. S. (**2009**). "The Physics of an Optimized Flapping Wing Micro Air Vehicle." *47th AIAA Aerospace Science Meeting.*

Cook, M. V. (**2007**). *Flight Dynamic Principles.* Elsevier Ltd., Oxford, UK.

Cox, A., Monopoli, D., Cveticanin, D., Goldfarb, M., and Garcia, E. (**2002**). "The Development of Elastodynamic Components for Piezoelectrically Actuated Flapping Micro Air Vehicles." *Journal of Intelligent Material Systems and Structures.*

Crassisis, J. L. and Junkins, J. L. (**2004**). *Optimal Estimation of Dynamical Systems.* Chapman and Hall/CRC.

Dalton, S. (**1975**). "Borne on the Wind." *Reader's Digest Press.*

Davis, W. R. J., Kosicki, B. B., Boronson, D. M., and Kostishack, D. F. (**1996**). "Micro Air Vehicles for Optical Surveillance." *The Lincoln Laboratory Journal*, 9: 197–213.

Dickinson, M. H. (**1996**). "Unsteady Mechanics of Force Generation in Aquatic and Aerial Locomotion." *American Zoologist*, 36: 537–554.

Duncan, W. J. (**1959**). *The Principles of the Control and Stability of Aircraft.* Cambridge University Press.

Ellington, C. P. (**1984**). "Morphological Parameters, The Aerodynamics of Hovering Insect Flight." *Philosophical Transactions of the Royal Society of London*, 305: 17–40.

Ellington, C. P. (**1991**). "Aerodynamics and the Origin of Insect Flight." *Advances in Insect Physiology*, 23: 171–210.

Ellington, C. P. and Pedley, T. J. (**1995**). "Biological Fluid Dynamics." *Company of Biologists.*

Fisher, R. A. (**1920**). *Contributions to Mathematical Statistics (collection of papers).* Wiley, New York.

Gallington, R. W., Merman, H., Entzminger, J., Francis, M. S., and Palmore, P. (**1996**). "Unmanned Aerial Vehicles." *Future Advances in Aeronautical Systems, AIAA.*

Grasmeyer, J. and Keenon, M. (**2001**). "Development of the Black Widow Micro Air Vehicle." *AIAA Paper*, 9.

Hamel, P. G. and Jategaonkar, R. V. (**1996**). "Evolution of Flight Vehicle System Identification." *Journal of Aircraft.*

Hundley, R. O. and Gritton, E. C. (**1994**). "Future Technology Driven Revolutions in Military Operations: Results of a Workshop." *RAND Corp.*

Iliff, K. W. (**1989**). "Parameter Estimation of Flight Vehicles." *Journal of Guidance, Control and Dynamics*, 12: 261–280.

Jategaonkar, R. V. (**2006**). *Flight Vehicle System Identification: A Time Domain Methodology.* AIAA.

Kalman, R. E. and Bucy, R. S. (**1961**). "New Results in Linear Filtering and Prediction Theory." *Journal of Basic Engineering*, pages 95–108.

Kornbluh, R. (**2002**). "Project Mentor: Biologically Inspired Platform." *Keynote Presentation at the 8th AIAA/CEAS Aeronautics Conference.*

Kundak, N. and Mettler, B. (**2007**). "An Experimental and Methodical Framework for Evaluating Autonomous Control Algorithms for Agile Aerial Vehicles." *European Control Conference ECC, Greece.*

Lewis, F. L. (**1986**). *Optimal Estimation with an Introduction to Stochastic Control Theory.* John Wiley and Sons, New York, NY.

McMichael, J. M. and Francis, C. (**1997**). "Micro Air Vehicles - Towards a New Dimension of Flight." *Technical report, DARPA.*

Mettler, B. (**2010**). "Extracting Micro Air Vehicles Aerodynamic Forces and Coefficients in Free Flight using Visual Motion Tracking Techniques." *Experiments in Fluids*.

Michelson, R. (**1998**). "Update on Flapping Wing Micro Air Vehicle Research - Ongoing Work to Develop a Flapping Wing, Crawling Entomopter."

Michelson, R., Helmick, D., Reece, S., and Amarena, C. (**1997**). "A Reciprocating Chemical Muscle (RCM) for Micro Air Vehicle Entomopter Flight." *1997 Proceedings of the Association for Unmanned Vehicle Systems*.

Morris, S. J. (**1997**). "Design and Flight Test Results for Micro-Sized Fixed-Wing and VTOL Aircraft." *1st international Conference on Emerging technologies for Micro Air Vehicles*.

Mueller, T. (**1985**). "The influence of laminar separation and transition on low Reynolds number airfoil hysteresis." *Journal of Aircraft*, 22: 763–770.

Mueller, T. J. (**2001**). "Fixed and Flapping Wing Aerodynamics for Micro Air Vehicle Applications." *Progress in Astronautics and Aeronautics, AIAA*.

Nachtigall, W. (**1974**). *Insects in Flight*. McGraw-Hill.

NASA (**2009**). "GSFC Wallops UAV Database." *http://uav.effnasa.gov/uav*.

Nicoud, J. D. and Zufferey, J. C. (**2002**). "Toward indoor flying robots." *IEEE International Robotics Systems Conference*.

Nordwall, B. D. (**1997**). "Micro Air Vehicles Hold Great Promise, Challenges." *Aviation Week and Space Technology*, 146: 67, 68.

Pelletier, A. and Mueller, T. J. (**2000**). "Low reynolds number aerodynamics of low-aspect-ratio, thin/flat/ cambered-plate wings." *AIAA Journal of Aircraft*, 37: 825–832.

Pines, D. J. and Bohorquez, F. (**2006**). "Challenges Facing Future Micro-Air-Vehicle Development." *Journal of Aircraft*, 43.

Plantraco (**2008**). "Butterfly Living Room Flyer." *http://www.microflight.com/Online-Catalog/All-Butterfly-Replacement-Parts/Butterfly-Livingroom-Flyer*.

Pornsin-Sirirak, T. N., Lee, S. W., Nasses, H., Grasmeyer, J., Tai, Y. C., Ho, C. M., and Keenon, M. (**2000**). "MEMS Wing Technology for Battery Powered Ornithopter." *Proceedings of the 13th IEEE Annual International Conference on MEMS*, 9: 779–804.

Rayner, J. M. V. (**1988**). "Form and Function in Avian Flight." *Current Ornothology*, 5: 1–66.

Rhinehart, M. and Mettler, B. (**2008**). "Extracting aerodynamic coefficients using direct trajectory sampling." *AIAA-2008-6899. AIAA Conference on Guidance Navigation and Control.*

Roskam, J. (**1986**). *Airplane Flight Dynamics and Automatic Flight Controls.* Roskam Aviation and Engineering Corporation, Ottawa, Kansas.

Samuel, P., Sirohi, J., Rudd, L., Pines, D., and Perel, R. (**2000**). "Design and Development of a Micro Coaxial Rotorcraft." *Proceedings of the AHS Vertical Lift Aircraft Design Conference.*

Schlesinger, S., Buyan, J. R., Callender, E. D., Clarkson, W. K., and Perkins, F. M. (**1974**). "Developing Standard Procedures for Simulation Validation and Verification." *Proceedings of the Summer Computer Simulation Conference.*

Sequeira, I., Willis, D. J., and Peraire, J. (**2006**). "Comparing aerodynamic models for numerical simulation of dynamics and control of aircraft." *44th AIAA Aerospace Sciences Meeting and Exhibit Reno, Nevada.*

Shevell, R. S. (**1989**). *Fundamentals of Flight.* Second Edition. Prentice Hall Inc., New Jersey, USA.

Shields, M. and Mohseni, K. (**2010**). "Static Aerodynamic Loading and Stability Considerations for a Micro Aerial Vehicle." *AIAA.*

Shyy, W., Lian, Y., Tang, J., Liu, H., Trizilla, P., Stanford, B., Bernal, L., Cesnik, C., Friedmann, P., and Ifju, P. (**2008**). "Computational Aerodynamics of Low Renolds Number Plunging, Pitching and Flexible Wings for MAV Applications." *46th AIAA Aerospace Science Meeting.*

Stengle, R. F. (**1994**). *Optimal Control and Estimation.* Dover Publications, New York, NY.

Stengle, R. F. (**2004**). *Flight Dynamics.* Princeton University Press, Princeton, New Jersey.

Stevens, B. and Lewis, F. (**1992**). *Aircraft Control and Simulation.* John Wiley and Sons Inc.

Stribling, C. B. (**1984**). *BASIC Aerodynamics.* Butterworth and Co Ltd., London, England.

Strogatz, S. H. (**1994**). *Nonlinear Dynamics and Chaos.* Addison Wesley publishing company.

Suit, W. T. (**1972**). "Aerodynamic parameters of the navion airplane extracted from flight data." *NASA Technical Note TN D-6643, NASA*.

unknown (**1998**). "Micro Spy Planes, Inside the World's Smallest Aircraft." *Popular Science*.

Vicon (**2006**). "Vicon mx hardware system reference." *http://www.vicon.com/index.html*.

Walter, U. (**1967**). Ph.D. thesis, California Institute of Technology.